STACKED SUBWAVELENGTH GRATINGS FOR IMAGING POLARIMETRY

by

PANFILO C. DEGUZMAN

A DISSERTATION

Submitted in partial fulfillment of the requirements
for the degree of Doctor of Philosophy in
Optical Science and Engineering
of
The School of Graduate Studies
of
The University of Alabama in Huntsville

HUNTSVILLE, ALABAMA

2000

DISSERTATION APPROVAL FORM

Submitted by Panfilo C. Deguzman in partial fulfillment of the requirements for the degree of Doctor of Philosophy in Optical Science and Engineering.

Accepted on behalf of the Faculty of the School of Graduate Studies by the dissertation committee:

Committee Chair

Program Chair

Department Chair

College Dean

Graduate Dean

ABSTRACT
School of Graduate Studies
The University of Alabama in Huntsville

Degree Doctor of Philosophy College/Dept Science/Optical Science and Engineering

Name of Candidate Panfilo C. Deguzman

Title Stacked Subwavelength Gratings for Imaging Polarimetry

The stacking of subwavelength gratings (SWG) in an integrated structure is presented for an application in imaging polarimetry. Imaging polarimetry extends the capability of conventional imaging by providing polarization information about a scene, in addition to variations in intensity. In this dissertation, a novel approach is introduced to develop a real-time imaging polarimeter. Subwavelength gratings are implemented as linear and circular polarization filters that are directly mounted onto the focal plane array of an infrared (IR) camera. Wire grid polarizers are used as linear polarization filters. The stacked structure, consisting of a wire grid polarizer and a form birefringent quarter-wave plate (QWP), implements the circular polarization filter and is the focus of this dissertation.

Initial investigations of the development of the individual SWG components and their integration are presented. Rigorous Coupled Wave Analysis (RCWA) was used to design the SWG structures. A broadband form birefringent quarter-wave plate for the 3.5 to 5 μm wavelength range was designed as a grating structure patterned directly into the substrate. Two fabrication methods for the wire grid polarizer were investigated. A 0.5 μm period polarizer was patterned by interference lithography. A 1 μm period polarizer was patterned by contact printing.

The stacking of the subwavelength grating structures was analyzed using the Jones Matrix calculus and a new RCWA method (developed by fellow graduate student Jianhua Jiang). Stacked SWG's were fabricated as large area (1.3 cm x 1.3 cm) filters and as a 256 x 256 array of small aperture (15 μm x 15 μm) pixels. Two stack designs were investigated, referred to as Stack I and Stack II. Stack I consisted of the 0.5 μm period polarizer and the form birefringent QWP. Stack II consisted of the 1 μm grid period polarizer and the form birefringent QWP. Simulation and measured results are presented to compare the cases of samples with and without AR-coating for the large area filters. The fabrication and optical testing of the small aperture SWG stacks which implement the circular polarization filters of the imaging polarimeter are presented.

Abstract Approval: Committee Chair ______________________

(Date)

Department Chair ______________________

Graduate Dean ______________________

ACKNOWLEDGEMENTS

The work described in this dissertation would not have been possible without the assistance of a number of people. I would like first to thank Dr. Gregory P. Nordin for his suggestion of the research topic, guidance throughout the entire process of the work and genuine concern for his students. Secondly, I would like to thank the other members of my committee who offered helpful suggestions and comments. I would like to thank Nichols Research Corporation for financially supporting this project. I would like to acknowledge the financial support from a National Science Foundation Traineeship award.

I would also like to thank my wife, Sachiko, and my family for giving me a lot of support and encouragement throughout this whole endeavor.

TABLE OF CONTENTS

Page

LIST OF FIGURES

Figures Page

LIST OF TABLES

Table Page

Chapter 1

INTRODUCTION

A diffraction grating that propagates only the 0^{th} diffraction order due to a sufficiently small period is called a subwavelength grating (SWG). Subwavelength grating structures have been demonstrated in many device configurations such as polarization components (e.g., waveplates [1,2] wire grid polarizers [3,4] and polarizing beam splitters [5,6]), anti-reflection surfaces [7,8,9], narrowband filters [10,11] and graded-index components [12] (e.g., binary lenses [13,14] and blazed gratings [15,16,17]). Such devices are useful for applications in imaging systems, laser systems, spectroscopy, polarimetry, and integrated optics.

An attractive option not previously explored is the stacking of subwavelength gratings into a single device to perform multiple functions. This is analogous to forming a sequence of discrete elements on a common substrate. The planar structure of SWG's is well-suited for stacking and several advantages are gained from this type of integration, including a reduction in overall device thickness, flexibility in the design of complex optical systems, improvement in alignment accuracy, possible low-cost fabrication, and the direct transfer of classical optical systems and designs into a compact structure. In addition, optical arrays can be naturally implemented in order to provide a large number of optical channels.

As an example of stacked SWG's, this dissertation will focus on an application in imaging polarimetry. An imaging polarimeter is used to capture polarization information from a scene by means of linear and circular polarization filters. A novel approach is introduced to develop a real-time imaging polarimeter. A micro-optic device consisting of an array of linear and circular polarization filters is designed to be mounted directly on the focal plane array of an infrared (IR) camera. Such an array of polarization components is naturally implemented by SWG structures. Wire grid polarizers are used as the linear polarization filters. Stacked SWG structures are used as the circular polarization filters.

This dissertation presents the design, fabrication and optical performance of stacked SWG's for a real-time imaging polarimeter application. The structures required to implement a circular polarization filter for the mid-wave infrared (MWIR) are a broadband form birefringent quarter-wave plate (QWP) and a wire grid polarizer. Initial investigations focused on developing the individual structures to characterize their performance and the stacking process required to integrate them. Our imaging polarimeter requires a 512 x 512 array of filter pixels that align to the focal plane array pixels of the camera. However, large area versions of these components were first fabricated to facilitate the optical testing of the component spectral characteristics. An overview of the dissertation is described below.

1.1 Overview of Dissertation

Chapter 2 provides background information on subwavelength gratings and also describes the quantities measured by the imaging polarimeter, namely the Stokes parameters, which are used to completely describe the polarization state of light. This is accomplished by first reviewing the various applications of SWG’s which is then followed by a literature review of reactive ion etching to achieve anisotropic etching of silicon. This is relevant for the fabrication of form birefringent QWP’s. Next, the derivation of the four Stokes parameters and the procedure used by the polarimeter to measure them is described.

Chapter 3 introduces our novel approach to develop a real-time imaging polarimeter by integrating the complete set of linear and circular polarization filters directly onto the focal plane array of the camera. A brief review of recent applications of polarization imaging is presented.

Chapter 4 presents approximate and rigorous methods used to analyze subwavelength grating structures. Effective medium theory (EMT) and rigorous coupled wave analysis (RCWA) are techniques used in this dissertation to model the individual subwavelength grating structures. The modeling of stacked SWG structures having arbitrary structural parameters and angular orientations were analyzed with the following approaches. A Jones matrix approach approximates the stack as two cascaded bulk components and therefore disregards multi-layer interactions. A novel RCWA technique to analyze SWG stacks, called the Stacked Rotated Grating RCWA, has been developed by Jiang and Nordin [18]. An overview of these techniques is presented.

Chapters 5 and 6 describe the development of the broadband form birefringent QWP and the wire grid polarizer, respectively, for the 3.5 to 5 micron wavelength range. In the literature, this is the first report on the physical implementation of broadband form birefringent wave plates that make use of form birefringence-based dispersion. Wire grid polarizers developed in this dissertation are also novel: 1) wire grid polarizers use molybdenum (Mo) as the metal grid, and 2) wire grid polarizers with 1 micron period are patterned by contact lithography. A description of the design, fabrication and performance of these components is discussed.

Chapter 7 presents the integration of a form birefringent quarter-wave plate and a wire grid polarizer to implement another functionality, a circular polarization filter. This is the first report in literature of a multi-functional device realized by stacked subwavelength gratings [19]. Two stack designs for large area (~1 cm^2) uniform filters are investigated to determine fabrication practicality and spectral performance by Fourier transform infrared (FTIR) testing.

Chapter 8 looks at the different aspects of transitioning from the large aperture circular polarization filter to an array of small aperture (15 μmx15 μm) circular polarization filters. The effect of the finite aperture on the QWP retardance and the wire grid polarizer extinction ratio is investigated. Fabrication of the 512 x 512 array of linear and circular polarization filters and performance results from infrared microscope testing are presented.

Chapter 9 summarizes the results and accomplishments of this doctoral research. Future research and improvements are discussed.

Chapter 2

BACKGROUND

This section of the dissertation provides background information on subwavelength grating structures and on the quantities measured by the polarimeter, the Stokes parameters. The SWG condition of propagating only the 0th diffration order, and the various implementations of SWG's reported in the literature, is presented in Section 2.1. A literature review of reactive ion etching (RIE) of silicon is provided in Section 2.2 to acquaint the reader with the fabrication challenge of achieving an anisotropic etch. As background for imaging polarimetry (Chapter 3), the Stokes parameters are derived and the polarimetric measurement of these quantities is described in Section 2.3.

2.1 Subwavelength Gratings

The grating equation, which describes the propagation of diffracted orders from a grating, is discussed and graphically illustrated in Section 2.1.1. A literature review on the form birefringent QWP and the wire grid polarizer is given in Section 2.1.2. Other implementations are described in following sections.

2.1.1 Graphical Illustration of the Grating Equation

The grating equation describes the direction of propagation of light due to diffraction by a grating. To obtain an insight into the diffraction process, we consider the case of an optical plane wave with wavevector $\mathbf{k}_i=\mathbf{k}_i(x,z)$ and incidence angle θ_i, diffracted by a 1-D grating with grating vector $\mathbf{K}=K_G\mathbf{x}=(2\pi/\Lambda)\mathbf{x}$ shown in Figure 2.1. The grating equation for this planar diffraction case is given by

$$n_q \sin\theta_{q,m} - n_I \sin\theta_i = m\lambda/\Lambda, \tag{2.1}$$

where the subscript q refers to region I (for reflected orders) or region II (for transmitted orders), n_q is either n_I or n_{II} , m is the diffraction order, and $\theta_{q,m}$ is the m^{th} order diffracted angle with respect to the z axis. Multiplication by $2\pi/\lambda$ expresses the equation in terms of the x and z components of the wavenumber k in regions I and II:

$$(k_{q,m})_x - (k_i)_x = m K_G \tag{2.2}$$

$$(k_{q,m})_z = (k_q^2 - (k_{q,m})_x^2)^{1/2}. \tag{2.3}$$

Propagating orders are those for which $(k_{q,m})_z$ is real. This can be interpreted graphically as shown in Figure 2.1. The reflected and transmitted orders lie on the semi-circles of radius k_I and k_{II}, respectively. In this example, non-zero order reflections and transmission can propagate along with the 0^{th} diffraction orders. If the grating vector K_G is made larger (or equivalently, the grating period smaller), fewer number of orders can propagate. The SWG condition occurs when K_G is chosen large enough such that only the 0^{th} diffraction orders can propagate and all other orders are evanescent. For normal incidence, this condition is met by choosing K_G to be larger than k_I and k_{II}, which is equivalent to choosing Λ to be less than λ/n_I and λ/n_{II}.

2.1.2 Polarization-Sensitive Components

The form birefringent property of SWG's is utilized for applications such as wire grid polarizers, wave plates, beam splitters, and polarizing mirrors. A review of the polarization components used in this dissertation is presented below.

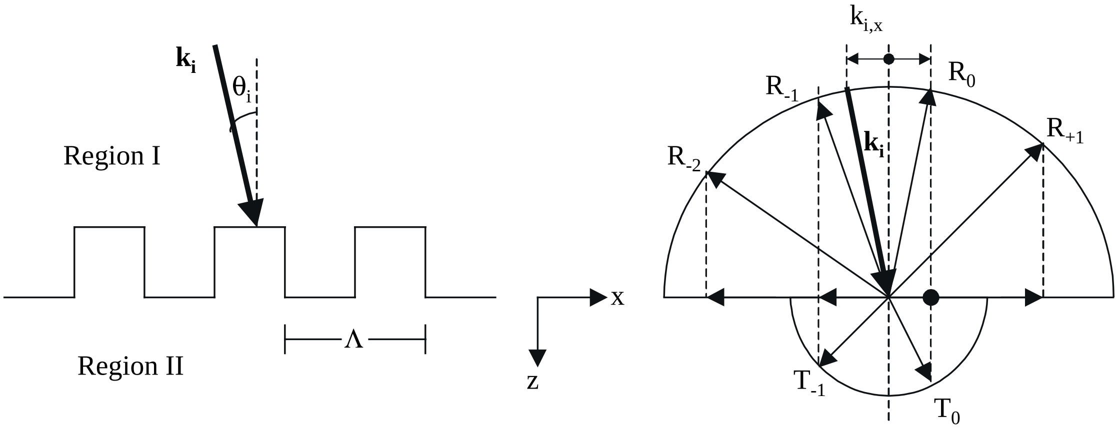

Figure 2.1 Diagram of the geometry of the diffraction grating and graphical representation of the grating equation.

2.1.2.1 Form Birefringent Quarter-Wave Plate

An isotropic material can be made to exhibit an artificial birefringence by structuring its surface with a SWG. The anisotropy of the grating region leads to the induced birefringence which is typically termed form birefringence [20]. A conventional wave plate tends to be bulky because it is made from naturally birefringent materials, such as quartz, calcite or mica, which have relatively small birefringence (e.g., calcite: $\Delta n = 0.172$ at $\lambda=589.3$ nm). Furthermore, birefringent materials suitable for a specific wavelength region may not exist. On the other hand, form birefringence can be designed for any wavelength region (given a suitable substrate), and can provide comparably larger birefringence which minimizes thickness (e.g., a silicon grating covered by medium having $n=1.5$ such as treated in this proposal gives: $\Delta n = 0.46$ at $\lambda= 4$ µm).

Approaches to modeling SWG's include the approximate method of EMT and rigorous methods, such as RCWA. The EMT analysis is accurate when the grating period, Λ, is much smaller than the wavelength, λ, of the incident radiation. Under this condition, the SWG is treated as an anisotropic, homogeneous film, and closed-form expressions are derived for the effective indices of the TE and TM modes. Birefringence calculations using EMT have been used by several groups to design wave plates [21,22]. A rigorous method is necessary when Λ is no longer much smaller than λ, and several groups have designed wave plates using RCWA [22,23,6]. A recent paper by Kikuta *et al.* [24] proposed a design of an achromatic QWP that deviates from the phase retardance of 90° by less than 3° for a ±10% bandwidth from the center wavelength. The broadband QWP designed in this dissertation is intended to operate over a much wider wavelength range of ±17.6% from the center wavelength (i.e., 3.5 to 5 µm), and a phase retardation error below 3° is achievable for the best-case design.

Fabrication of subwavelength QWP's has been attempted using volume holographic materials, but because of low birefringence (Δn = 8.7x10-3), an emulsion thickness of 18.5µm was required [23]. The fabrication process becomes more complex for surface-relief wave plates, but several advantages such as thickness reduction and material durability make it desirable. Several authors have fabricated *single wavelength* wave plates as surface-relief gratings on silicon nitride [1], amorphous silicon [25] and GaAs [6] for the visible and near infrared. To our knowledge, no surface-relief grating has been fabricated that performs as a *broadband* QWP.

2.1.2.2 Wire Grid Polarizer

Wire grid polarizers have been studied since the beginning of the century. More recently, Yeh [26] used EMT analysis to predict the performance of the wire grid polarizer. The development of RCWA has simplified the rigorous analysis of metal gratings. For example, Kuta *et al.* [27] modeled wire grid polarizers using RCWA in the visible and infrared for free-standing gold metal gratings in vacuum, and also gold metal gratings on silica and GaAs substrates. They characterized the diffraction efficiencies of the two orthogonal modes as a function of the wavelength, period, grating profile, and dielectric constant of the metal and substrate.

Wire grid polarizers have been fabricated using vacuum evaporation of metals. Ruled, dielectric gratings (or replicas) were used as the grid pattern for gold and aluminum that are deposited on the groove tips of the grating by vacuum evaporation at grazing angles [3,4]. Grating periods of the finished wire grids were limited by the capabilities of the ruling engine, and applications were mainly in the IR. Improvements in patterning photoresist by optical and non-optical exposure systems, and also improvements in dry etching technology have led to applications in the NIR and visible. Tungsten grid polarizers for the visible spectrum with 100 nm period and thickness have been fabricated through the use of electron-beam lithography to pattern photoresist, and RIE to transfer the pattern to tungsten [28]. The difficulty of fabricating such small features with high quality is seen with the measurement of the polarizer extinction ratio which amounted to a value of only 2 at normal incidence, much lower than the expected value of approximately 100.

2.1.3 Antireflection Surfaces

Typically, antireflection surfaces are achieved by depositing a stack of dielectric films. Alternatively, low reflectance surfaces can be realized using subwavelength gratings. For example, the corneas of certain moths are interestingly antireflective subwavelength surfaces [29]. A film is required to satisfy the conditions on refractive index $n=(n_{in}n_{out})^{1/2}$ and thickness $h=\lambda/4n$ to behave as an antireflective structure [30], in which n_{in} and n_{ou} are the refractive indices of the substrate and ambient media. This can be achieved by designing the grating structure with an effective index equal to that value. Non-binary grating profiles have been shown to exhibit low reflectance over a wide wavelength range [7].

2.1.4 Guided-Mode Resonance Filters

Narrowband filters have been realized using the resonance anomalies of diffraction gratings [10,11]. Such anomolies were first reported by Wood in 1902 when he illuminated a metallic grating and measured almost zero transmission for certain wavelengths [31]. Resonance conditions occur for a suitable choice of incidence angle, grating thickness, grating period and refractive indices.

The grating region is designed to have a ridge index of $n_g+\Delta n$ and trough index of $n_g-\Delta n$, and n_g is chosen to be larger than the indices of the surrounding media. At the resonance wavelength, there is constructive interference that result in perfect reflectance. This resonant condition is very sensitive to small changes in the incidence angle, wavelength, or other parameters. In general, the width of the resonance peak increases with increasing modulation Δn. These waveguide modes can exhibit very narrow filter linewidths of $\Delta\lambda/\lambda=10^{-7}$ [10].

2.1.5 Graded-Index Components

The internal structure of a subwavelength grating can be modulated such that the grating can function like a graded-index material. For example, modulating the fill factor has been used to produce structures that are equivalent to diffractive lenses [13,14] and blazed gratings [15-17]. Figure 2.2 shows a blazed grating and an equivalent SWG with a modulated fill factor. The appropriate fill factor at individual carrier-grating period Λ_c regions can be determined rigorously, or by the use of effective medium theory when the period-to-wavelength ratio is sufficiently small [32].

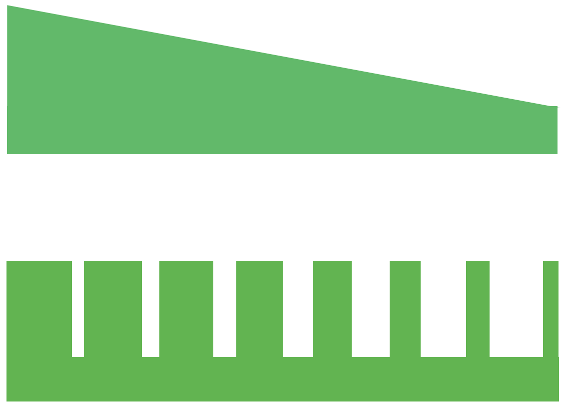

Figure 2.2 Blazed grating realized by modulating the fill factor of a SWG structure.

Fabrication of diffractive phase elements is very attractive because only one lithography step and etching step are needed to create the SWG pattern. A multi-layer binary gratings approach requires alignment between multiple lithography and etch steps. Another alternative is gray scale lithography which requires careful control of resist profile.

2.2 Anisotropic Reactive Ion Etching using Fluorine-Based Chemistry

Anisotropic etching of silicon (Si) is required for various applications such as integrated circuit fabrication, integrated optoelectronics, micromachining, integrated sensors, and novel devices. A commonly used dry etching method is the reactive ion etch (RIE) plasma process which combines ion bombardment with chemically reactive species. Many Si etch processes developed have used chlorine-containing gases, and often with modified RIE systems, such as those allowing cryogenic cooling, or with other plasma sources like electron cyclotron resonance (ECR) [33] and inductively coupled plasma (ICP) [34] systems which generate high-density plasma under lower pressure conditions. Chlorine etching is very slow without ion bombardment, so the etch is determined by the ion bombardment direction, normal to the surface.

Fluorine, on the other hand, etches without any help from the ion bombardment, so anisotropic profiles are harder to achieve. The advantage of using fluorine over chlorine is environmental safety since it is less toxic and corrosive than chlorine.

Etching deep trenches into Si with high aspect ratios is a challenge for a basic RIE system using F-based etch chemistries. A high aspect ratio of 6.7 combined with very narrow grooves 0.3 µm wide, which we needed to fabricate, makes for an even bigger challenge. Several groups have reported using F-based etch chemistries which provide good anisotropy. A technique to improve etch anisotropy is to allow formation of a passivating film on the grating sidewalls to inhibit lateral etching. In one case, the etching of deep holes (~1 µm wide, 5 µm deep) using $CBrF_3$ gas was assisted by film formation on the sidewalls which was determined to be aluminum (due to the Al RIE cathode) and oxygen (due to the SiO_2 etch mask) [35]. Film formation on the side walls by adding a gas with the necessary precursor components to the mixture is a very popular method. Trenches (~10 µm wide, 20 µm deep) using a $CBrF_3/SF_6/Ar$ mixture relied on the $CBrF_3$ gas to form polymers to protect the sidewalls [36]. A black silicon method uses an $SF_6/O_2/CHF_3$ mixture for etching deep trenches (up to 200 µm) with high aspect ratios (up to 10), in which the O_2 gas in the mixture reacted with Si to form an oxide film that inhibited lateral etching [37]. The minimum feature achievable with this process was not specified, but etched trenches shown were approximately 4 µm. An etch chemistry of SF_6 and CHF_3 gases was used to fabricate silicon nanowires, in which the F radicals chemically etch Si, while CF_2 is used to form a polymer film on the sidewall [38]. The feature sizes of the Si pillars were very small (50nm wide), and these structures had low fill factor. Although none of these etches show the results we are searching for, i.e., high fill factor (68%) and narrow etch grooves (0.3 µm), they provide a good starting point for our fabrication process.

A successful process for producing Micro Electro Mechanical Systems (MEMS) devices uses an ICP plasma source which generates a high density plasma at low pressure [39]. A sequence of alternating etch and deposition steps is balanced to control the anisotropy. The etch chemistry of SF_6 and fluorocarbons for sidewall passivation, such as CHF_3 and C_2F_6, have been used to fabricate 2 µm wide trenches that are extremely deep (~30 µm). Feature sizes as low as 1µm, etch depths of 2 µm to 100 µm, and aspect ratios of 30 are claimed to be achievable with this process. Anisotropic etching using film formation for side-wall passivation is now an established processing technology [40].

2.3 Stokes Parameters

Stokes parameters give a complete description of any polarization state of light. They are quantities that are acquired by measurement of the intensity of the optical field after passing through a set of polarization filters. A derivation of these quantities and the significance of each parameter are discussed in Section 2.3.1 The classical method of measuring these quantities is outlined in Section 2.3.1. This treatment follows the exposition given by Collett [41].

2.3.1 Derivation of Stokes Parameters

Consider two plane waves that are orthogonal to each other:

$$E_x(t) = E_{0x}(t)\cos[\omega t + \delta_x(t)] \tag{2.4}$$

$$E_y(t) = E_{0y}(t)\cos[\omega t + \delta_y(t)]\,. \tag{2.5}$$

The polarization ellipse is given by

$$\frac{E_x^2(t)}{E_{0x}^2(t)} + \frac{E_y^2(t)}{E_{0y}^2(t)} - \frac{2E_x(t)E_y(t)}{E_{0x}(t)E_{0y}(t)}\cos\delta(t) = \sin^2\delta(t)\,, \tag{2.6}$$

where $\delta(t) = \delta_y(t) - \delta_x(t)$. For monochromatic radiation, the amplitudes and phases are constant in time such that

$$\frac{E_x^2(t)}{E_{0x}^2} + \frac{E_y^2(t)}{E_{0y}^2} - \frac{2E_x(t)E_y(t)}{E_{0x}E_{0y}}\cos\delta = \sin^2\delta\,, \qquad (2.7)$$

The observed quantity is the time average of the fields:

$$\frac{< E_x^2(t) >}{E_{0x}^2} + \frac{< E_y^2(t) >}{E_{0y}^2} - \frac{2 < E_x(t)E_y(t) >}{E_{0x}E_{0y}}\cos\delta = \sin^2\delta\,, \qquad (2.8)$$

where

$$< E_i(t)E_j(t) >= \lim_{T\to\infty}\frac{1}{T}\int_0^T E_i(t)E_j(t)dt \qquad \text{i,j=x,y.} \qquad (2.9)$$

Then,

$$< E_x^2(t) >= \frac{1}{2}E_{ox}^2 \qquad (2.10)$$

$$< E_y^2(t) >= \frac{1}{2}E_{oy}^2 \qquad (2.11)$$

$$< E_x(t)E_y(t) >= \frac{1}{2}E_{0x}E_{oy}\cos\delta\,. \qquad (2.12)$$

Substitution leads to

$$2E_{ox}^2E_{oy}^2 + 2E_{ox}^2E_{oy}^2 - (2E_{ox}E_{oy}\cos\delta)^2 = (2E_{0x}E_{oy}\sin\delta)^2\,. \qquad (2.13)$$

First two terms can expressed as perfect squares so that

$$(E_{ox}^2 + E_{oy}^2)^2 - (E_{ox}^2 - E_{oy}^2)^2 - (2E_{ox}E_{oy}\cos\delta)^2 = (2E_{0x}E_{oy}\sin\delta)^2\,. \qquad (2.14)$$

The quantities in parenthesis are the Stokes parameters:

$$S_0 = E_{ox}^2 + E_{oy}^2 \qquad (2.15)$$

$$S_1 = E_{ox}^2 - E_{oy}^2 \qquad (2.16)$$

$$S_2 = 2E_{ox}E_{oy}\cos\delta \tag{2.17}$$

$$S_3 = 2E_{ox}E_{oy}\sin\delta\,. \tag{2.18}$$

For completely polarized light,

$$S_0^2 = S_1^2 + S_2^2 + S_3^2\,. \tag{2.19}$$

The Stokes parameters are observables. S_0 describes the total intensity of light. S_1 describes the amount of linear polarization that is horizontal or vertical. S_2 describes the amount of linear polarization that is 45° or -45°. S_3 describes the amount of circular polarization that is right or left rotation.

In terms of complex amplitudes, the Stokes parameters can be written as

$$S_0 = E_xE_x^* + E_yE_y^* \tag{2.20}$$

$$S_1 = E_xE_x^* - E_yE_y^* \tag{2.21}$$

$$S_2 = E_xE_y^* + E_yE_x^* \tag{2.22}$$

$$S_3 = i(E_xE_y^* - E_yE_x^*)\,. \tag{2.23}$$

2.3.2 Measurement of Stokes Parameters

Measurement of the Stokes parameters is performed with the use of a retarder and a polarizer. The retarder (with retardance ϕ) advances the phase of the x-component by $\phi/2$ and retards the y-component by $\phi/2$:

$$E_x^1 = E_xe^{i\phi/2} \tag{2.24}$$

$$E_y^1 = E_ye^{-i\phi/2}\,. \tag{2.25}$$

With the transmission axis of the polarizer at angle θ (from x-axis), the transmitted field will be

$$E = E_x^1 \cos\theta + E_y^1 \sin\theta$$

$$= E_x e^{i\phi/2} \cos\theta + E_y e^{-i\phi/2} \sin\theta \,. \tag{2.26}$$

The intensity given by $I = E^* E$ is

$$\begin{aligned} I(\theta,\phi) &= \frac{1}{2}[(E_x E_x^* + E_y E_y^*) + (E_x E_x^* - E_y E_y^*)\cos 2\theta + \\ &(E_x E_y^* + E_y E_x^*)\cos\phi \sin 2\theta + i(E_x E_y^* - E_y E_x^*)\sin\theta \sin 2\phi] \\ &= \frac{1}{2}[S_0 + S_1 \cos 2\theta + S_2 \cos\phi \sin 2\phi + S_3 \sin\theta \sin 2\theta]. \end{aligned} \tag{2.27}$$

With no retarder (ϕ = 0°), the quantities S_0, S_1, and S_2 can be determined by placing the polarizer axis at θ = 0°, 45°, and 90°. S_3 is determined with the retarder having ϕ = 90° and polarizer at θ = 45°. The Stokes intensity formula $I(\theta,\phi)$ gives

$$I(0^\circ,0^\circ) = \frac{1}{2}[S_0 + S_1] \tag{2.28}$$

$$I(45^\circ,0^\circ) = \frac{1}{2}[S_0 + S_2] \tag{2.29}$$

$$I(90^\circ,0^\circ) = \frac{1}{2}[S_0 - S_1] \tag{2.30}$$

$$I(45^\circ,90^\circ) = \frac{1}{2}[S_0 + S_3] \,. \tag{2.31}$$

Solving for the Stokes parameters:

$$S_0 = I(0^\circ,0^\circ) + I(90^\circ,0^\circ) \tag{2.32}$$

$$S_1 = I(0^\circ,0^\circ) - I(90^\circ,0^\circ) \tag{2.33}$$

$$S_2 = 2I(45^\circ,0^\circ) - I(0^\circ,0^\circ) - I(90^\circ,0^\circ) \tag{2.34}$$

$$S_3 = 2I(45^\circ,90^\circ) - I(0^\circ,0^\circ) - I(90^\circ,0^\circ) \,. \tag{2.35}$$

The basic polarimeter measures the intensity passing through the four polarization filters (i.e., *I*(0,0), *I*(90,0), *I*(45,0), and *I*(45,90)) sequentially in time. Each filter is alternately placed in front of the camera and the intensity is measured. Real-time specification of the Stokes parameters is therefore not possible. In the following chapter, we present a novel imaging polarimeter design that realizes real-time operation.

Chapter 3

REAL-TIME IMAGING POLARIMETRY

Imaging polarimetry can extend the capability of conventional imaging by providing polarization information about a scene, in addition to variations in intensity. An imaging polarimeter can therefore function in either of two modes to produce a high contrast image by means of measuring spatial variations in polarization or intensity. As a consequence, even if very little intensity contrast is present in the scene, it is still possible to achieve high contrast images from polarization contrast. Significant improvements in image contrast have therefore drawn increasing attention to the use of polarization imagery in a number of applications.

Polarization imaging cameras have been developed for the visible, mid-wave IR and long-wave IR wavelength regions [42,43,44,45,46]. A complete Stokes vector can be attained from intensity measurements through four different polarization filters. A basic imaging polarimeter acquires these measurements sequentially in time, i.e., the first filter is placed in front of the camera and a frame is grabbed, and then the next filter is placed in front of the camera and another frame is grabbed, and so on. Since these measurements are not simultaneous, it cannot function in real time and is therefore not useful when the camera is in motion or if the scene is changing in time. Approaches for realizing real-time capability include the use of liquid crystal that is modulated at high frequencies to allow sequential sampling of the four Stokes parameters in essentially simultaneous manner [47,48]. The drawback of using liquid crystal polarization optics for precise polarimetry is the lack of an inherent calibration arising from their high temperature sensitivity and retardation variation with wavelength. Another approach has been proposed in which a photopolarimeter uses a beam splitter to divide the incident beam into four copies of the original image so as to allow simultaneous measurement of the four Stokes parameters [49]. This approach however requires the use of multiple detector arrays.

In this dissertation, a novel approach is introduced to develop a real-time imaging polarimeter. The design requires a micro-optic device, consisting of a complete set of linear and circular polarization filters, to be mounted directly onto the focal plane array of the camera. Simultaneous intensity measurements of all the polarization information can therefore be acquired within each image frame allowing for the real time measurement of the complete Stokes vector [50]. In this chapter, a brief review of recent applications of polarization imaging is presented. A description of our real time approach for imaging polarimetry will follow.

3.1 Imaging Polarimeter Applications

Some recent applications of polarization imaging can be found in astronomy, medicine, and remote sensing. Polarization properties of planets, stars and nebulae have been studied [51]. Solar magnetic fields can be determined by measuring the solar polarization arising from the Zeeman effect in sunspots using imaging polarimeters that are combined with narrowband tunable spectral filters [48,47]. A recent clinical study demonstrated that a polarization camera is able to visualize the true margins of skin cancer not clinically visible to dermatologists [52].

Remote sensing applications are numerous because of the information that can be gathered from spectrometric techniques [53]. Target discrimination and classification has been significantly enhanced by polarization characterization. It has been applied to target recognition in military systems, environment, and machine vision for transportation systems [42]. The polarization property of an object is dependent on material composition and surface geometry. Metal and dielectric surfaces can be distinguished from each other by the characteristic elliptical polarization each produces from reflection. Surfaces can be differentiated from the type of reflection, specular or diffuse. The edges of a surface can also be enhanced which is useful to identify an object from its background. Examples of polarimetric discrimination include the detection of military vehicles from their background. The vehicle's antiballistic glass transmits a characteristic polarization that is different from the background. Camouflage netting is colored and textured to resemble the background but can be discriminated from the background terrain because of its highly polarized reflection. Satellite monitoring systems use polarization to determine the distribution of atmospheric particle and aerosol size and cloud particle size. Soil and rocks have the tendency to polarize light while grass does not. Foliage can be discriminated by the circular polarization it produces due to the birefringence present in floral structures. Other applications of polarimetric camera systems, such as the detection of ice on aircraft, ice on roadways, surface and buried land mines, have also been cited [54].

3.2 Real-Time Imaging Polarimeter Implementation

Our approach to realize real-time operation is to integrate a complete set of linear and circular polarization filters directly onto the focal plane array of the camera. Simultaneous intensity measurements from all the polarization filters can then be acquired in each image frame for the real time specification of the complete Stokes vector. The first three Stokes parameters, which measure the linear polarization content, can be acquired with linear polarizers at angular orientations of 0°, 45° and 90°. We have already reported this linear-only micro-optic device [55]. The fourth Stokes parameter, which measures circular polarization content, can be acquired with a circular polarization filter consisting of a quarter-wave plate and a polarizer. These four polarization filters together make up the unit cell of the complete micro-optic polarization filter array of the camera.

3.2.1 Layout of the Real-Time Imaging Polarimeter

A layout of the real-time imaging polarimeter is shown in Figure 3.1. A typical mid-infrared focal plane array consists of an indium antimonide (InSb) detector array that is conductively bonded by indium bumps to a silicon electronics backplane and packaged on a sapphire substrate. Polarization filters are located on the side of the micro-optic device adjacent to the InSb focal plane array detector. The filters are positioned as close to the FPA as possible so as to minimize cross-talk between adjacent pixels. Each polarization filter on the micro-optic is spatially registered to an underlying FPA pixel. The FPA is a 512 x 512 pixel array having a 25 μm pitch and 100% fill factor.

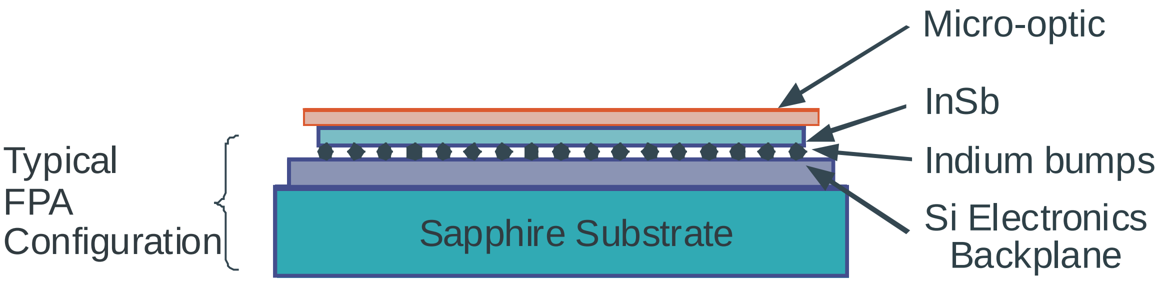

Figure 3.1 Layout of the integration of the DOE with the FPA detector.

The polarization filter unit cell, shown in Figure 3.2, consists of a 2 x 2 array of polarization filters that correspond to three linear polarization filters and a circular polarization filter. The circular polarization filter consists of a polarizer stacked above a QWP and rotated 45° with respect to the QWP axis. The design shown will pass light that is right circularly polarized (RCP) and block light that is left circularly polarized (LCP). The filters are noticeably smaller in dimension, 15μm x 15μm, than the FPA pixels in order to minimize cross-talk between adjacent pixels. The smaller dimension is also necessary for practical reasons to accomodate alignment errors associated with the fabrication of the filter elements and the mounting of the micro-optic to the FPA. The division of the 512 x 512 array by 4 different filter elements leads to 256 x 256 image pixels for each polarization filter. The design of incorporating all the filters in a single micro-optic device therefore permits real-time operation but leads to a reduction in image resolution.

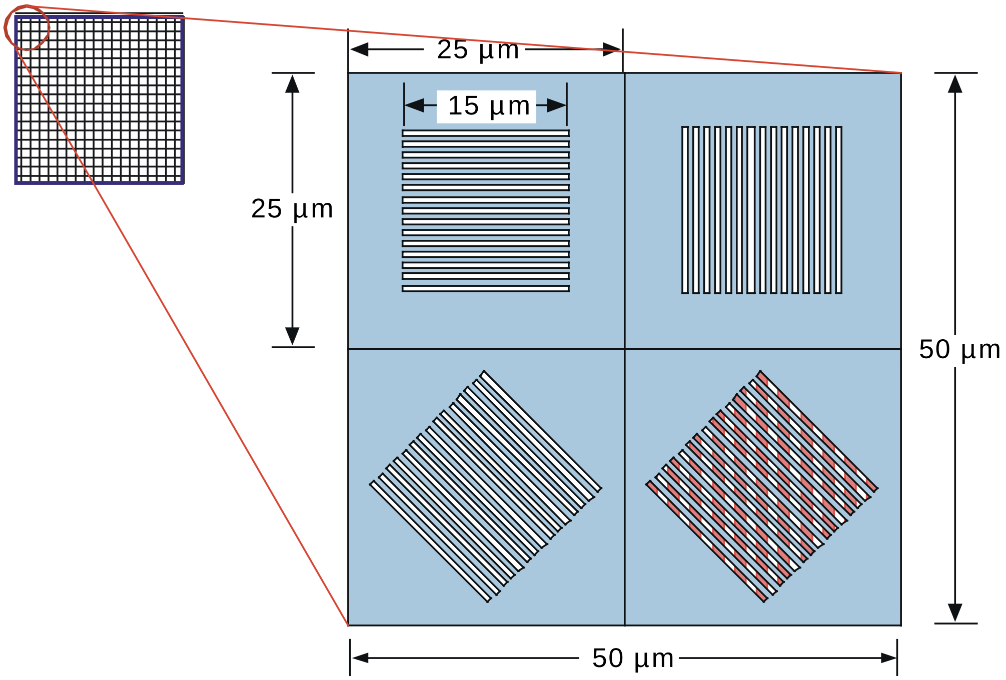

Figure 3.2 Unit cell of polarization filters.

A cross-sectional diagram of the device layers showing the linear polarizer and the circular polarizer consisting of the SWG stack is shown in Figure 3.3. The form birefringent QWP is fabricated directly on the silicon substrate surface. An SU-8 layer is used to planarize this underlying surface-relief for the stacking of a second SWG layer. A thin SiO_2 layer is deposited above the SU-8 layer. The Mo wire grid polarizer is then patterned above this SiO_2 layer and then protected with another SiO_2 capping layer.

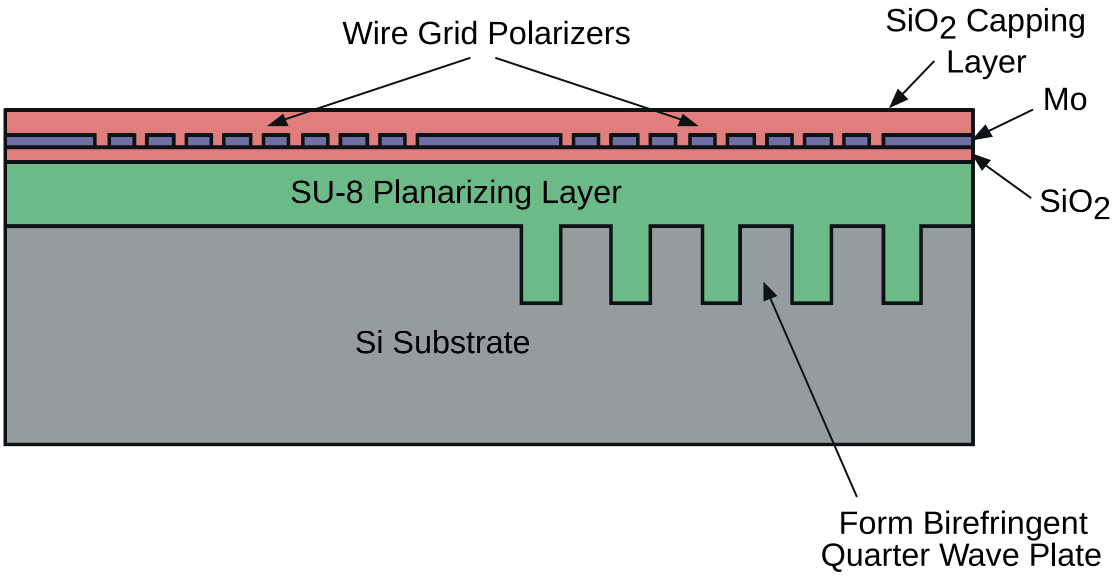

Figure 3.3 Device layers of an adjacent linear polarizer and circular polarization filter.

3.3 Conclusion

In this chapter, we presented various applications of imaging polarimetry and a new approach of designing a real-time imaging polarimeter by the use of a micro-optic device that incorporates all four polarization filters. The design requires the use of subwavelength gratings to implement the polarization components that measure the Stokes vector components. Polarizers oriented at 0°, 45°, and 90° will measure the linear polarization content and a polarizer/QWP stack will measure the circular polarization content. The design requires careful attention to alignment errors to avoid possible optical cross-talk between adjacent pixels. The 512 x 512 pixel array of the FPA is divided among four polarization filters resulting in four sets of 256 x 256 image pixels. With the capability to make measurements simultaneously with the four polarization filters, the polarization state of the incident beam can be specified in real time.

Chapter 4

ANALYSIS METHODS OF SUBWAVELENGTH GRATING STRUCTURES

In this work, rigorous and approximate theoretical methods have been used to analyze subwavelength grating structures. Effective medium theory (EMT) is an approximate theory that is valid when the period of the SWG is sufficiently small in comparison to the incident wavelength [32]. It is useful for producing starting points for the more intensive rigorous calculations, and also for deriving insightful analytical formulas for calculating the optical properties of the grating. Rigorous Coupled Wave Analysis (RCWA) is one of the most commonly used techniques to accurately analyze the diffraction of electromagnetic waves by periodic structures. It has been successfully applied to the analysis of holographic gratings and surface-relief grating structures [56]. The SWG structures designed and fabricated in this dissertation were analyzed using the rigorous method of RCWA. Effective medium theory simulations were also performed for the form birefringent QWP. This approximate analysis, however, was found to be inaccurate for the treatment of metal gratings [57].

The analysis of stacked SWG components was performed using both approximate and rigorous calculations. In the Jones Matrix calculus [58], the stack is treated as two cascaded bulk components. The analysis excludes the effects due to multi-layer interactions and the results are therefore only approximate. The rigorous method used to study the SWG stack is the Stack Rotated Grating RCWA (SRG-RCWA) technique developed by Jiang and Nordin [18]. It is used for the analysis of multi-layer binary gratings that are stacked and arbitrarily rotated.

In Section 4.1, we outline EMT method and obtain equations for the effective indices of a SWG structures. In Section 4.2, we present an overview of the RCWA method. In Section 4.3, we present several areas in which the Jones matrix analysis was applied. Extinction ratio calculations are described in Section 4.3.2. Generation of elliptical polarization by non-ideal QWP and polarizer components is treated in Section 4.3.3. Analysis of the stacked SWG's is treated in Section 4.3.4. Finally, an overview of SRG-RCWA is given in Section 4.4.

4.1 Effective Medium Theory

An isotropic material can be made to exhibit an artificial birefringence by structuring its surface with a SWG. The anisotropy of the grating region leads to the induced birefringence which is typically termed form birefringence [20]. The analysis of form birefringence by effective medium theories is useful in the limit when the grating period is sufficiently small compared to the incident wavelength. Radiation encountering the spatially varying structure, with dimensions substantially smaller than its wavelength, will not be able to resolve the spatial variations and instead experience a spatial average of this structure. The grating structure can therefore be treated as an anisotropic thin film, a special case of a diffraction grating which diffracts light only into the 0th order. The EMT method used by Rytov to calculate the effective medium's optical properties will be described below and the reader is directed to Rytov [32] for a more detailed description.

4.1.1 TE Polarization

We derive the effective index of a stratified medium shown in Figure 4.1 for the TE case. The two mediums, with thickness values of h_1 and h_2, have different permitivities ε, and permeabilities μ. The period is given by $\Lambda = h_1+h_2$, and the fill factor *f* is defined as h_1/Λ.

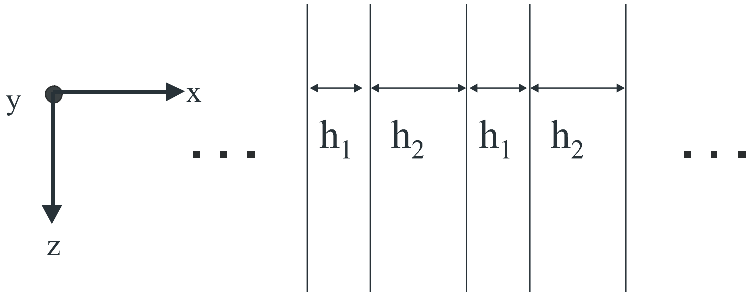

Figure 4.1 Stratified medium consisting of two different materials.

For a wave propagating in the z direction with the electric field in the y-direction, the electric and magnetic fields in the periodic (x-direction) structure may be written in the form

$$E_y = U(x)e^{iknz} \tag{4.1}$$

$$H_z = V(x)e^{iknz} \tag{4.2}$$

$$H_x = W(x)e^{iknz}. \tag{4.3}$$

Solutions consistent with Maxwell's equations are given as

$$U_j(x) = A_j \cos\alpha_j x + B_j \sin\alpha_j x \tag{4.4}$$

$$V_j(x) = \frac{i\alpha_j}{\mu_j\omega}[A_j \sin\alpha_j x - B_j \cos\alpha_j x] \tag{4.5}$$

$$W_j(x) = -\frac{nk}{\mu_j \omega}[A_j \cos\alpha_j x + B_j \sin\alpha_j x], \tag{4.6}$$

where

$$\alpha_j = k\sqrt{n_j^2 - n^2} \quad , \quad n_j^2 = \varepsilon_j \varepsilon_0 \text{ , and} \quad \text{j=region 1 or region 2.} \tag{4.7}$$

The field coefficients, A$_j$ and B$_j$, are determined by applying Maxwell's boundary conditions

$$U_1(h_1) = U_2(0), \qquad V_1(h_1) = V_2(0),$$

$$U_2(h_2) = U_1(0), \qquad \mathrm{V}_1(h_2) = V_1(0). \tag{4.8}$$

Substitution of the fields into the boundary conditions leads to the equation of the effective index of refraction, $n_{E\perp K}$, for a TE polarized wave:

$$\frac{\sqrt{n_1^2 - n_{E\perp K}^2}}{\mu_1}\tan[\pi\frac{h_1}{\lambda}\sqrt{n_1^2 - n_{E\perp K}^2}] = \frac{\sqrt{n_2^2 - n_{E\perp K}^2}}{\mu_2}\tan[\pi\frac{h_2}{\lambda}\sqrt{n_2^2 - n_{E\perp K}^2}]. \tag{4.9}$$

4.1.2 TM Polarization

The calculations for a TM-polarized incident wave proceeds in the same manner. From the symmetry in Maxwell equations however, results can be obtained directly from the formulas of the preceding sections if the parameters *H*, *E*, ε, μ are changed to *E*, -*H*, μ, ε. The effective index of refraction, $n_{E\|K}$, for the TM polarization can be shown to satisfy

$$\frac{\sqrt{n_1^2 - n_{E\|K}^2}}{\mu_1}\tan[\pi\frac{h_1}{\lambda}\sqrt{n_1^2 - n_{E\|K}^2}] = \frac{\sqrt{n_2^2 - n_{E\|K}^2}}{\varepsilon_2}\tan[\pi\frac{h_2}{\lambda}\sqrt{n_2^2 - n_{E\|K}^2}]. \tag{4.10}$$

The SWG structure can therefore be represented as a homogeneous uniaxial film layer with effective refractive indices given by the TE and TM cases.

4.1.3 Expansion of Effective Index of Refraction

Analytic forms for the effective index of refraction can be acquired from the expansion of the previous equations in terms of a power series:

$$\tan\delta = \delta + \frac{\delta^3}{3} + \frac{2\delta^5}{15} + \ldots \quad . \tag{4.11}$$

Use of only the first term leads to the zeroth order expansion. Addition of higher terms, such as the δ^3 and the δ^5 terms, leads to the 2nd order and the 4th order expansions, respectively. Simple closed form equations can be obtained from the calculation of the 0th order:

$$\begin{aligned} &\text{TE:} \quad n_{TE} = [\, f n_1^2 + (1-f) n_2^2]^{1/2} \\ &\text{TM:} \quad n_{TM} = [\, f n_1^{-2} + (1-f) n_2^{-2}]^{-1/2}, \end{aligned} \tag{4.12}$$

in which *f* is the fill factor. In this approximation, the grating period is assumed to be extremely small relative to the wavelength such that the effective index of refraction is only a function of the fill factor of the grating. Analytic expressions up to the 4th order expansion have been accomplished [7] to include the dependence on grating period. An exact solution of the effective index of refraction can be obtained by solving the trancendental equations given in Equations (4.9) and (4.10). In the design of the form birefringent QWP (Section 5.1), the EMT simulation results are obtained from calculating exact solutions to the transcendental equations.

4.1.4 Propagation in Stratified Films

Effective medium theory allows a uniaxial film equivalent to represent the subwavelength grating. For an arbitrary grating profile, multiple layers of binary gratings can suitably approximate this continuous profile. Using EMT, the effective indices of individual layers can be calculated and an equivalent stack of uniaxial film layers will represent the SWG. There are several methods available to determine the optical characteristics of stratified film layers [59,60,61]. The Berreman method [61] to treat stratified anisotropic media was chosen for this dissertation. The design and analysis of the form birefringent QWP was performed using EMT to approximate the grating profile into multiple anisotropic film layers and the 4x4 Method given by Berreman was used to calculate the reflection, transmission and phase retardance of the subwavelength grating. (The 4 x 4 Method of Berreman written in Matlab code is supplied in the Appendix.)

4.2 Rigoruous Coupled Wave Analysis

Rigorous coupled wave analysis, proposed by Gaylord and Moharam [56,62], is a vector analysis method used in the study of electromagnetic diffraction by grating structures. The approach of RCWA is to find solutions that satisfy Maxwell’s equations in each of the three (incident, grating and exit) regions and then match the tangential electric and magnetic fields components at the boundaries to calculate the propagating diffracted fields. Gratings are treated as binary, surface relief structures. The analysis of arbitrary periodic grating profiles dividing the profile into several binary grating layers. The RCWA code used in this dissertation was written by Chambers [63] using the Matlab software. The RCWA approach is described below.

4.2.1 Overview of RCWA Method

The periodic relative permitivities of the grating layers are expanded in a Fourier series. The fields in this grating region are expanded into space harmonic fields using the Floquet condition. Substitution of these fields into Maxwell’s equations leads to a set of 2nd order coupled-wave equations which can be written in matrix form as an eigenvalue problem. The eigenvalues and eigenvectors associated with the matrix are solved and the space harmonics of the tangential electric and magnetic fields are expressed in terms of these quantities. Maxwell's boundary conditions for these tangential fields are then applied at each interface in order to calculate the amplitudes of the reflected and transmitted fields. The diffraction efficiencies of the propagating orders are then calculated from the field amplitudes. A detailed description of the RCWA method is found in Moharam [56] and [62].

4.3 Jones Matrix Calculus

The Jones Matrix calculus was used to study light propagation through cascaded components. It was used in extinction ratio calculations for wire grid polarizer samples in Chapter 6. This method was also used to specify the polarization state of the incident radiation generated by a QWP and polarizer. To analyze stacked SWG structures, the stack is treated as two cascaded bulk components. This analysis excludes the effects due to multi-layer interactions. These Jones Matrix analyses are described in the following sections.

4.3.1 Jones Matrices for the Polarizer and QWP

The Jones matrix for a linear polarizer is

$$J_P = \begin{bmatrix} \alpha & 0 \\ 0 & \beta \end{bmatrix}, \tag{4.13}$$

in which α and β are the field amplitudes along the x and y axes. For an ideal polarizer, $\alpha = 1$ and $\beta = 0$.

The Jones matrix of a QWP with the fast axis in the x direction is

$$J_{WP} = \begin{bmatrix} \varsigma e^{i\varphi_x} & 0 \\ 0 & \eta e^{i\varphi_y} \end{bmatrix}, \tag{4.14}$$

in which ς and η are the field amplitudes, and φ_x and φ_y are the relative phases along the x and y axes. An ideal QWP has a phase difference φ (= φ_y - φ_x) of 90° and unity field amplitudes. The Jones matrix of a rotated component is calculated using the rotation matrix,

$$R(\theta) = \begin{bmatrix} \cos\theta & \sin\theta \\ -\sin\theta & \cos\theta \end{bmatrix}. \tag{4.15}$$

For a rotation of θ, the Jones matrix of the rotated component becomes

$$S' = R(-\theta) \cdot S \cdot R(+\theta). \tag{4.16}$$

4.3.2 Extinction Ratio Derivation

In this section, we derive the extinction ratio of the wire grid polarizer sample from the measurement acquired from testing with another polarizer having known properties. Radiation from the FTIR source is incident on the known polarizer first and then followed by the sample.

The Jones matrix for the cascaded polarizer components in parallel orientation is

$$M_P = \begin{bmatrix} \alpha_2 & 0 \\ 0 & \beta_2 \end{bmatrix} \begin{bmatrix} \alpha_1 & 0 \\ 0 & \beta_1 \end{bmatrix} = \begin{bmatrix} \alpha_1\alpha_2 & 0 \\ 0 & \beta_1\beta_2 \end{bmatrix}. \tag{4.17}$$

The electric field exiting the components is given by

$$E_p = M \begin{bmatrix} x \\ y \end{bmatrix} = \begin{bmatrix} x\alpha_1\alpha_2 \\ y\beta_1\beta_2 \end{bmatrix}, \tag{4.18}$$

in which x and y represent the electric field of the incident source along the x-axis and y-axis. The intensity exiting the components is given by

$$I_P = E_p^* E_p \tag{4.19}$$

$$I_p = [x^2\alpha_1^2\alpha_2^2 + y^2\beta_1^2\beta_2^2] = y^2\beta_1^2\beta_2^2[\frac{x^2}{y^2} ER_1 ER_2 + 1]. \tag{4.20}$$

The Jones matrix for the cascaded components in perpendicular orientation is

$$M_\perp = \begin{bmatrix} \beta_2 & 0 \\ 0 & \alpha_2 \end{bmatrix} \begin{bmatrix} \alpha_1 & 0 \\ 0 & \beta_1 \end{bmatrix} = \begin{bmatrix} \alpha_1\beta_2 & 0 \\ 0 & \alpha_2\beta_1 \end{bmatrix}. \tag{4.21}$$

The electric field and intensity exiting the components are given by

$$E_{\perp,y} = M \begin{bmatrix} x \\ y \end{bmatrix} = \begin{bmatrix} x\alpha_1\beta_2 \\ y\alpha_2\beta_1 \end{bmatrix} \tag{4.22}$$

$$I_\perp = E_\perp^* E_\perp \tag{4.23}$$

$$I_\perp = [x^2\alpha_1^2\beta_2^2 + y^2\alpha_2^2\beta_1^2] = y^2\beta_1^2\beta_2^2[\frac{x^2}{y^2} ER_1 + ER_2]. \tag{4.24}$$

The measured extinction ratio, *ER*, between the two polarizers is

$$ER = \frac{I_P}{I_\perp} = \frac{C \cdot ER_1 ER_2 + 1}{C \cdot ER_1 + ER_2} \text{ , where } C = x^2/y^2. \tag{4.25}$$

Solving for the extinction ratio of the wire grid polarizer sample, ER_2, this becomes

$$ER_2 = \frac{C \cdot ER\ ER_1 - 1}{C \cdot ER_1 - ER}. \tag{4.26}$$

4.3.3 The Polarization Ellipse

Testing of the circular polarization filters required illumination with nominal RCP and LCP radiation. Due to non-ideal input generating components, the actual polarization state is elliptical. Using Jones Matrix analysis, we can determine the principal semi-axes a and b of the ellipse and the angle ψ which the major axis makes with the x-axis.

The Jones matrix for a polarizer and a rotated QWP generating the RCP state is given by

$$\mathbf{M}_{\mathbf{RCP}} = R(-45^\circ)\cdot[QWP]\cdot R(+45^\circ)\cdot[Polarizer]\,. \tag{4.27}$$

The x-component along the transmission axis of the polarizer dominates the intensity because of the high ER value of the polarizer. We can determine the parameters of the polarization ellipse. The Jones vector of the electric field due to this x-component is

$$\mathrm{J}_{\mathrm{RCP}} = \mathbf{M}_{\mathbf{RCP}}\cdot\begin{bmatrix}1\\0\end{bmatrix} = \begin{bmatrix}a_1\exp(i\delta_x)\\a_2\exp(i\delta_y)\end{bmatrix}\,. \tag{4.28}$$

From the field amplitudes a_1 and a_2, and phase difference

$$\delta = \delta_y - \delta_x\,, \tag{4.29}$$

we can calculate ψ, a_1 and a_2 using the following equations [64]:

$$\tan 2\psi = \frac{2a_1a_2}{a_1^2 - a_2^2}\cos\delta \tag{4.30}$$

$$a^2 = a_1^2\cos^2\psi + a_2^2\sin^2\psi + 2a_1a_2\cos\psi\sin\psi\cos\delta \tag{4.31}$$

$$b^2 = a_1^2\sin^2\psi + a_2^2\cos^2\psi - 2a_1a_2\cos\psi\sin\psi\cos\delta\,. \tag{4.32}$$

The polarization ellipse with semiaxes a and b, and angle ψ is illustrated in Figure 4.2.

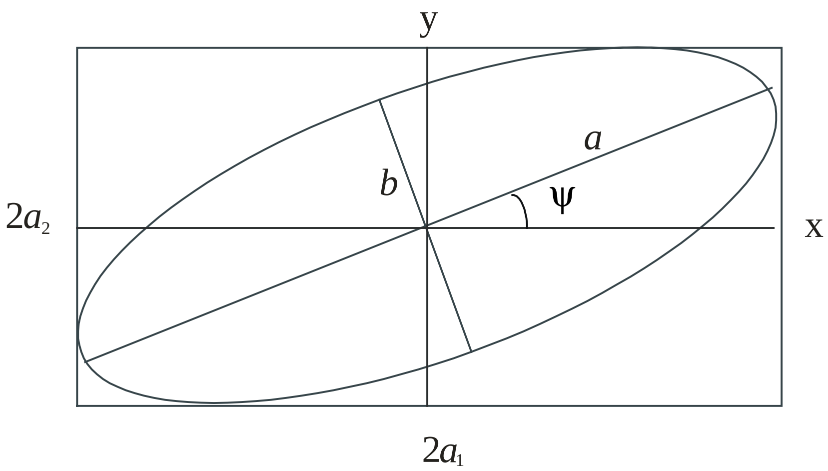

Figure 4.2 The polarization ellipse with semiaxes *a* and *b*, and angle ψ.

4.3.4 Stacked SWG's Analysis

In the analysis of the stacked SWG's, the two SWG's were treated as cascaded bulk components. Each component was assigned a Jones matrix with the elements derived from RCWA simulations of the individual components. There can however be some arbitrariness as to how to divide the SWG stack into two components. As shown in Figure 4.3, the multi-layer configuration of the stack consists of the substrate, QWP, planarization layer, polarizer, and ambient regions. The approach chosen in this analysis is to consider the QWP component as the configuration when the polarizer layer is removed from the stack. Similarly, the polarizer is chosen to be the configuration when the QWP layer is removed from the stack. This manner of dividing the stack was desirable because it was consistent with the design of the individual SWG components, i.e., the form birefringent QWP in Chapter 5 and the wire grid polarizer in Chapter 6.

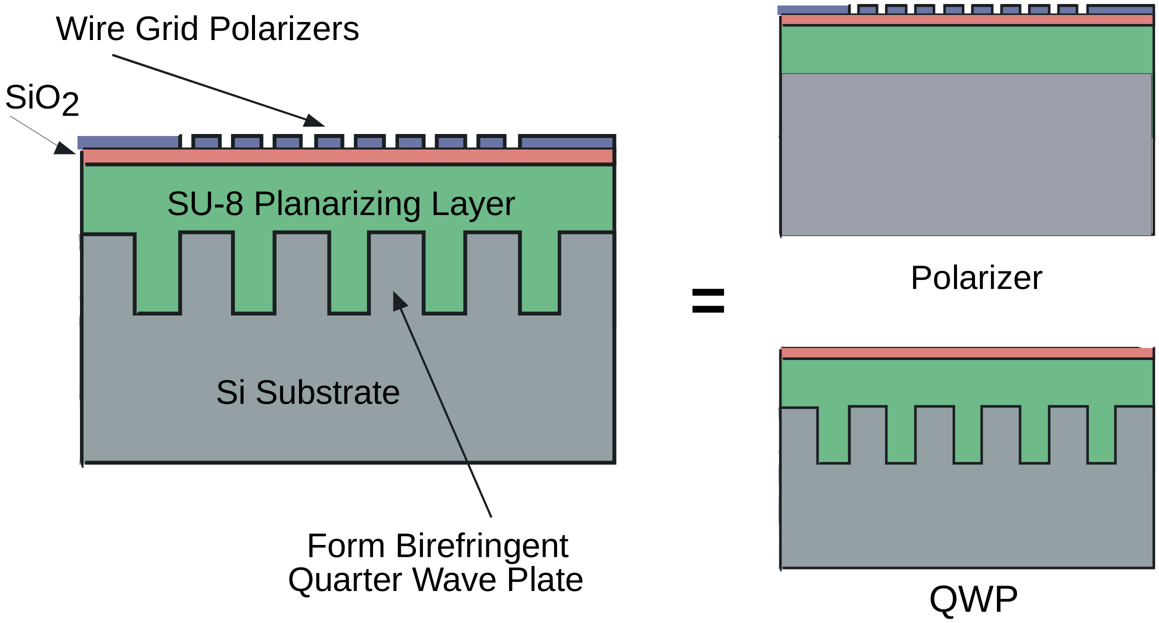

Figure 4.3 Stack divided into QWP and polarizer structures for Jones Matrix analysis.

4.4 Stacked Rotated Grating RCWA

The analysis of the subwavelength stack consisting of the form birefringent QWP and wire grid polarizer was performed using a rigorous algorithm called Stack Rotated Grating RCWA (SRG-RCWA). An overview of this method will only be described here and the reader can find the complete exposition in Jiang's doctoral dissertation [18]. The technique is used to model a multi-layer grating stack in which the gratings are one-dimensional uniform gratings that have arbitrary angular orientations and structural parameters. The technique is unique from other rigorous diffraction models in the literature because it is able to analyze more than two such grating layers. The treatment of a multi-layer grating stack is a three-dimensional grating diffraction problem and is based on a three-dimensional RCWA algorithm.

4.4.1 Overview of SRG-RCWA Method

The algorithm of SRG-RCWA is similar to the RCWA algorithm described above. The periodic relative permittivity of each grating layer is expanded as a Fourier series. The electric and magnetic fields in the 3 regions (incident, grating, and exit) are expanded into space harmonic fields. The set of coupled wave equations (arising from Maxwell's equations) is solved by calculating the eigenvalues and eigenvectors of the associated matrix and those quantities are used to express the space harmonics of the tangential fields in the grating region. From boundary conditions, the tangential electric and magnetic fields are matched at the interfaces using the computed space harmonics. The amplitude of the reflected and transmitted fields are calculated using the enhanced transmittance matrix method to efficiently compute a large number of layers. Diffraction efficiencies are calculated from the field amplitudes.

The expansion of the periodic relative permittivity into Fourier components is different from the traditional 3-D RCWA representations which can only handle grating layers having the same period in the x and y directions. To treat gratings which have different grating periods and arbitrary angular orientations, the SRG-RCWA algorithm uses a Fourier expansion in terms of sampling frequencies f_{sx} and f_{sy}. Arbitrary sampling frequencies f_{sx} and f_{sy} are chosen along the x and y direction such that a rectangular sampling lattice in frequency space can span all the diffracted orders generated by all the 1-D gratings in the stack. A suitable choice will allow the permittivities of all the gratings to be expanded into a Fourier series of f_{sx} and f_{sy} harmonics.

An example is given here of the SWG stack to illustrate how the grating parameters are related to the sampling frequencies f_{sx} and f_{sy}. Figure 4.4 shows a diagram in frequency space of a stack consisting of 3 gratings which have different grating periods and angular orientations. The k-vector of the gratings can be expressed in terms of the f_{sx} and f_{sy} unit vectors (spacings) in the f_x

and f$_y$ directions. The projections are integers n_x and n_y which are called the sampling numbers. The period of a grating is given as

$$\Lambda = \frac{1}{[(n_x f_{sx})^2 + (n_y f_{sy})^2]^{1/2}} \ , \tag{4.33}$$

and the angle β between a grating k-vector and f$_x$ axis is calculated from

$$\sin\beta = \frac{n_y f_{sy}}{[(n_x f_{sx})^2 + (n_y f_{sy})^2]^{1/2}} = n_y f_{sy} \cdot \Lambda \ . \tag{4.34}$$

If the sampling frequencies are chosen as

$$f_{sx} = f_{sy} = 1\,\mu\text{m}^{-1}, \tag{4.35}$$

then the parameters of the 3 gratings shown in the figure are

Grating 1: n_x =1, n_y=3, Λ=0.316 μm, β=71.4°.

Grating 2: n_x =2, n_y =1, Λ=0.447 μm, β=63.4°.

Grating 2: n_x =1, n_y =-1, Λ=0.707 μm, β=-45°.

In performing analysis and design of stacked gratings, the grating parameters are given and the sampling frequencies (f_{sx}, f_{sy}) and sampling numbers (n_x, n_y) need to be determined. The f$_x$ axis is chosen to coincide with one of the gratings in the stack, and then a pair of (f_{sx}, f_{sy}) is chosen and n_x and n_y are calculated for each grating. A dominant factor in making the choice is to minimize the n_x and n_y values so as to improve computational efficiency. It would be practical to choose low sampling numbers that only approximate actual grating parameters in order to perform simulations in a reasonable amount of time. For some configurations, the algorithm will not be able to produce the sampling quantities that allow the exact grating parameters of all the grating layers to be satisfied. This is the limitation of the method and values will then be used that best approximate the grating parameters.

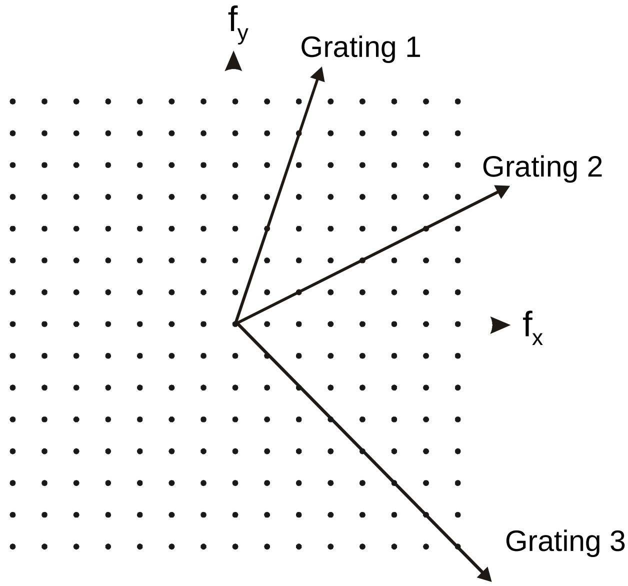

Figure 4.4 SWG stack consisting of 3 arbitrary gratings represented in frequency space.

4.5 Conclusion

In this chapter, approximate and rigorous methods to analyze SWG structures were presented. Effective medium theory is useful only when the grating period is sufficiently smaller than the incident wavelength such that the representation of the SWG as a uniaxial homogeneous film layer is valid. The resultant representation of the SWG as a film layer or multi-layer of films is then handled by the Berreman method for propagation through stratified films. Rigorous coupled wave analysis is a widely used rigorous technique for the analysis of grating structures.

A 2-D RCWA algorithm was used for the design and analysis of both the QWP and the wire grid polarizer components.

The Jones Matrix analysis was applied in several areas. We derived the extinction ratio of a polarizer sample from the measurement with another polarizer having a finite extinction ratio. The Jones analysis was also used in specifying the parameters of the polarization ellipse. The testing of the circular polarizers required illumination with RCP and LCP states; however, due to the use of non-ideal QWP and polarizer components for generating the desired circular inputs, the actual incident polarization states were elliptically polarized. The elliptical parameters were calculated with Jones Matrix analysis. In addition, the stacking of the SWG structures, QWP and polarizer, was studied using the Jones Matrix calculus by treating the stack as two cascaded bulk components. In this approximation, multi-layer interactions between the SWG components were ignored. The Jones matrices for the individual components were obtained from the 2-D RCWA analysis results.

The rigorous method to analyze the SWG stack is the SRG-RCWA. It is based on a 3-D RCWA algorithm that was modified to allow the treatment of multi-layer 1-D gratings having different structural parameters and angular orientations. Multiple reflections throughout the grating region are considered.

Chapter 5

BROADBAND FORM BIREFRINGENT QUARTER-WAVE PLATE

Subwavelength gratings are attractive for compact implementations of polarization-sensitive devices such as wave plates, wire grid polarizers and polarizing beam splitters. The fabrication processes involved are compatible with those of the semiconductor industry and therefore benefit from technological advances. The continuing drive to reduce feature size is instrumental in the development of these grating structures and the feasibility of using them. Fabrication of wave plates for *single wavelength operation* has been achieved using surface relief structures in silicon nitride [1], GaAs [6], and amorphous silicon [25]. For broadband operation, Kikuta *et al.* [24] recently proposed a method of creating achromatic form birefringent wave plates by compensating for the usual 1/λ dependence of the phase retardance with the strong dispersion exhibited by form birefringence when the grating period is on the order of the optical wavelength. For example, in one of their design studies a retardation error of only 3° is predicted for a ± 10% change in wavelength.

We have reported the first physical implementation of a broadband form birefringent wave plate that makes use of form birefringence-based dispersion [65]. We have designed, fabricated and tested broadband quarter-wave plates for the 3.5 to 5 μm wavelength region. We investigated two quarter-wave plate designs that differ in the ambient medium for the groove material: 1) air and 2) a dielectric medium with refractive index approximately equal to 1.5. In the second case, the dielectric medium also serves as a planarization layer which allows a attractive method for integrating subwavelength gratings by multi-layer stacking. In this chapter, we present the development of the first structure of the SWG stack, the broadband form birefringent QWP.

5.1 Design of Broadband Form Birefringent Quarter-Wave Plates

The design of the broadband form birefringent QWP was approached using two simulation methods: rigourous coupled wave analysis (RCWA) and effective medium theory (EMT). Effective medium theory is an approximate method which is accurate when the grating period is sufficiently small compared to the incident wavelength. As discussed in Section 4.1, EMT simplifies the analysis of SWG's by treating the structures as uniaxial thin film layers which leads to less intensive computational calculations compared to RCWA. Results can be used to provide a starting point for the rigorous method, as well as yield insight into the performance of the component. The extension to multi-layer SWG's was treated by the multi-layer thin film formulations such as those of Yeh [60] and Berrreman [61].

In the simulations, we examine the effects of several parameters on the phase retardance and transmittance of the subwavelength grating. As illustrated in Figure 5.1, these parameters are the grating period Λ, fill factor f (=a/Λ), and thickness t. The substrate is silicon and the ambient medium has index n_a. Normally incident illumination is assumed, and the polarization states of TE and TM correspond to the electric field parallel and perpendicular, respectively, to the grating ridges. The refractive index of silicon found in The Infrared Handbook [66] was used in the RCWA calculations. The index of an SU-8 planazing layer used in the simulations was obtained from samples measured by J. A. Woolam Company.

Based on the circular polarization filter design (discussed later in Section 7.1.1), we desired to achieve a phase retardance of $0.5\pi \pm -0.1\pi$ over the 3.5 to 5 μm wavelength range. We systematically varied the values of the grating period, fill factor and thickness, and examined the dispersion of the effective refractive indices. Optimum parameters were determined when this dispersion adequately compensated for the 1/λ dependence of the phase retardance. Afterwards, we characterized the sensitivity of the retardance to small fabrication errors involving the grating fill factor and thickness.

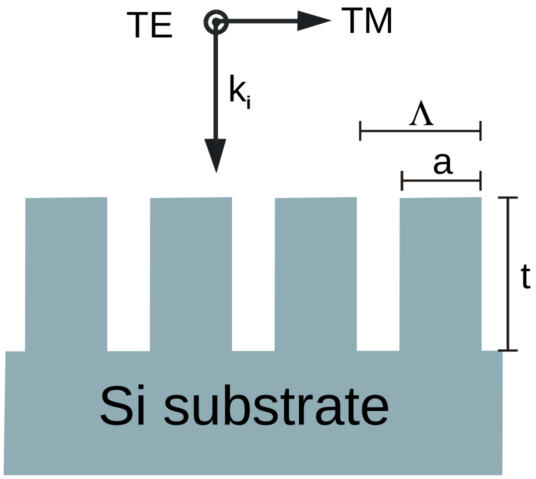

Figure 5.1 Schematic diagram of a form birefringent wave plate and a normally incident beam showing TE and TM polarization definitions.

5.1.1 QWP Design: Silicon-Air Interface

The RCWA and EMT methods were used in the simulations to design a broadband QWP grating in an ambient medium of air. The phase retardance and transmittance are plotted as a function of wavelength. The grating period was chosen to be sufficiently small to satisfy the subwavelength condition of propagating only the 0^{th} order. (For normally incident illumination, this condition is met if the grating period is less than λ_{min}/n_{Si} = 1.02 μm in which λ_{min}= 3.5 μm and the refractive index of silicon is 3.42.) The grating period was chosen to be 1 μm. By systematically, varying grating parameters of fill factor and thickness, we determined optimal values that achieve achromatic behavior across the 3.5 to 5 μm wavelength range. The optimum achromatic performance occurred for grating parameters near the values: period = 1 μm, fill factor = 66% and thickness = 1.25 μm.

The tolerance on fabrication error was determined by plotting the fill factor and thickness values which satisfy the retardance tolerance ($0.5\pi \pm 0.1\pi$). As shown in Figure 5.2(a), for a given grating thickness of 1.25 μm, only a narrow range of fill factors (64-68%, which corresponds to a trench width tolerance of ± 20 nm) satisfactorily meets this criteria. The corresponding tolerance on etch depth tolerance, Figure 5.2(b), is less severe (± 50 nm), for a given fill factor of 66%. Clearly a tight control of the fill factor is essential for the successful fabrication of a broadband structure. For optimum value of the grating parameters, the retardance across the wavelength range is within 0.45π to 0.54π. The TE and TM transmission through this grating layer is shown in Figure 5.3.

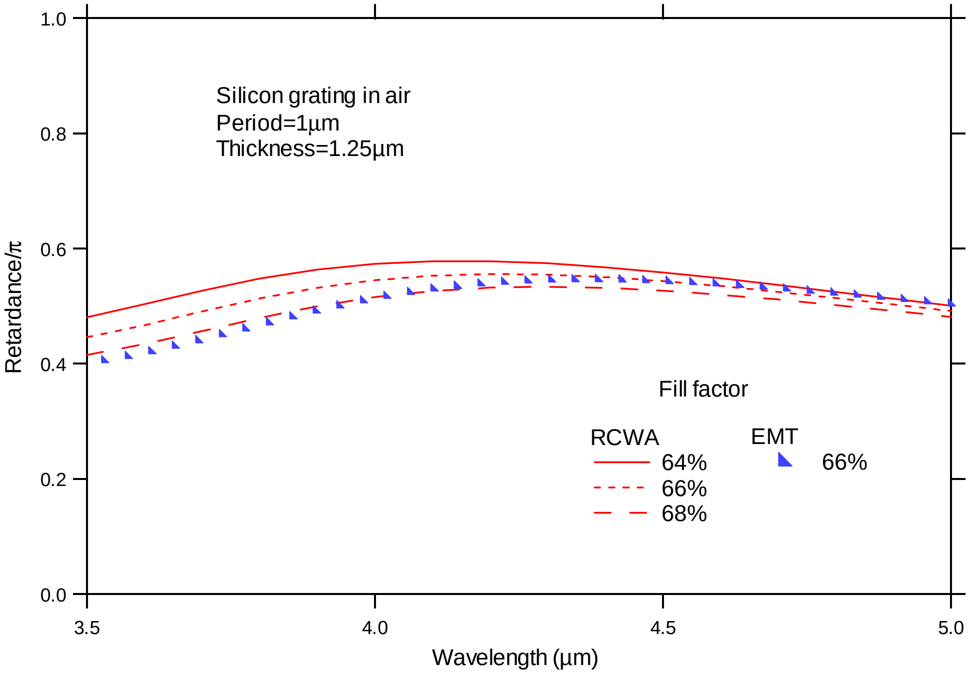

(a)

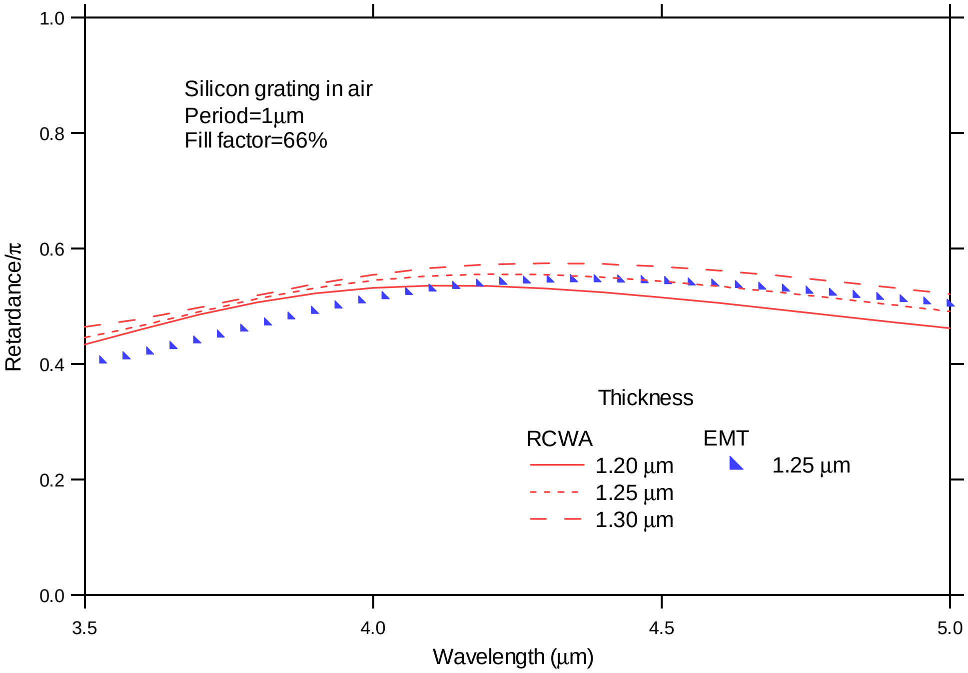

(b)

Figure 5.2 Phase retardance of QWP in air as a function of wavelength for 1.0 µm period gratings parametrized by (a) fill factor (for thickness of 1.25 µm) and (b) thickness (for fill factor of 66%).

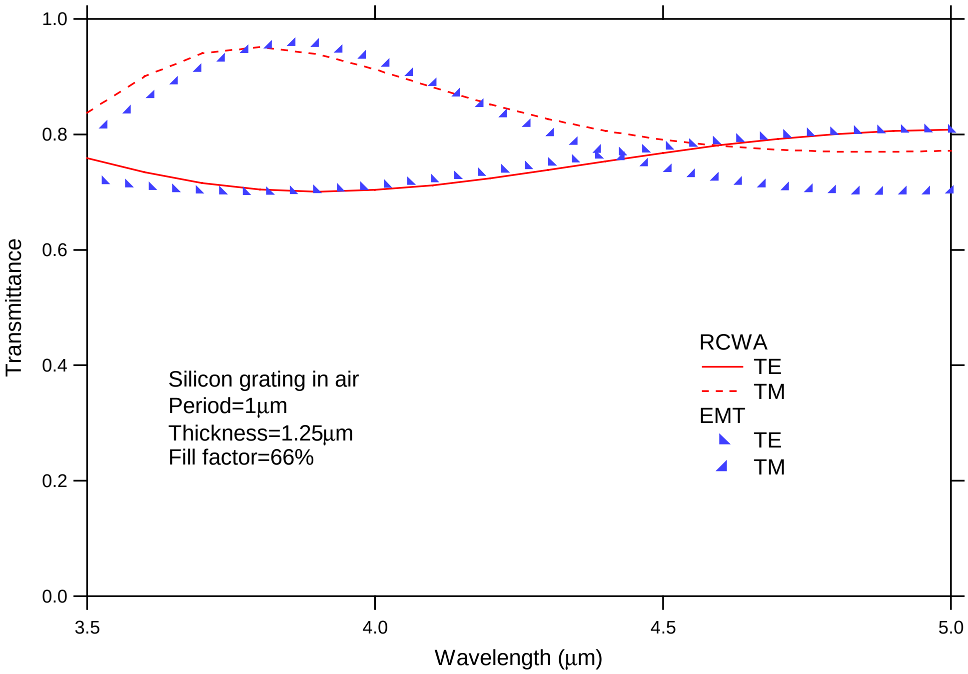

Figure 5.3 Transmittance as function of wavelength for given fill factor and thickness values of 66% and 1.25 μm, respectively.

5.1.2 QWP Design: Silicon-Dielectric Interface

The RCWA and EMT methods were used in the simulations to design a broadband QWP grating for a dielectric ambient medium with a refractive index: of 1.5. The phase retardance and transmittance are plotted as a function of wavelength. The grating period was chosen to be 1 μm. Optimum achromatic performance occurred for grating parameters near the following values: period = 1 μm, fill factor = 66%, and thickness = 2.15 μm. Tolerance on fabrication errors due to fill factor and thickness was not as severe as that of the grating in air. In Figure 5.4, the fill factor range satisfying the retardance criteria extended from 62% to 76% (for a thickness of 2.15 μm), which correspond to a trench width tolerance of ± 70 nm. The etch depth tolerance is also less severe at ± 150 nm (for fill factor of 68%). Although a more challenging task in fabrication is required which involves anisotropic etching of deep and high aspect ratio (defined as groove height/groove width) gratings, the design of the QWP produced wider tolerances on fabrication error than the grating in air. Using optimum parameter values, the retardance across the wavelength range is extremely good in which values are within 0.48π to 0.52π. The transmission through this grating layer is shown in Figure 5.5. The transmission values of TE and TM polarizations range from 85% to 99%, which is generally greater than the transmission through the grating in air.

5.2 Fabrication of Broadband Form Birefringent Quarter-Wave Plates

The form birefringent quarter-wave plates are fabricated on the surface of 75mm diameter p-type <100> silicon substrates having a resistivity of 1-20 ohm-cm. Photolithography was done in a contact mask aligner (made by AB-Manufacturing) with a mercury arc lamp source. A 5” x 5” dark-field photomask is used with 1.3 cm x 1.3 cm of grating region area in the mask center composed of 500 nm wide chrome lines and spaces. An epoxy-based, near-UV negative resist, SU-8 2, was used as the dielectric medium. The schematic of the grating fabrication is shown in Figure 5.6 and described in the following sections.

5.2.1 QWP Fabrication: Silicon-Air Interface

Wafers were prepared for photolithography by first immersing (with ultrasonic agitation) in an aqueous-based adhesion promoter (Surpass 1000 from DisChem, Inc.) for 1 minute and spun dry. A 500 nm layer of Shipley 1805 photoresist is next spin coated and then soft-baked at 115° C for one minute on a vacuum hotplate.

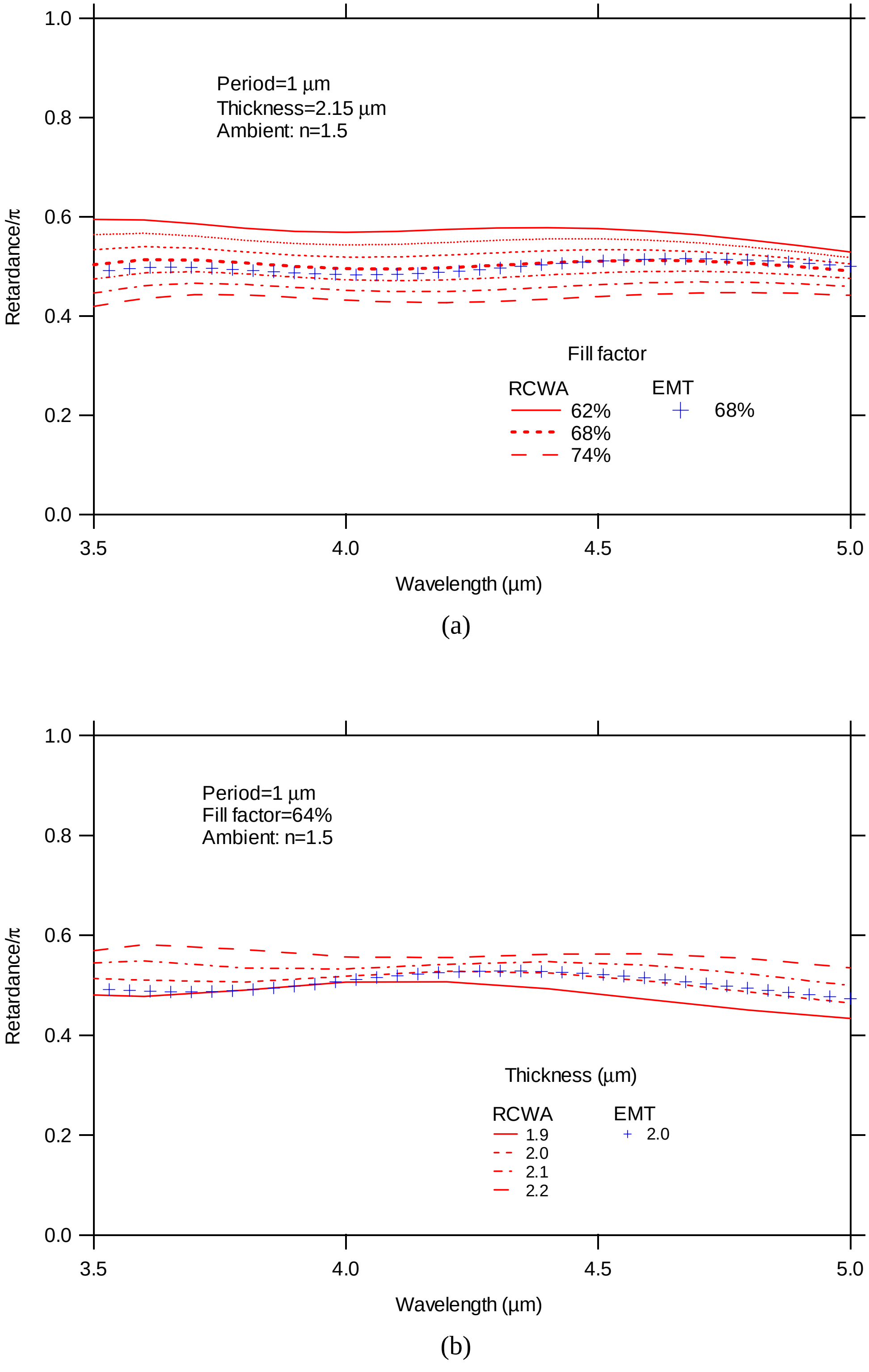

Figure 5.4 Phase retardance of QWP in ambient medium, n=1.5, as a function of wavelength for 1 µm period gratings parametrized by (a) fill factor (for thickness of 2.15 µm) and (b) thickness (for fill factor of 64%).

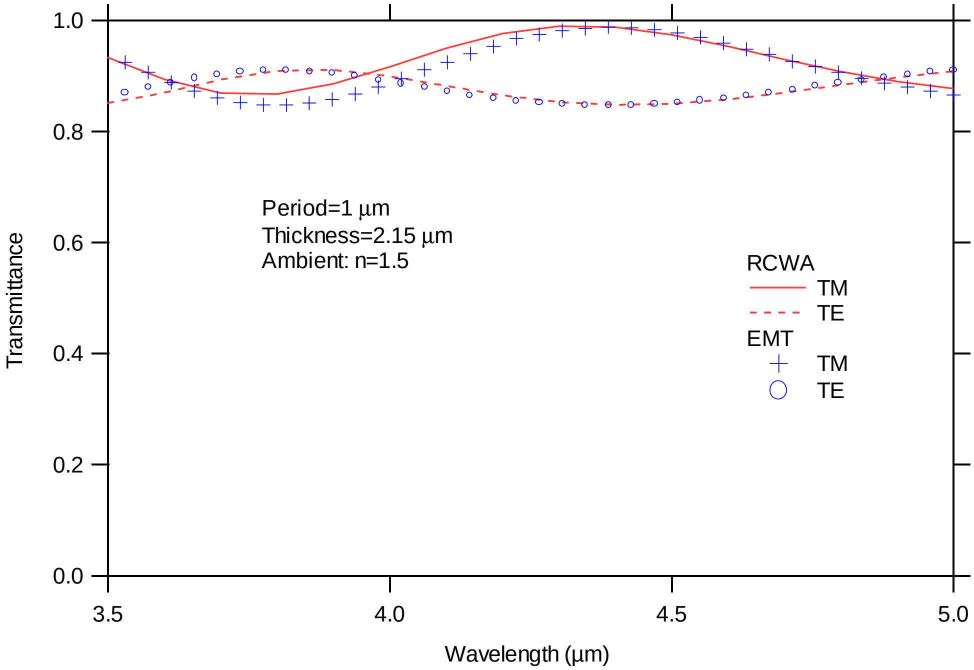

Figure 5.5 Transmittance as a function of wavelength using fill factor and thickness values of 68% and 2.15 µm, respectively.

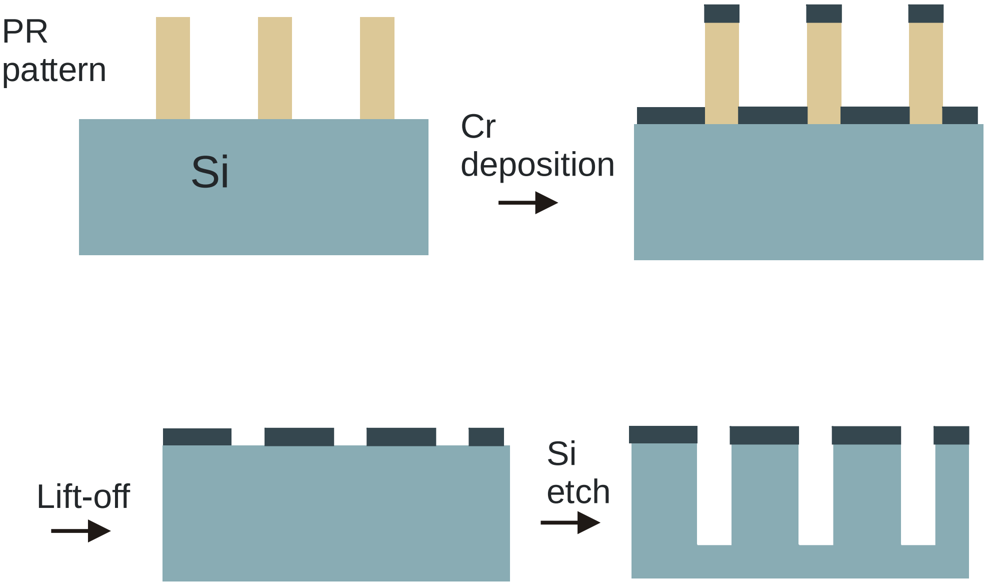

Figure 5.6 Schematic of the silicon grating fabrication process.

Vacuum contact printing of small feature sizes, such as the 500 nm lines and spaces of the photomask used here, poses significant challenges. We have however been able to consistently achieve uniform and well-defined grating patterns in photoresist over nearly the whole 1.3 cm x 1.3 cm grating area defined on our mask. A critical factor is turning off the substrate vacuum prior to exposure which allows better vacuum contact between the mask and the wafer. Furthermore, by carefully controlling the exposure, we are able to tightly control the photoresist fill factor which is a critical precursor to achieving the desired silicon grating fill factor. For example, as shown in Figure 5.7(a), we found that an exposure of 3.3 seconds (for measured intensities at 365 nm and 405 nm of 16 mW/cm^2 and 9.9m W/cm^2, respectively) and a 1 minute development time in Microposit 352 developer resulted in a grating pattern with an approximately 30% photoresist fill factor.

After photoresist patterning, a lift-off method was used to create a chrome mask for plasma etching the silicon substrate, as seen in Figure 5.7(b). To assure good adhesion between the chrome and the substrate, a short oxygen plasma etch in the RIE is employed to remove any residual photoresist present after development. A 250 nm thick chrome layer is deposited over the patterned photoresist, following which the wafer is immersed (with ultrasonic agitation) in hot (160° F) Microposit 1165 Remover for lift-off. Gentle wiping of the surface with a soft cloth is helpful in achieving lift-off.

The grating pattern is transferred to the silicon substrate by reactive ion etching using a Plasma-Therm 790 system with 9.5” diameter electrodes. We used a graphite electrode cover plate. A gas chemistry of trifluoromethane (CHF_3) and sulfur-hexafluoride (SF_6) was used to achieve an anisotropic etch based on polymer sidewall passivation [40]. The process parameters include the gas flow rates of 34 and 6 sccm for the CHF_3 and SF_6 gases, an RF power of 125 W

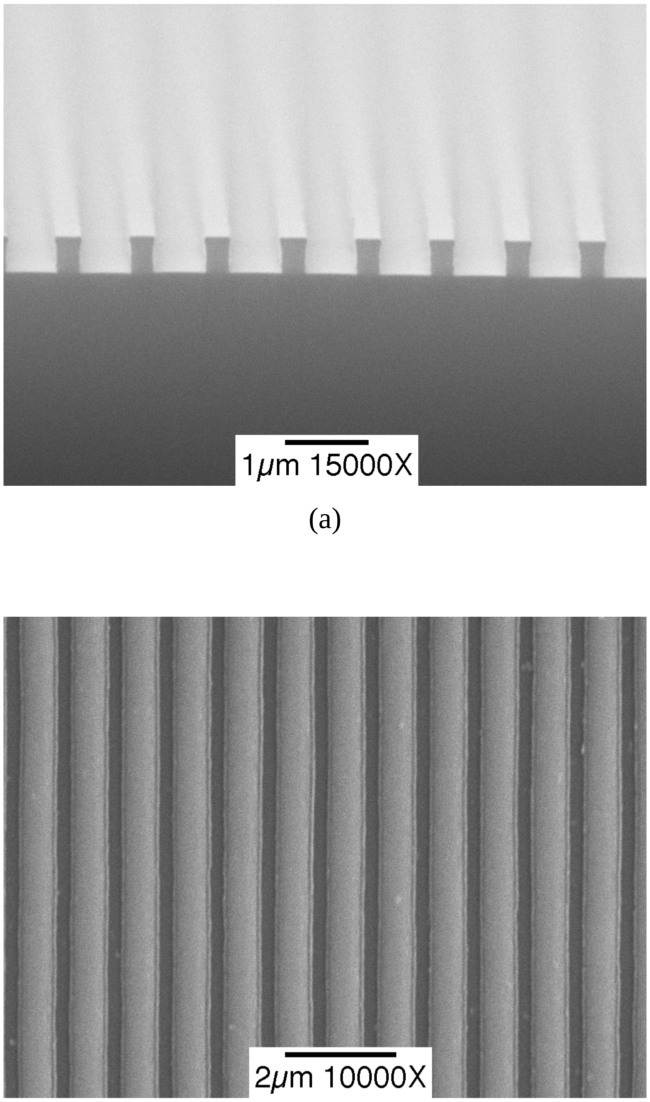

(a)

(b)

Figure 5.7 (a) Scanning electron microscope (SEM) cross section image of a photoresist grating on Si. (b) SEM top view image of Cr etch mask (on Si) with a Cr fill factor of ~70%.

(0.27 W/cm^2) and a pressure of 10 mTorr. This results in a Si etch rate of 16 nm/min. A typical grating cross section is shown in Figure 5.8. The etch depth is approximately 1.23 μm and the sidewalls are slightly sloped. There is also some evidence of redeposited silicon on the upper sidewalls.

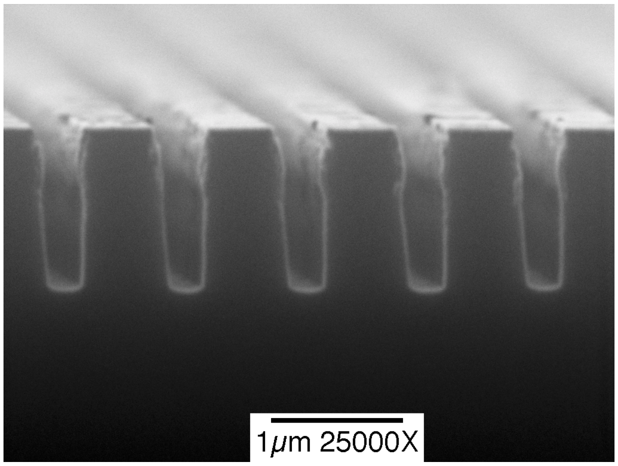

Figure 5.8 An SEM cross-sectional image of an etched Si grating.

5.2.2 QWP Fabrication: Silicon-Dielectric Interface

The procedure for fabricating the QWP having a dielectric ambient medium is a slightly modified version of the previous process. The dielectric material chosen was SU-8, and epoxy-based, negative resist. Wafers were prepared for photolithography by applying an anti-reflective coating (ARC XL-20 from Brewer Science) on the surface of the silicon substrate to reduce standing waves within the resist layer arising from multiple reflections. The ARC layer also serves as an adhesion base for the resist. These two properties of ARC improved the yield in the photoresist patterning. A 500 nm layer of Shipley 1805 photoresist is next spin-coated and then soft-baked at 115° C for one minute on a vacuum hotplate.

The exposure time is increased to allow for an even smaller resist fill factor (which results in larger chrome fill factor) to accommodate the longer etch time in fabricating the deep silicon grating. With the same source intensity as given above, an exposure time of 4.5 seconds produced photoresist grating patterns having an approximate 20% fill factor value. An anisotropic polyimide etch in the RIE is used to transfer the resist pattern to the ARC layer. A gas chemistry of helium and oxygen is used, with 8 sccm flow rates for each gas, RF power of 175 W, 10 mTorr pressure and an etch time of 3 minutes. A 250 nm thick chrome layer is deposited over the patterned photoresist and ARC layers, and the lift-off procedure follows.

The grating pattern is transferred to the silicon substrate by reactive ion etching using a two-step process. The first step involves a gas chemistry of CHF_3 and SF_6 similar to the previous etch except for a different gas flow ratio to achieve even more anisotropy in the etch. This was accomplished by inducing more polymer sidewall passivation by increasing the number of CH, CHF and CHF_2 species present with respect to the free F radicals that attack silicon atoms isotropically. This is accomplished by increasing the flow of CHF_3. The process parameters are gas flow rates of 35 and 5 sccm for CHF_3 and SF_6, respectively, 125 W RF power, 10mTorr chamber pressure, and an etch time of 90 minutes. The second etch step is to use CF_4 gas. The reduction of the number of free F radicals accomplished by removing the SF_6 gas increased the anisotropy in the etch, but resulted in a lower etch rate. The process parameters are 40 sccm flow rate, 125 W power, 10 mTorr pressure and 70 minute etch time. The silicon etch rate averages to 12.5 nm/min. With our 9.5” electrode, 3 wafers can be etched simultaneously by slightly increasing (by 6.25 minutes or 4%) the etch time. The etch results in a grating depth of approximately 2.0 μm and the sidewalls are slightly sloped, as shown in Figure 5.9(a).

5.2.3 Planarization of Silicon Grating

Planarization of the silicon grating is essential to the fabrication of multi-layer structures. SU-8 is an excellent choice because it planarizes the surface relief adequately and is resistant to acetone and other photoresist strippers such as Microposit 1165 Remover. This resistance allows subsequent multiple processes involving the use of photoresist strippers. These processes included multiple lift-off steps to form the micropolarizer array. SU-8 also functions as a hard dielectric coat to protect the delicate grating structure.

Table 5.1 lists the process steps for planarization of our form birefringent QWP silicon gratings. This results in an SU-8 planarization layer approximately 1.3 microns thick above the grating structure. A typical grating cross section is shown in Figure 5.9(b).

Table 5.1 The SU-8 planarization process.

1. Spin-coat: 2800 RPM, ramp 560 rev/s, 20 seconds
2. Softbake: 90°C, 30 seconds float with N_2, then 90 seconds contact vacuum
3. Flood expose: 36 seconds
4. Post-exposure bake: 90°C, 5 minutes
5. Development: P-type thinner, 45 seconds
6. Hardbake: 200°C, 2 minutes

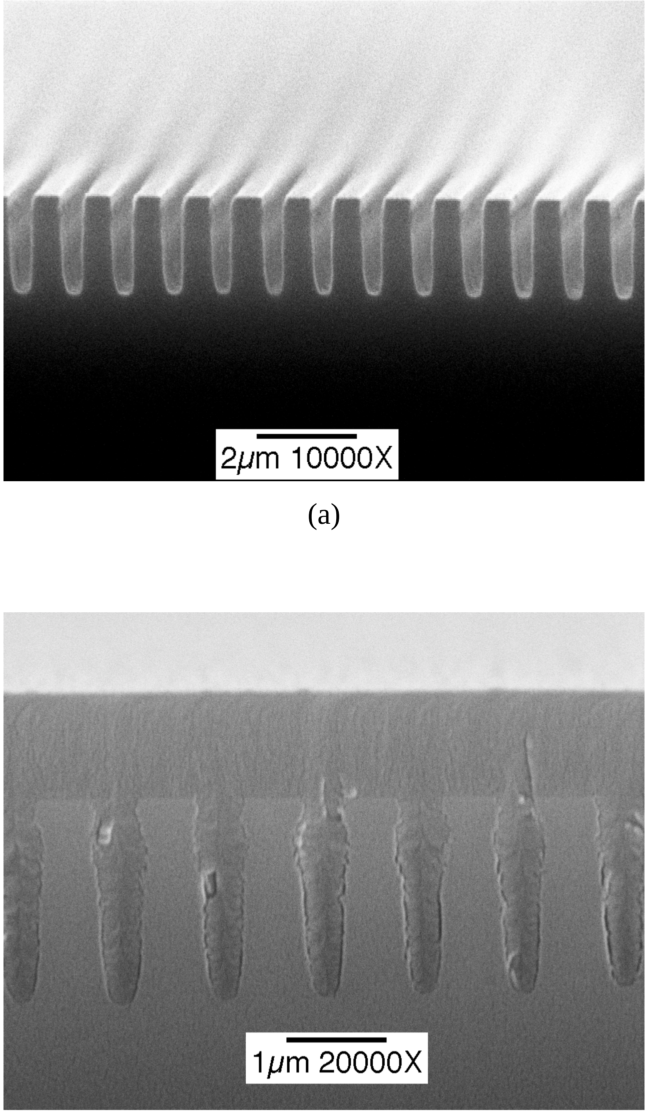

(a)

(b)

Figure 5.9 An SEM cross-sectional image of (a) an etched Si grating and (b) subsequent planarization using SU-8.

5.3 Performance of Broadband Form Birefringent Quarter-Wave Plates

In this section, we discuss the optical performance of the fabricated subwavelength gratings. An FTIR-based spectropolarimeter [67] and an FTIR spectrometer (FTS60A from BioRad) were used to measure the phase retardance and transmittance of the TE and TM modes. Since the backside of the silicon wafers were not anti-reflection coated, a 30% Fresnel reflection loss at this interface significantly reduced the transmittance values. Measurements are compared with simulations using RCWA and EMT of the etched profiles approximated as multi-layer, binary gratings.

5.3.1 QWP Performance: Silicon-Air Interface

The Si grating shown in Figure 5.8 was approximated as a multi-layer binary grating structure using the layer parameters listed in Table 5.2. As illustrated in Figure 5.10(a), the quarter-wave plate designed for an ambient medium of air was measured to have a phase retardance that varies from 0.49π to 0.57π (or 89° to 102°) over the 3.5 μm to 5 μm wavelength range. The RCWA and EMT results compare well with experimental measurement.

The transmission measurements and corresponding RCWA and EMT simulations are given in Figure 5.10(b). Using the FTIR-based spectropolarimeter, the TE and TM transmissions of the quarter-wave plate in air were measured to be between 55% and 62%. The RCWA and EMT results are in agreement.

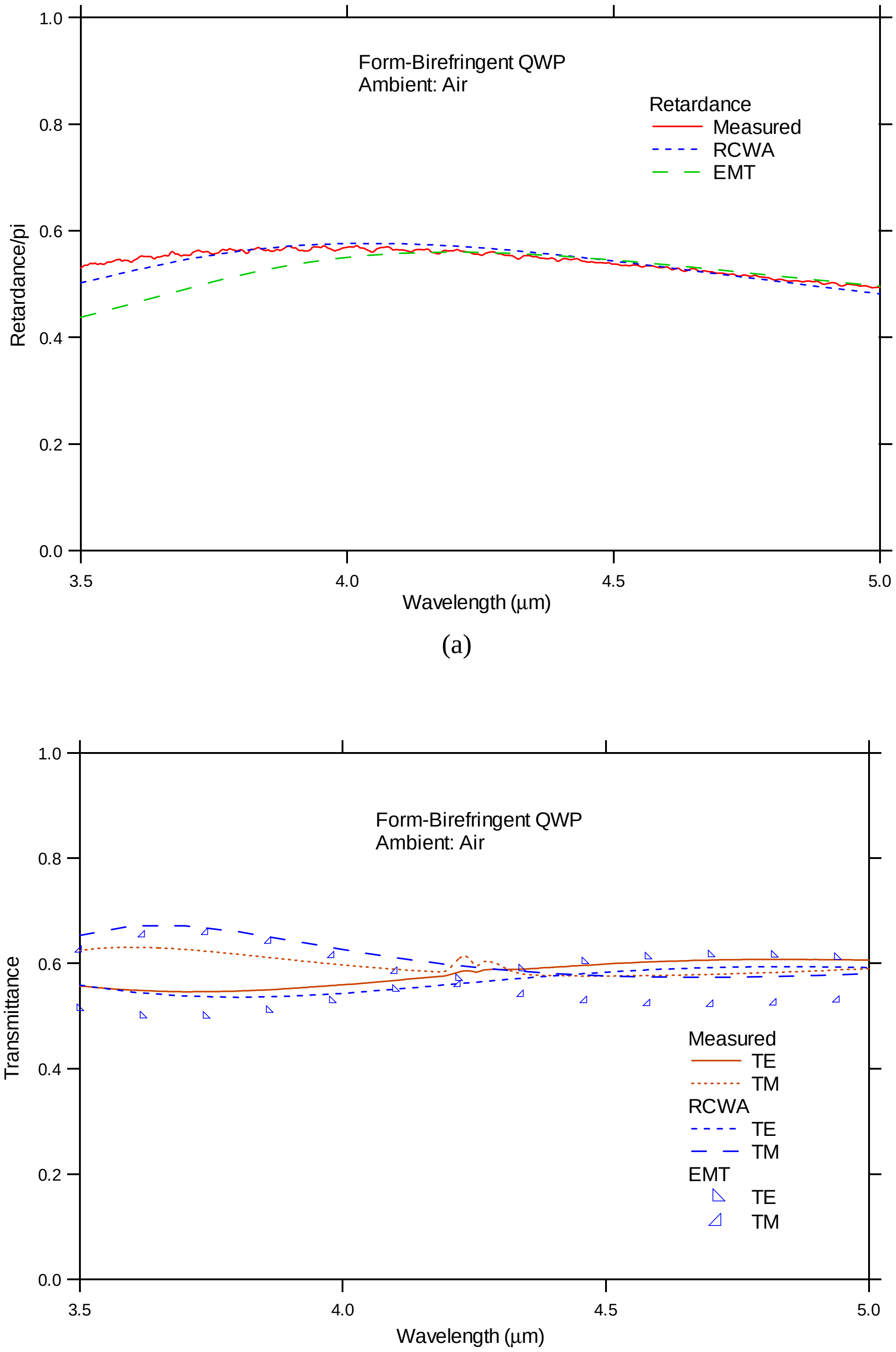

(a)

(b)

Figure 5.10 (a) Measured and simulated phase retardance as a function of wavelength and (b) the corresponding TE and TM transmittance.

Table 5.2 RCWA and EMT parameters for grating in air.

Layer	Thickness (μm)	Width (μm)
1	0.28	0.67
2	0.27	0.62
3	0.22	0.60
4	0.10	0.62
5	0.24	0.63
6	0.11	0.67

5.3.2 QWP Performance: Silicon-SU-8 Interface

The Si grating shown in Figure 5.9(b) was approximated as a multi-layer binary grating structure using the layer parameters listed in Table 5.3. Figure 5.11 shows the phase retardance of the quarter-wave plate planarized by SU-8 in which a range from 0.45π to 0.53π is measured. The TE and TM transmittances were determined to vary between 53% and 68%. The retardance and transmittance measurements are in excellent agreement with RCWA and EMT simulation results.

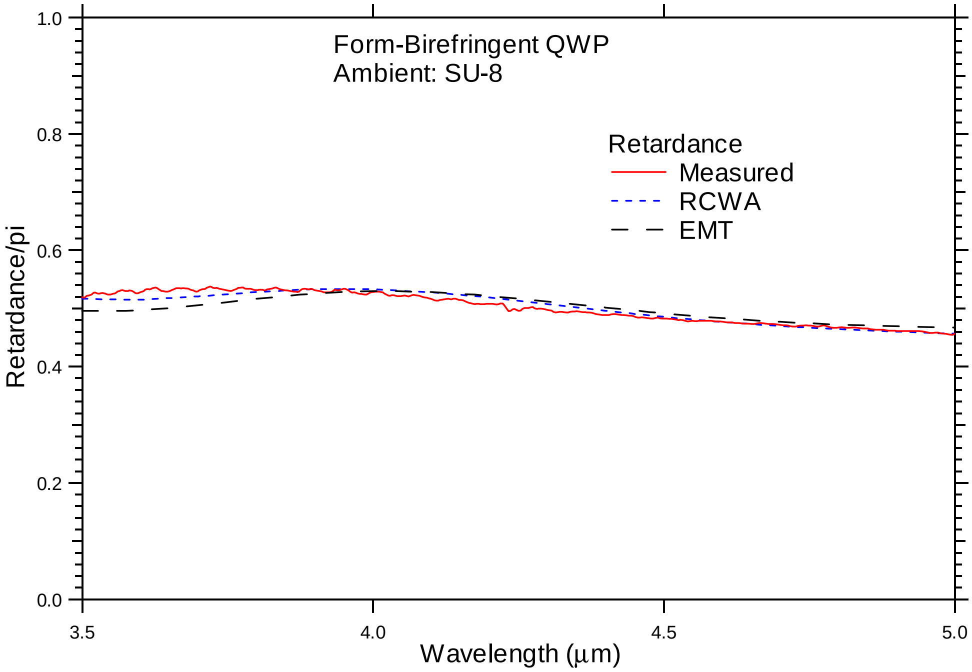

(a)

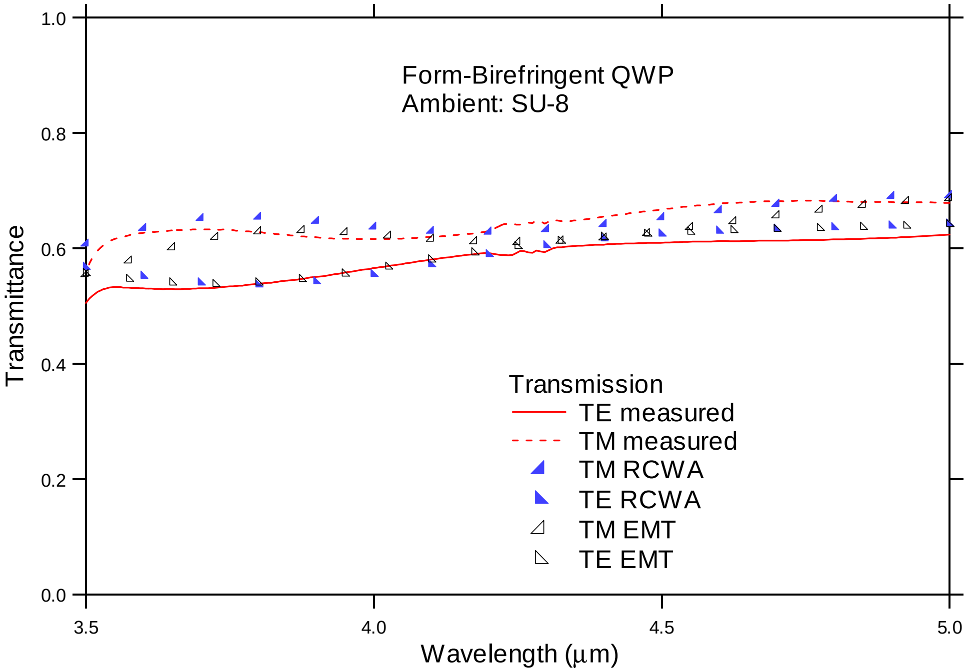

(b)

Figure 5.11 (a) Measured and simulated phase retardance as a function of wavelength and (b) the corresponding TE and TM transmittances.

Table 5.3 RCWA and EMT parameters for grating in SU-8.

Layer	Thickness (μm)	Width (μm)
1	0.363	0.569
2	0.363	0.541
3	0.363	0.569
4	0.363	0.618
5	0.363	0.668
6	0.174	0.769

5.4 Summary

We have designed, fabricated and measured the optical performance of subwavelength gratings for use as broadband quarter-wave plates over the 3.5 to 5 μm wavelength region. Dispersion of the effective refractive indices when the grating period is on the order of the wavelength is clearly an effective method of compensating for the usual 1/λ dependence of the phase retardance as long as the grating parameters are carefully controlled in the fabrication process. Such grating structures offer an attractive and flexible method of implementing broadband wave plates in the infrared. The resultant device represents an attractive alternative to the only other mid-infrared achromatic wave plate currently available, which involves the use of two uniaxial materials [68]. Furthermore, planarized subwavelength gratings are attractive for multi-layer integration which results in the production of multi-functional integrated components.

Chapter 6

WIRE GRID POLARIZERS FOR THE MID-INFRARED WAVELENGTH REGION

In this chapter, different methods of fabricating a wire grid polarizer are investigated. Wire grid polarizers are commonly used as polarizing elements for the wavelength range of 1 to 1000 microns. Commercially available wire grid polarizers consist of a thin film metallic grid pattern deposited on suitable infrared substrates such as ZnSe, BaF_2, CaF_2, Ge, Polyester, and Polyethylene [69]. Two common methods of patterning the photoresist grating, which defines the subsequent metallic wire grid, is by interference lithography and contact printing. In interference lithography, a near-UV sensitive photoresist is exposed to an interference pattern created by the intersection of two laser beams. Grid periods as small as 0.25 μm are achieved in this manner [69]. For defining grid patterns with larger periods (generally, larger than 4 μm), it is adequate to use standard UV photolithography, such as contact lithography. For very fine grid periods, the use of electron-beam lithography can be used to generate feature sizes on the order of tens of nanometers. The method of metal deposition at an oblique angle on the photoresist grating is used to define the metallic grid pattern.

The application of imaging polarimetry requires an array of metallic wire grid polarizer filters and each unit cell consists of polarization filters at different angular orientations. Oblique angle deposition is only practical for the manufacture of large area (up to 71 mm) wire grid polarizers in one axis. The fabrication process should also be compatible with the QWP fabrication process such that the two components can be integrated by stacking to act as a circular polarization filter. We therefore investigate other methods that are suitable for fabricating the array of rotated wire grid polarizers which include reactive ion etching [70] of the metal along with lift-off [71]. In this chapter, we present the design, fabrication and performance of wire grid polarizers on silicon substrates for the 3.5 to 5 μm wavelength range. We investigated two wire grid polarizer designs which differ in their grid period. A 0.5 μm period polarizer can be suitably patterned using the method of interference lithography. A 1 μm period polarizer was also investigated because such a feature size can still be patterned using contact lithography. The fabrication process came directly from the development of the 1 μm period form birefringent QWP. Our objective was to produce a wire grid polarizer that performs with high extinction ratio and transmission performance in the 3.5 to 5 μm wavelength range. We have successfully developed polarizers that meet the requirements of the imaging polarimeter application and the results are discussed in the following sections. The two designs are labeled Polarizer I and II.

6.1 Wire Grid Polarizer I

We investigated the method of fabricating the wire grid polarizer using interference lithography for producing the grating pattern on photoresist that is subsequently transferred to the metal layer. Large areas can be patterned relatively fast and inexpensively by this method in comparison to electron beam lithography. By adequately expanding the beams, uniform exposures over an area of 1 cm^2 (required for the imaging polarimeter application) have been achieved in the following sections. Section 6.1.1 presents the design of Polarizer I consisting of 0.5 μm grid period. Section 6.1.2 presents the fabrication process using the interference lithography setup. The measured performance and RCWA analysis of the fabricated polarizer is discussed in Section 6.1.3.

6.1.1 Polarizer I: Design

The first wire grid polarizer design, referred to as Polarizer I, consists of a 0.5 μm grid period. The RCWA method is commonly applied to the analysis of diffraction gratings [62] and was used here in the design of the wire grid polarizers. The particular RCWA code used was written in Matlab by Chambers [63]. We characterized the performance of the metal grating as a function of the grating parameters of period, fill factor and thickness. We also studied the effect of inserting a low index medium between the substrate and the polarizer, which has a significant effect in the performance.

The EMT method is useful in the analysis of subwavelength gratings when the grating period is sufficiently small in comparison to the incident wavelength. This was shown to be valid for the QWP design in which the surface of the silicon substrate is patterned with a subwavelength grating structure. However, EMT analysis of subwavelength metal gratings is inaccurate except for very large wavelength to period ratios [57]. The EMT method was therefore not used in the design.

The metals, molybdenum (Mo) and chromium (Cr), are good candidates as wire grid polarizers because of their high reflectivity in the 3.5 to 5 μm wavelength range. Another important reason for choosing Mo is its suitability for RIE in a fluorine-based etch chemistry. The photoresist grating pattern is transferred to the Mo layer by RIE to fabricate the wire grid. Cr was chosen to act as an etch mask and also as a top layer wire grid.

In the following RCWA simulations, we investigated the performance of the wire grid polarizer as a function of the grating parameters: period fill factor and thickness. We also investigated the dependence on the use of a low index insertion layer sandwiched between the substrate and the metal gratings. The optical constants of Mo and Cr are acquired from sputtered sample measurements performed by J. A. Woolam Company. The fabrication process for Cr was later changed to an evaporation method and therefore there will be some discrepancy in the simulation results compared to measurement due to the approximation of using the optical constant of sputtered Cr for evaporated Cr. Assume normally incident illumination for all cases.

6.1.1.1 Wire Grid Simulations: Period

The 0th order should be the only order to propagate; therefore, the grating period must be chosen to be sufficiently small. Figure 6.1(a) shows the extinction ratio, $ER \equiv T_{TM}/T_{TE}$, dependence on period, Λ, for the case of a Mo wire grating on silicon. Sample values are chosen as (λ=4 µm, fill factor=50%, and thickness=0.2 µm). The grating is truly polarization sensitive at small periods, showing ER values as high as 16,000 at Λ=0.1 µm. As the period increases polarizer performance drops drastically to ER values close to 1. The kink in the curves corresponds to the threshold in which 1st order reflections begin to propagate when the grating period is equal to λ/n_{Si} (≈ 1.2). Figure 6.1(b) shows the transmission characteristics of the 0th diffraction order. It is also advantageous to use small grating periods to achieve high transmission (T_{TM}). The limiting factor in choosing grating period is feasibility of fabricating the small features. For example, a grating with a period of 0.5 µm, 50% fill factor and 0.2 µm Mo thickness has an ER of 300 and a transmission of 78%.

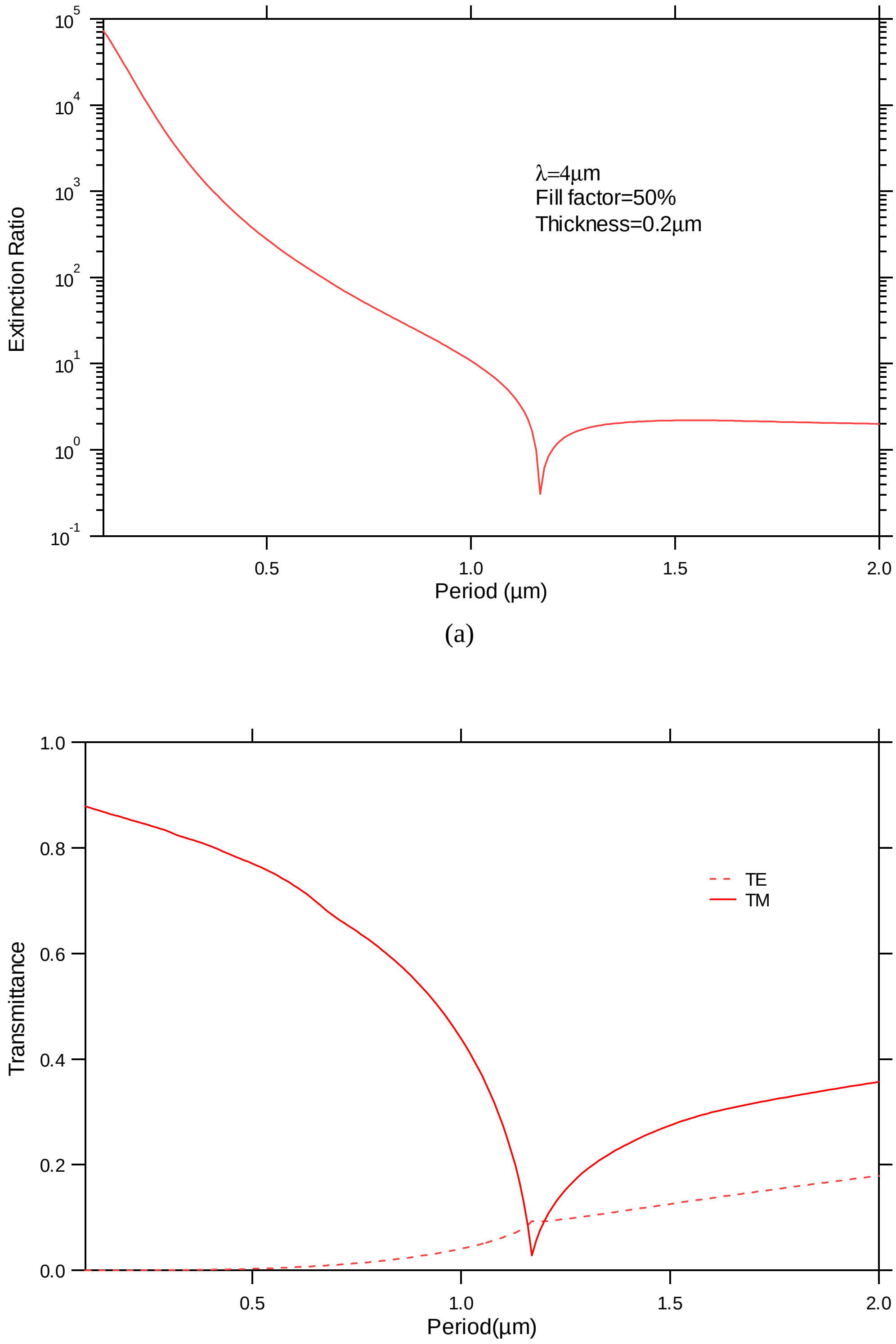

(a)

(b)

Figure 6.1 (a) Extinction ratio and (b) transmittance as a function of Mo grating period.

6.1.1.2 Wire Grid Simulations: Fill Factor

The effect of the fill factor on ER is next examined, as shown in Figure 6.2(a). The fill factors at the endpoints correspond to the grating becoming a uniform (metal or the layer cover medium), so the ER=1. In between, the ER is a strong function of fill factor, with the highest values occurring at large metal fill factors. Despite the high ER, however, the TM transmission coefficient is very low at this end, as seen in Figure 6.2(b). A trade-off therefore must be made between high ER and high transmission.

6.1.1.3 Wire Grid Simulations: Thickness

The effect of the metal grating thickness on ER is shown in Figure 6.3(a). The thicker the metal, the higher the ER. Figure 6.3(b) shows that in this thickness range, there is no penalty in the transmission of the TM for thicker wires, in fact it even increases somewhat. The maximum achievable wire grid thickness is then the limiting factor here, and this is set by fabrication considerations.

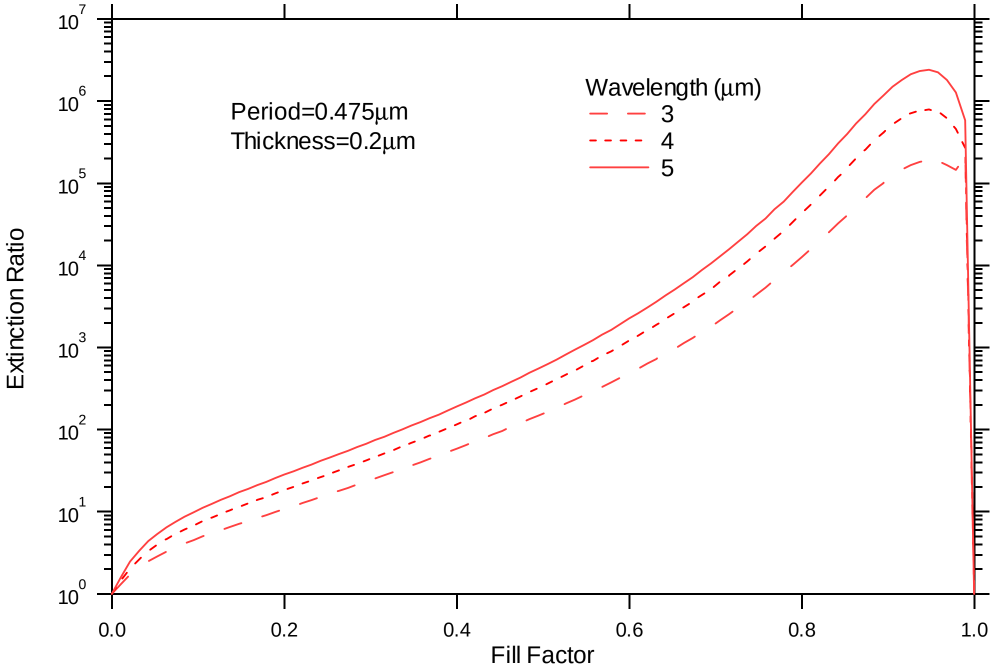

(a)

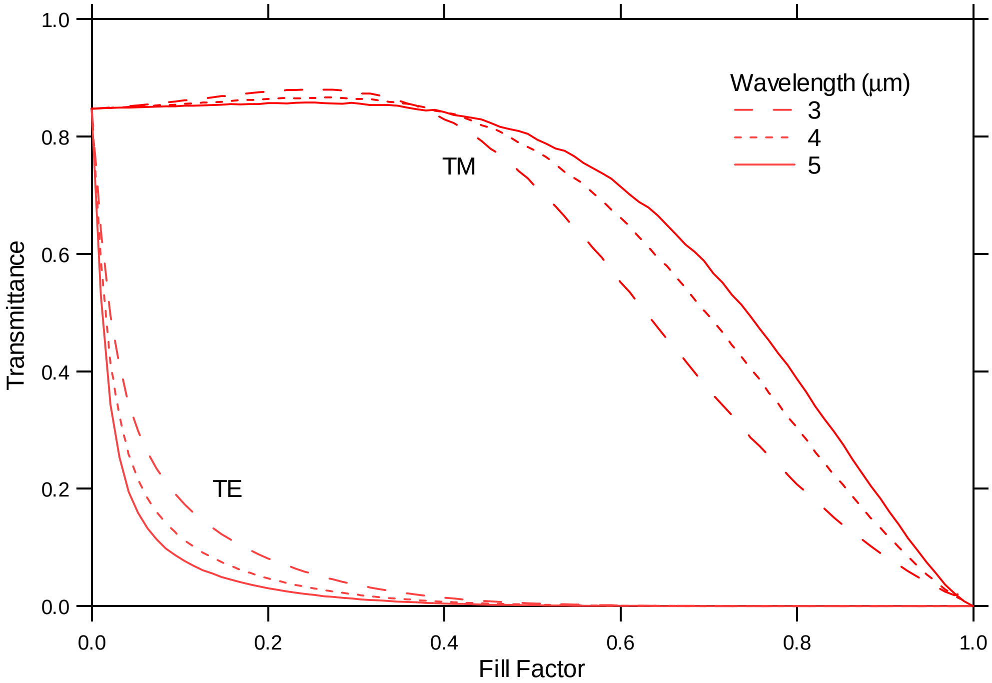

(b)

Figure 6.2 (a) Extinction ratio and (b) transmittance as a function of Mo grating fill factor.

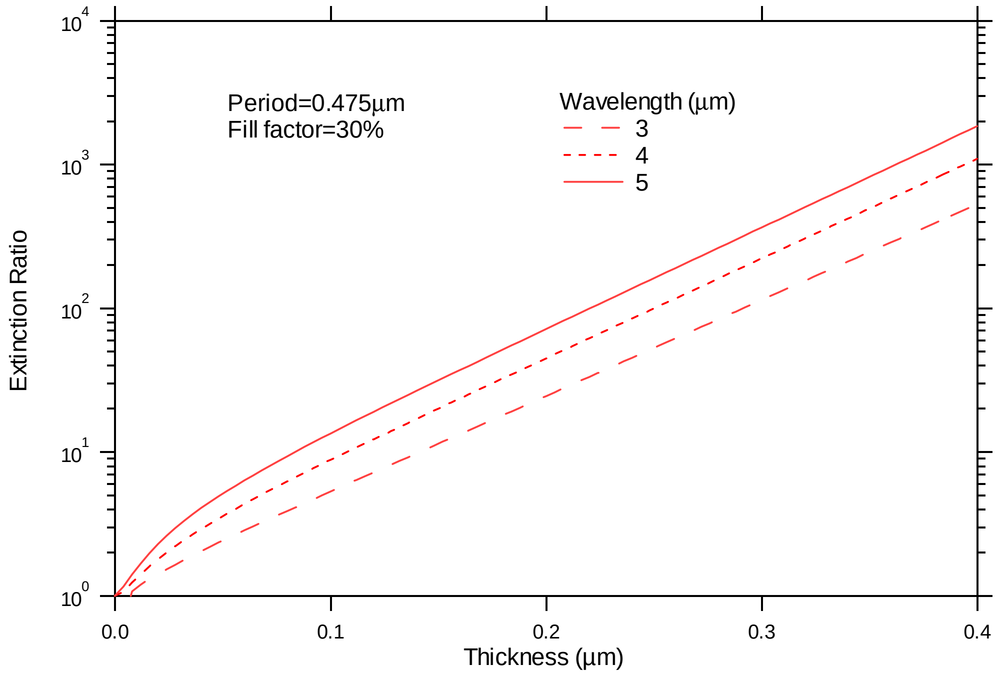

(a)

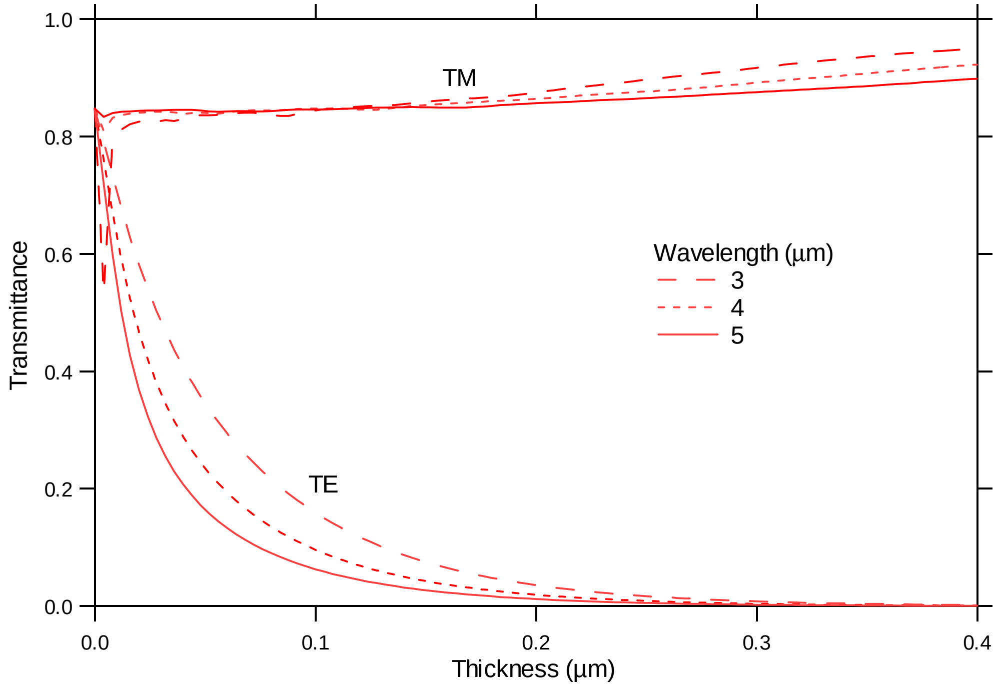

(b)

Figure 6.3 (a) Extinction ratio and (b) transmittance as a function of Mo grating thickness.

6.1.1.4 Low Index Insertion Layer Simulations: Thickness

The next set of simulation results illustrates the effect of inserting a low index layer between the Mo and Si substrate (which in our case will be needed to planarize the surface relief of the form birefringent Si wave plate). Our results show that the use of a low index layer can dramatically increase the extinction ratio and the transmission of the TM mode for the right planarizing layer thickness. At worst, the ER stays the same value. The transmission however can change to a significantly higher or lower value compared to the case with no planarizing layer. The planarizing layer thickness thus plays an important role in the performance of the polarizer.

Figure 6.4(a) shows the oscillating behavior of the ER as a function of the planarizing layer thickness. The ER behavior is periodic with thickness, and the period is, as expected, $\lambda/2n$. The peak value of the ER quadruples that of the Mo grating alone (i.e., when SU-8 thickness is 0). Figure 6.4(b) shows the transmission behavior. The TM and TE transmittance values can be markedly reduced or increased from the no planarizing layer case. Their ratio (T_{TM}/T_{TE}), defined as the ER, is an oscillating function with a maximum occurring when T_{TM} is high and T_{TE} is low. A thickness of 1.5 µm maximizes the transmission (~99%) and still yields a high ER of 700 for λ=4 µm. The ER will vary with wavelength; therefore for broadband applications, a thickness value must be chosen such that a high ER results throughout the desired range.

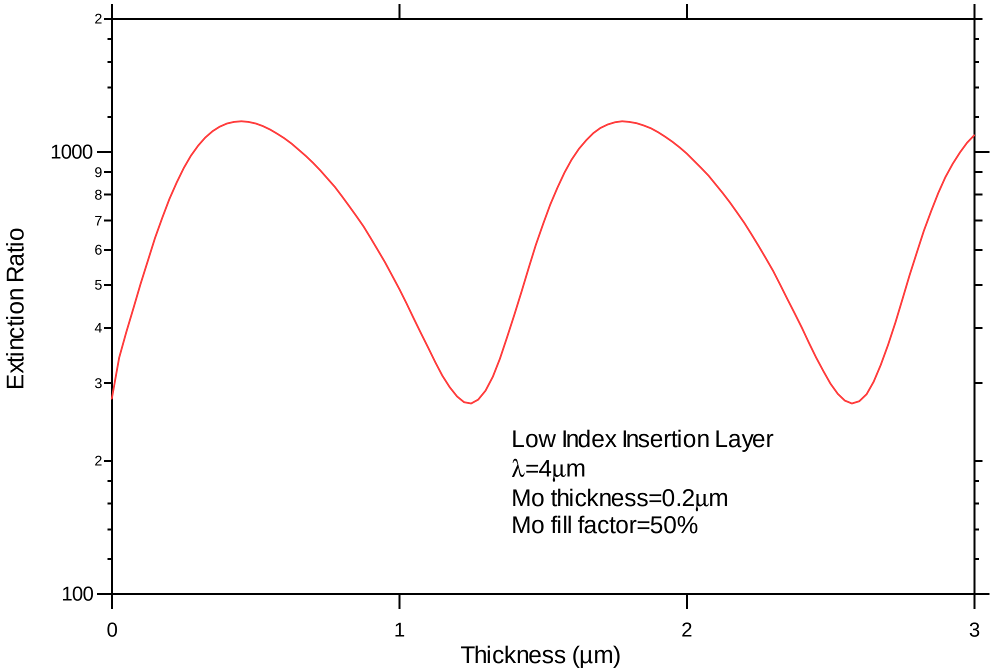

(a)

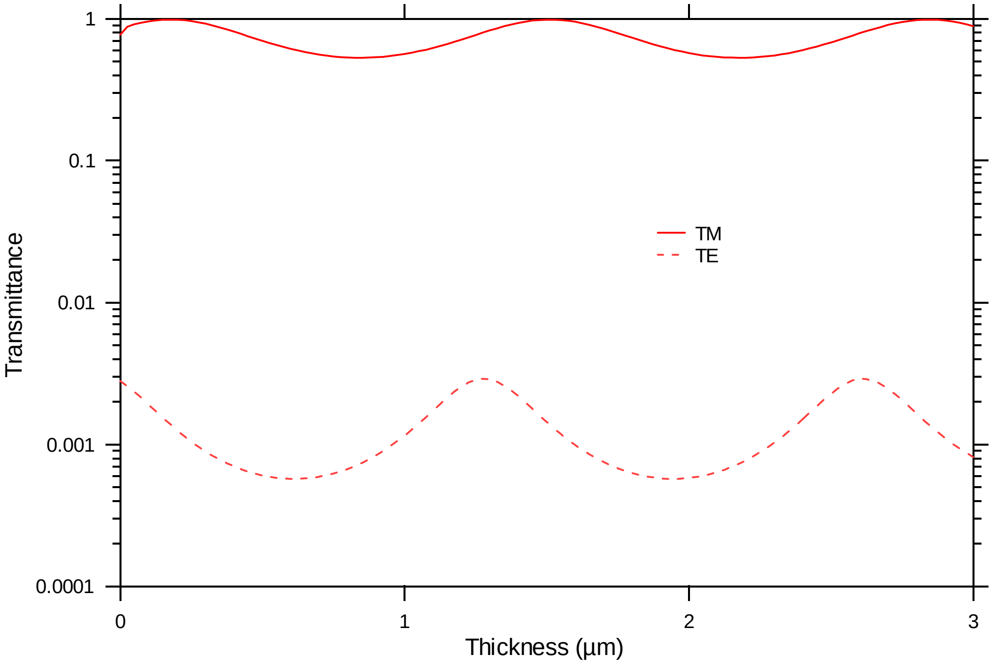

(b)

Figure 6.4 (a) Extinction ratio and (b) transmittance as a function of planarizing layer thickness.

6.1.2 Polarizer I: Fabrication

In this section, we describe the fabrication process of Polarizer I which consists of a Mo and Cr wire grids on silicon substrates. Fabrication of Polarizer I can be divided into four steps: 1) thin film deposition of metal layer 2) patterning of phtoresist using interference of lithography system 3) lift-off process to create an etch mask and 4) RIE of metal layer. These steps are described in the following sections.

6.1.2.1 Thin Film Deposition

We used p-type <100>75 mm in diameter Silicon substrates with a resistivity of 1-20 ohm-cm. A thin etch stop layer of SiO_2, 100 nm thick, is deposited on the substrate by RF sputter deposition. The parameters are 200 W power, 5 mTorr chamber pressure flow and 714 seconds of deposition time. A 160 nm layer of Mo is next deposited over the SiO_2 layer by DC sputtering. The parameters are 100 W power, 10 mTorr chamber pressure, 70 sccm of Ar flow, and 502 seconds of deposition time.

6.1.2.2 Photoresist Patterning

A wire grid polarizer having a 0.5 μm grid period can be suitably patterned using an interference lithography system. The angle between the two interfering laser beams determines the periodicity of the sinusoidal intensity pattern. The biggest difficulty in the fabrication process occurs in the patterning stage which depends on various factors such as the stability of the laser source, alignment of optical components, vibration isolation, and uniformity of the photoresist coat. Typical exposure times last as long as 2 minutes; therefore, fringe stability is crucial.

Photoresist is patterned with the interference lithography system shown in Figure 6.5. The laser source is a HeCd unit that operates at 442 nm and has a 120 mW power output. The raw laser beam is divided into two beams by a beamsplitter and directed by mirrors towards the recording plane. The raw beams are each spatially filtered, then expanded with a 20x microscope objective, and allowed to interfere at the exposure location approximately 1 meter from the spatial filters. The half-wave plate is used to equalize the beam intensities of the two arms. The period of the sinusoidal intensity pattern is given by the equation:

$$\Lambda = \lambda / 2\sin\theta_{1/2}, \tag{6.1}$$

in which $\theta_{1/2}$ is half the angle formed between the two laser beams. Our setup had a half angle of $\theta_{1/2}$=26.2° which results in a period of 0.5 μm.

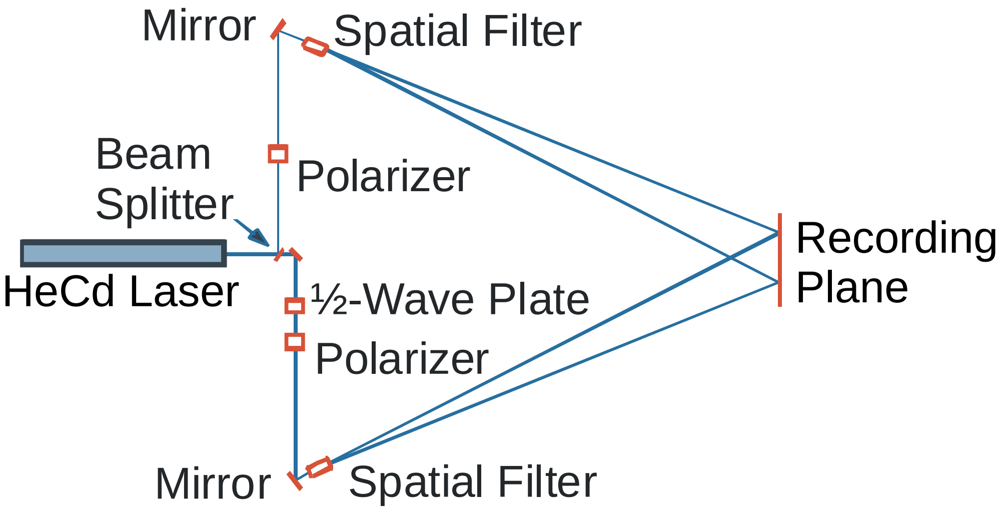

Figure 6.5 Diagram of interference lithography setup.

A 220 nm ARC layer is spun on top of the Mo layer prior to the photoresist layer and baked on a hotplate at 152°C for 1 minute. The use of a bottom-layer anti-reflection coating (ARC XL-20 from Brewer Science) on top of the highly reflective Mo layer is necessary for minimizing standing waves due to reflection from the Mo surface. A 0.5 μm thick positive photoresist, Shipley 1805, is spin-coated above the ARC layer and soft-baked at 115°C for 1 minute. The resist-coated wafer is exposed in the interference lithography system for an energy dose of 37.5 mJ/cm^2 (which is 100 seconds in exposure time). A 1 minute development time in the Microposit 352 developer removes the exposed regions on the resist and results in the 0.5 micron grating pattern. Typical results are shown in Figure 6.6.

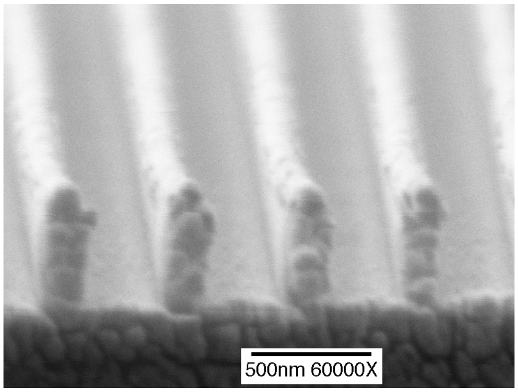

Figure 6.6 An SEM cross-sectional image of a photoresist grating patterned by interference lithography followed by an ARC etch to reveal the metal layer.

6.1.2.3 Lift-off Method

Pattern transfer of the photoresist grating pattern to the Mo layer could not be done directly by RIE because the resist is etched much faster than Mo and therefore could not act as the etch mask. We create a Cr etch mask directly from the photoresist pattern using the lift-off procedure described earlier in Section 5.2 of the QWP fabrication. Cr etches minimally in fluorine-based RIE. This lift-off procedure (see Figure 5.6) is described below.

The photoresist grating pattern is transferred to the ARC layer by a suitable polyimide etch (see Section 5.2.2) to reveal the Mo layer. A 25 nm layer of Cr is then thermally evaporated on the grating pattern. The wafer is then immersed in hot (165°F) photoresist stripper, Microposit 1165 Remover with ultrasonic assistance. The Cr deposited on the photoresist is lifted off while the Cr deposited on the Mo layer remains, thereby creating a Cr grating etch mask.

6.1.2.4 RIE

The resulting Cr etch mask is then used to pattern the Mo in the RIE. There are two stages in the etch. Initially, pure SF_6 gas is used to etch the Mo layer until about the final 5% of this layer remains. Another etch that adds Ar gas is then used to break through into the SiO_2 layer. The reduction of F atoms minimized the undercutting which was noticeable with the first etch. The parameters for the etches are

1) SF_6: 40 sccm gas flow rate, 15 mTorr chamber pressure, 100 W power, and 5.5 minute etch time;

2) SF_6/Ar: 30/10 sccm gas flow rates, 15 mTorr chamber pressure, 400 W power, and 30 seconds etch time.

An etched wire grid polarizer sample is shown in Figure 6.7. The resultant polarizer is a two wire grid. The Cr layer has a curvature resulting from the Cr deposition over the photoresist grating profile. The etched Mo layer is undercut due to the fluorine etch. The breakthrough etch required using high power (400 W) and Ar gas to improve anisotropic etching by emphasizing the physical sputtering aspect of the etch process. There is a presence of SiO_2 and SU-8 sputtered on the sidewalls of the Mo grating.

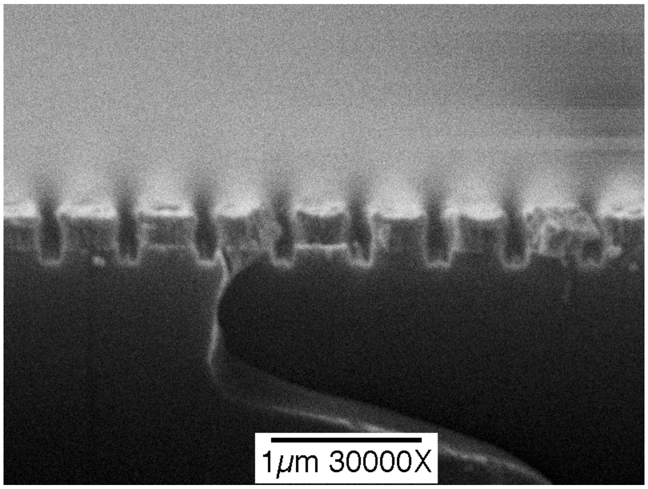

Figure 6.7 An SEM cross-sectional image of a Polarizer I sample.

6.1.3 Polarizer I: Performance

The performance of a Polarizer I sample in the desired wavelength range of 3.5 to 5 μm was measured with a FTIR spectrometer (FTS-60A from BioRad). The incident linearly polarized light was generated by a commercially available wire grid polarizer from Graseby/Specac. This polarizer has an extinction ratio of 107 and 273 at λ=3 μm and λ=7 μm, respectively, and linear interpolation was used for the ER within that range. The extinction ratio, ER, of a polarizer is defined as the ratio of its principal transmittances, the TM and TE modes. We differentiate this with the ER obtained from measurement of two polarizers that are in parallel and crossed orientations. Because of the finite ER of the generating polarizer, the ratio of the measured transmittances for the parallel orientation of the polarizers and the crossed orientation of the polarizers does not measure the ER of the sample. The process of extracting the ER of the sample from this measurement was discussed in Section 4.3.2.

This wire grid polarizer was fabricated on silicon substrate with no anti-reflection (AR) coating on the back side of the substrate. Therefore, a Fresnel reflection loss of 30% occurrs at that silicon/air interface which lowers the throughput of the sample. The final device will have an AR-coating to increase the throughput. The layer parameters used in the following simulations are given in Table 6.1.

Figure 6.8(a) shows the transmission of the TM and TE polarizations as a function wavelength through the sample. The RCWA simulation results for the TM transmission are in excellent agreement with the measurement. The measured TE transmission is larger than the predicted value and the difference can be partly attributed to defects in the wire grid where some regions are missing gratings and therefore allow either polarization modes to pass through.

Figure 6.8(b) shows the ER as a function of wavelength. The ER measured between both polarizers, sample and input generator, is measured to be within 30 to 35. Extracting the ER of the sample alone, we obtain values within 40 to 42.

Table 6.1 RCWA parameters for Polarizer I sample.

Layer	Thickness (μm)	Fill Factor
Air	Ambient	100%
Cr	0.025	60%
Mo	0.16	50%
SiO_2	0.1	100%
Si	Ambient	100%

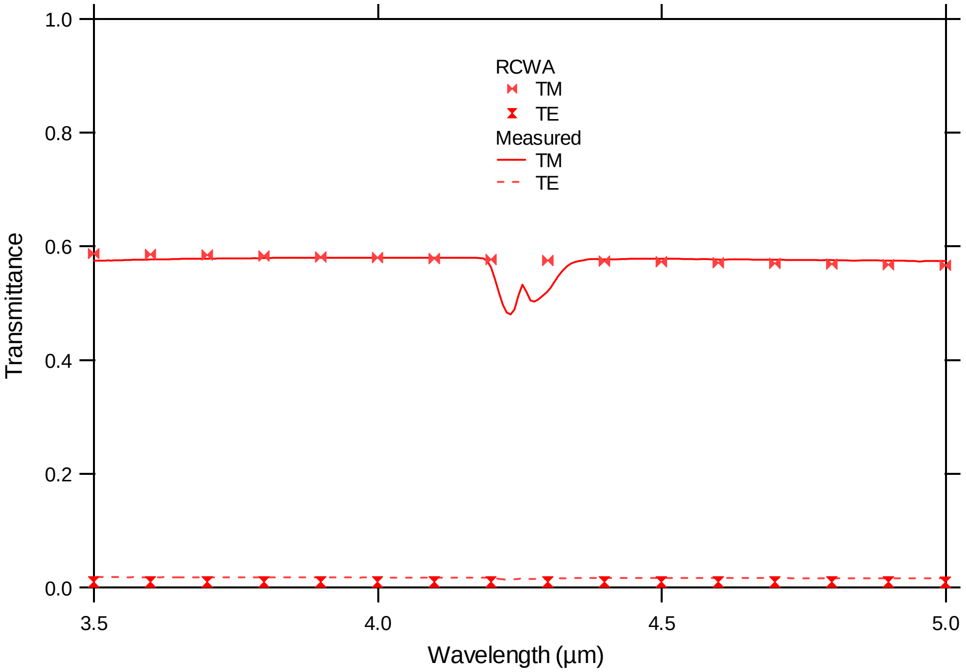

(a)

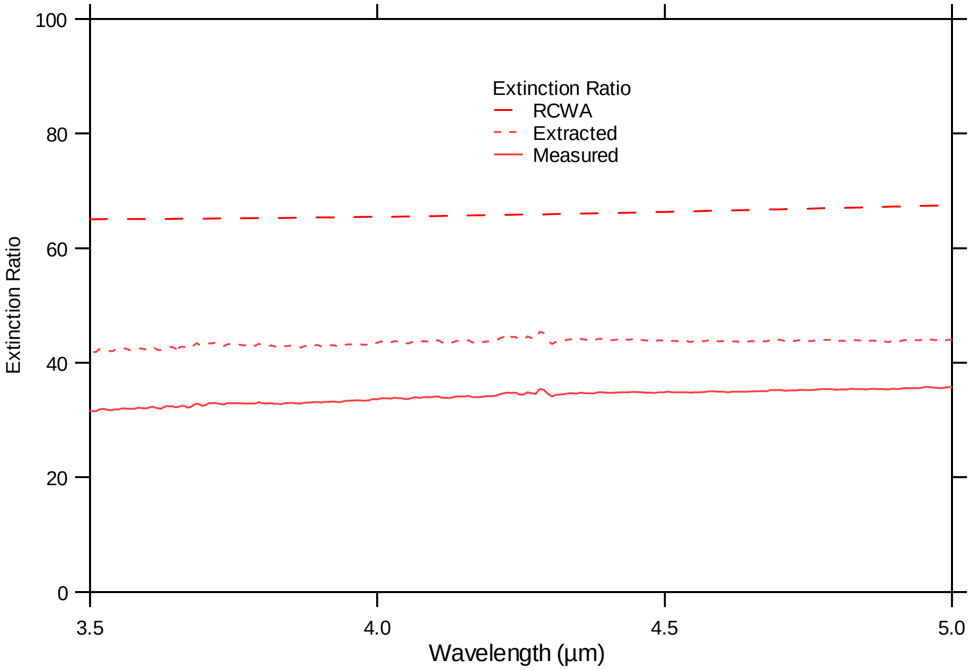

(b)

Figure 6.8 (a) Transmittance and (b) extinction ratio of a Polarizer I sample comparing the results from measurement and RCWA simulations.

6.2 Wire Grid Polarizer II

We investigate an alternative method of fabricating the wire grid polarizer by contact printing. The process of patterning 1 micron period photoresist gratings over a silicon substrate has already been developed with the QWP fabrication and therefore not a difficult transition to pattern such gratings over a metal layer. The use of a contact aligner offered several advantages as well as disadvantages compared to interference lithography. The contact mask aligner requires very little setup time as opposed to interference lithography which requires careful alignment of components and equalization of beam intensities between the two arms. Contact printing exposure times are also comparably shorter which leads to better repeatability. Long exposure times involved with interference lithography makes photoresist patterning susceptible to laser power instability, beam wandering and vibration in the testing apparatus.

The disadvantage of using contact printing is the necessity of providing a very flat surface for the photomask to make uniform contact across the grating region. The design also requires a thicker wire grid layer to compensate for the reduced ER performance due to the larger 1 μm grid period. The larger period however can accommodate the lift-off process of a thicker Cr layer. In this subsection, we investigate the design, fabrication and performance of this polarizer.

6.2.1 Polarizer II: Design

The period of the Polarizer II design is chosen as 1 micron. We investigate the performance of this polarizer in simulations varying the thickness of the Cr layer. We keep the thickness of Mo the same as Polarizer I. We can therefore determine what thickness of Cr should be added so as to compensate for using a larger grating period and achieve a polarizer performance comparable to the polarizer with a 0.5 μm period.

We characterize the dependence of the ER as a function of Cr layer thickness. We look at the case of a 2-layer polarizer consisting of a 160 nm Mo layer and a variable Cr layer thickness (see inset in Figure 6.9). The fill factor for both metals is 50%. A 100 nm SiO_2 layer is deposited over the silicon substrate to act as an etch stop. Figure 6.9 shows a plot of the ER as a function of the Cr thickness.

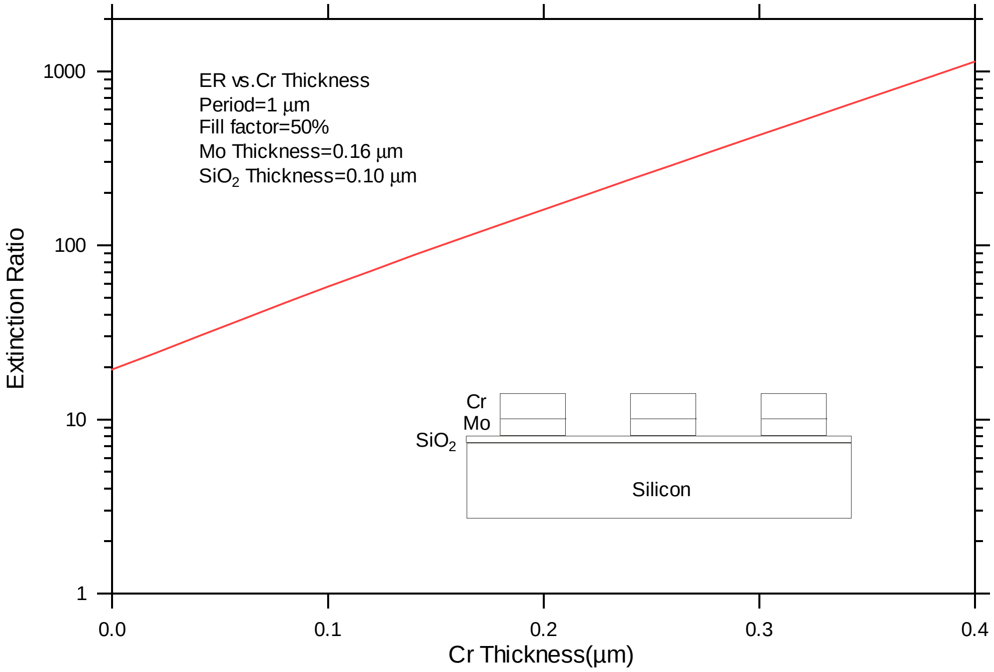

Figure 6.9 Extinction ratio as a function of Cr grating thickness for a 2-layer wire grid polarizer.

The ER of the wire grid polarizer increases as the Cr thickness increases. In the lift-off process used during the QWP fabrication to create an etch mask for silicon, a Cr layer greater than 200 nm was deposited. Using the same process to fabricate such a Cr grating layer over the Mo grating layer would produce a polarizer with an ER value greater than 100.

6.2.2 Polarizer II: Fabrication

A wire grid polarizer having a 1.0 μm grid period can be patterned by contact lithography. The fabrication process is a combination of the patterning process of the 1 μm period form birefringent QWP in Section 5.2.2 and the Mo etching process of Polarizer I in Section 6.1.2.4. A brief description is given below.

The 100 nm layer of SiO_2 and 160 nm layer of Mo are sucessively deposited on the silicon substrate by sputter deposition as was done with Polarizer I. A 220 nm ARC layer is applied over the Mo layer mainly to serve as an adhesion layer for photoresist. The Shipley 1805 photoresist is then applied over the ARC layer and exposure was accomplished with the contact mask aligner. Exposure time is 4 seconds. The lift-off procedure is used to generate a Cr grating from the photoresist grating pattern. In the Polarizer I fabrication, the thin (25 nm) Cr grating serves mainly as an etch mask for the Mo layer. In this Polarizer II fabrication, the Cr grating is 220 nm and serves the dual purpose of an etch mask and an additional polarizer layer. The Cr wire grid is then used as an etch mask to pattern the Mo layer by RIE using the same etch parameters as the Polarizer I process.

An SEM cross section of an etched wire grid Polarizer II sample is shown in Figure 6.10. The Cr grating having thickness of 220 nm has a large fill factor (65% to 72%). The underlying Mo grating was undercut during the etch because the etch time was too long. The etch penetrated through the SiO2 etch stop layer and into the silicon substrate. To improve the fabrication, the exposure time should be reduced (by ~25%) to decrease the fill factor so that transmission is higher. The etch time also should be reduced to minimize undercutting of the Mo grating.

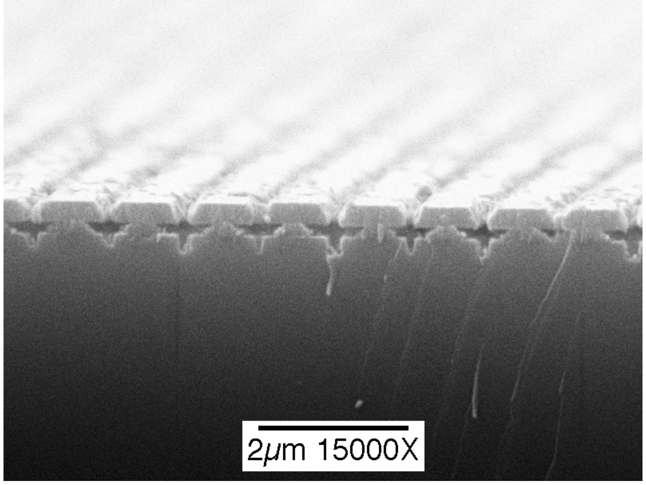

Figure 6.10 An SEM cross-sectional image of a Polarizer II sample.

6.2.3 Polarizer II: Performance

The performance of a Polarizer II sample in the desired wavelength range of 3.5 to 5 μm was measured with the FTIR spectrometer. The incident linearly polarized light was generated by another commercially available wire grid polarizer from Molectron Detector Inc. which has an extinction ratio of 74 and 105 at $\lambda = 3.5$ and 5 μm, respectively. This Polarizer II sample is also without an AR-coating and suffers from Fresnel reflection loss. The layer parameters used in the following simulations are given in Table 6.2.

Figure 6.11(a) shows the transmission of TM and TE polarizations through the sample as a function wavelength. The measurement of the TM transmittance yielded values from 40% to 60% across the wavelength range and RCWA simulation results are in agreement. The measured TE transmission is again larger than the predicted value. The Polarizer II sample transmits 0.5% in comparison to an RCWA result of 0.2%. The difference may be due to the uncertainty in the true optical constant of the evaporated Cr. Because our optical constant was measured from sputtered Cr, it is possible that the higher energies involved in sputtering deposition in comparison with thermal evaporation can have an appreciable effect on the optical constant through the film morphology. Another reason may be the sensitivity of the measurement which involves very small signal amplitudes and possible linearity errors in the detector.

Figure 6.11(b) shows the ER as a function of wavelength. The ER measured between both polarizers, the Polarizer II sample and the polarizer generating the input, is measured to be within 65 to 105. Extracting the ER of the sample alone, we obtain values of approximately 250. The RCWA simulation results predict larger values of approximately 550. The calculation of the extinction ratio (T_{TM}/T_{TE}) is very sensitive to the small discrepancies in TE transmittance because it is in the denominator.

Table 6.2 RCWA parameters for Polarizer II sample.

Layer	Thickness (μm)	Fill Factor
Air	Ambient	100%
Cr	0.14	65%
Cr	0.08	72%
Mo	0.16	15%
SiO_2	0.11	100%
Si	Ambient	100%

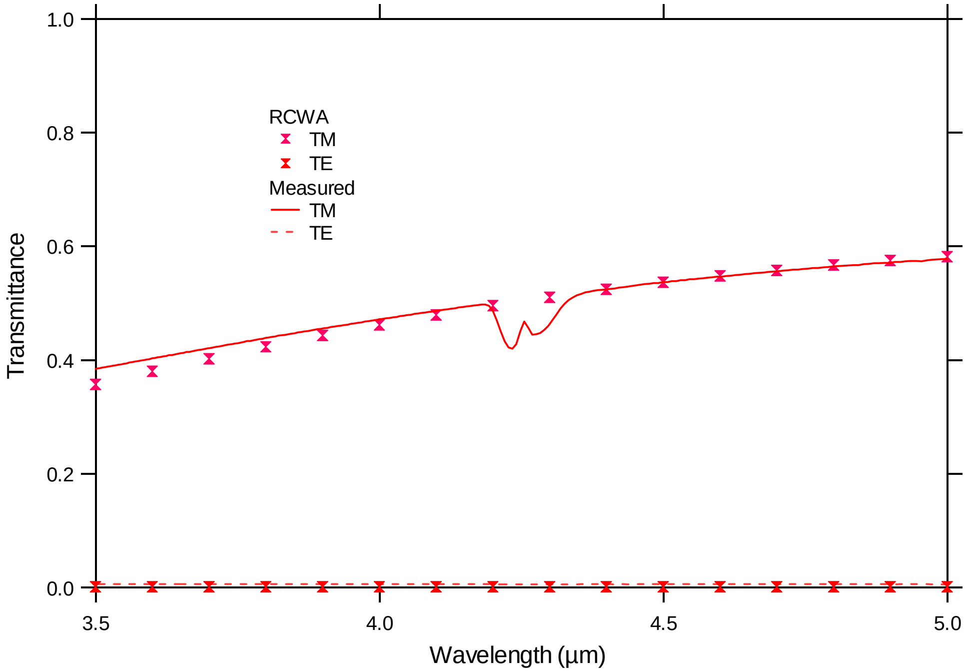

(a)

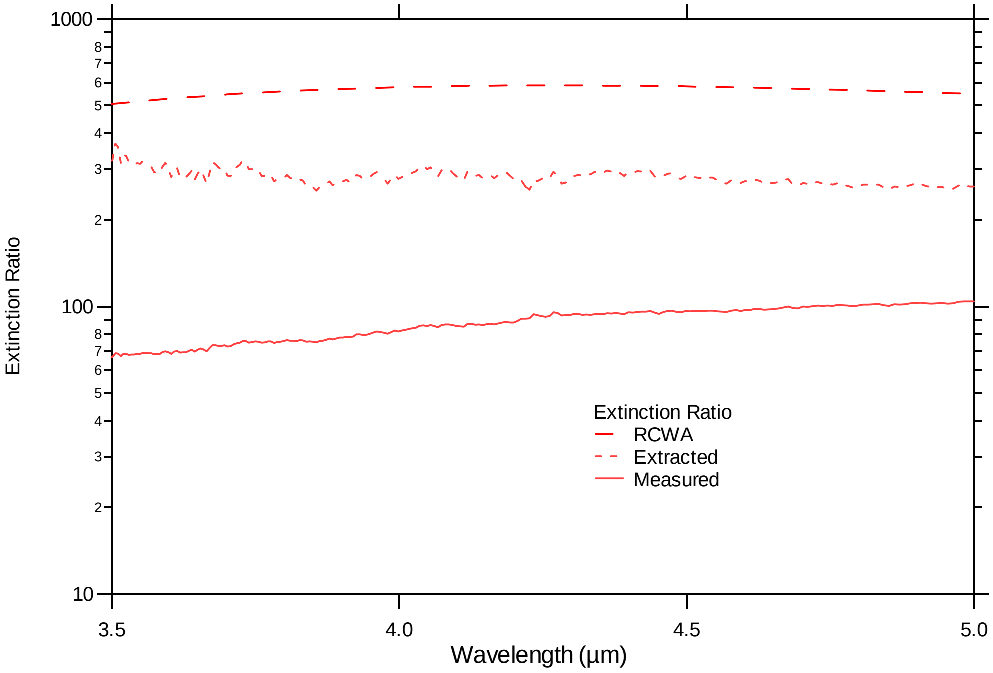

(b)

Figure 6.11 (a) Transmittance and (b) extinction ratio of the Polarizer II sample comparing the results from measurement and RCWA simulations.

6.3 Conclusion

In conclusion, we have presented two methods of fabricating wire grid polarizers for an application in imaging polarimetry. The first design, referred to as Polarizer I, was fabricated by the method of interference lithography and performed with an extinction ratio of 40. The TM transmittance was 60% for these samples which were not AR-coated. The 30% Fresnel reflection loss at the front surface of the substrate would be reduced with a broadband AR-coat which would increase the transmittance to approximately 75% to 80%. To improve the ER of polarizer I, the thickness of the Mo layer can be increased without changing the fabrication process that has been developed.

Another design, referred to as Polarizer II, was fabricated by contact lithography and had a high ER performance that was calculated to be approximately 250. Its transmission ranged from 38% to 56% across the 3.5 to 5 μm wavelength which is noticeably lower at the shorter wavelengths in comparison to Polarizer I. Again, the Fresnel reflection loss can be reduced with an AR-coating on the back surface of the substance, which would result in a transmission of 50% to 80%.

The ER and transmittance of both polarizers are satisfactorily high and adequate for our application in imaging polarimetry. The comparison between simulation and measured (extracted) results of TM transmittance through the polarizers are excellent, in which values up to 60% were measured. The TE transmittance ($=T_{TM}/ER$) also has reasonable agreement between simulation and (extracted) measurement. At $\lambda=5$ μm, Polarizer I transmits approximately 1.3% in comparison to a slightly lower RCWA result of 1.0%. The calculation of the extinction ratio (T_{TM}/T_{TE}) is very sensitive to the small discrepancies in TE transmittance because it is in the denominator, which is illustrated by the difference between the measured and RCWA simulation ER values. Discrepancies can be partly attributed to scattering from the rough texture of the grating profile (due to fabrication process) which may have a depolarizing effect. From the polarizer measurements, the predicted ER values can be twice as large as the measured values. In the design process, this factor can then be taken into consideration.

Chapter 7

CIRCULAR POLARIZERS USING STACKED SUBWAVELENGTH GRATINGS

An attractive option that has not previously been explored is to stack subwavelength grating components in a single structure to form a multi-functional integrated component. This integration provides the advantages of fabrication flexibility, package size reduction and structure stability. In this dissertation, we treat an application in imaging polarimetry in which linear and circular polarizer filters are used to determine the linear and circular polarization content of the incoming radiation. These measurements allow the polarization state to be completely specified in terms of the Stokes vector components. Our design to implement the circular polarization filter uses two polarization elements, a quarter-wave plate and a polarizer, whose axes are rotated 45° apart. As demonstrated in Chapters 5 and 6, subwavelength gratings are suitable for realizing such elements. In this chapter, we discuss the integration of the form birefringent quarter-wave plate and wire grid polarizer to implement another functional component, a circular polarizer. We present the design, fabrication, and performance of stacked subwavelength gratings for use as a circular polarization filter for the 3.5 to 5 μm wavelength range. The fabrication process for integrating the two SWG structures can accommodate the fabrication of relatively large area (~1 cm^2) uniform filters, as well as a 512 x 512 array of small aperture (15 μm x 15 μm) filters (corresponding to the focal plane array pixels of the imaging polarimeter). We discuss the performance of the two stack designs initially in the large aperture case and look at the performance of the circular polarizers as a pixel array of small apertures in Chapter 8.

7.1 Design of Circular Polarizers

Two circular polarizer designs were investigated. The first design, Stack I, consists of the form birefringent quarter-wave plate and Polarizer I, the 0.5 μm period wire grid polarizer. Stack II consists of the form birefringent quarter-wave plate and Polarizer II, the 1.0 μm period wire grid polarizer. The QWP and polarizer are specifically oriented such that the circular polarization filter passes right circularly polarized (RCP) light and blocks left circularly polarized (LCP) light. In the following section, the Jones Matrix formulation is used to analyze the performance of the circular polarization filter by treating the stack as cascaded components.

7.1.1 Jones Matrix Calculation

We are interested in fabricating a circular polarizer with a circular extinction ratio (defined as the ratio of RCP and LCP transmittances) of approximately 10 to 20. A Jones matrix calculation is used to determine the performance of the circular polarizer consisting of a QWP and a polarizer. We determine the performance loss due to non-ideal components and fabrication errors. The tolerance on fabrication errors can then be specified in order to meet the performance goal.

The Jones matrix for a non-ideal QWP and a non-ideal polarizer rotated 45° from one another is (see Section 4.3.1)

$$\begin{aligned} \mathrm{A} &= [Polarizer]\cdot R(+45^{\circ})\cdot[QWP] \\ &= \begin{bmatrix} \alpha & 0 \\ 0 & \beta \end{bmatrix} \frac{1}{\sqrt{2}} \begin{bmatrix} 1 & 1 \\ -1 & 1 \end{bmatrix} \begin{bmatrix} \varsigma\, e^{i\varphi_x} & 0 \\ 0 & \eta\, e^{i\varphi_y} \end{bmatrix}, \end{aligned} \tag{7.1}$$

in which α, β, ς and η are the field amplitudes, and φ_x and φ_y are the relative phases of the field along the x and y directions. The difference between the phases defines the retardance of the QWP, $\varphi = \varphi_x - \varphi_y$. Furthermore, we define the QWP retardance error, Δ, in the following equation: $\varphi = \frac{\pi}{2} + \Delta$. The circular extinction ratio, ER_c, of the stack is given by the transmittance ratio of right circularly polarized (RCP) illumination and left circularly polarized (LCP) illumination:

$$ER_C = \frac{T_{RCP}}{T_{LCP}} = \frac{\left|\underline{\underline{A}} \cdot \underline{J}_{RCP}\right|^2}{\left|\underline{\underline{A}} \cdot \underline{J}_{LCP}\right|^2} \tag{7.2}$$

with $\underline{J}_{\mathrm{RCP}} = \frac{1}{\sqrt{2}}\begin{bmatrix} 1 \\ -j \end{bmatrix}$ and $\underline{J}_{\mathrm{LCP}} = \frac{1}{\sqrt{2}}\begin{bmatrix} 1 \\ j \end{bmatrix}$.

Substituting Equation (7.1) into Equation (7.2), we obtain

$$ER_C = \frac{(\varsigma\alpha)^2 + (\alpha\eta)^2 + (\varsigma\beta)^2 + (\beta\eta)^2 + 2\varsigma\eta(\cos\Delta)(\alpha^2 - \beta^2)}{(\varsigma\alpha)^2 + (\alpha\eta)^2 + (\varsigma\beta)^2 + (\beta\eta)^2 - 2\varsigma\eta(\cos\Delta)(\alpha^2 - \beta^2)} \; . \tag{7.3}$$

As an example, consider a non-ideal polarizer that has a linear extinction ratio of 40 and 80% transmission ($\approx\alpha^2$). The circular extinction ratio can be plotted as a function of the QWP retardance error Δ and QWP transmittance ratio which we define as $\gamma \equiv \eta^2/\zeta^2$. In Figure 7.1, the circular ER is plotted as a function of Δ for various cases of γ as it deviates from the ideal value of 1 to 0.7. From the curves, a circular extinction ratio of approximately 20 can be achieved if the QWP tolerance on the retardance error is within $\Delta = \pm 0.1\pi$ and tolerance on the transmittance ratio is $\gamma > 0.8$.

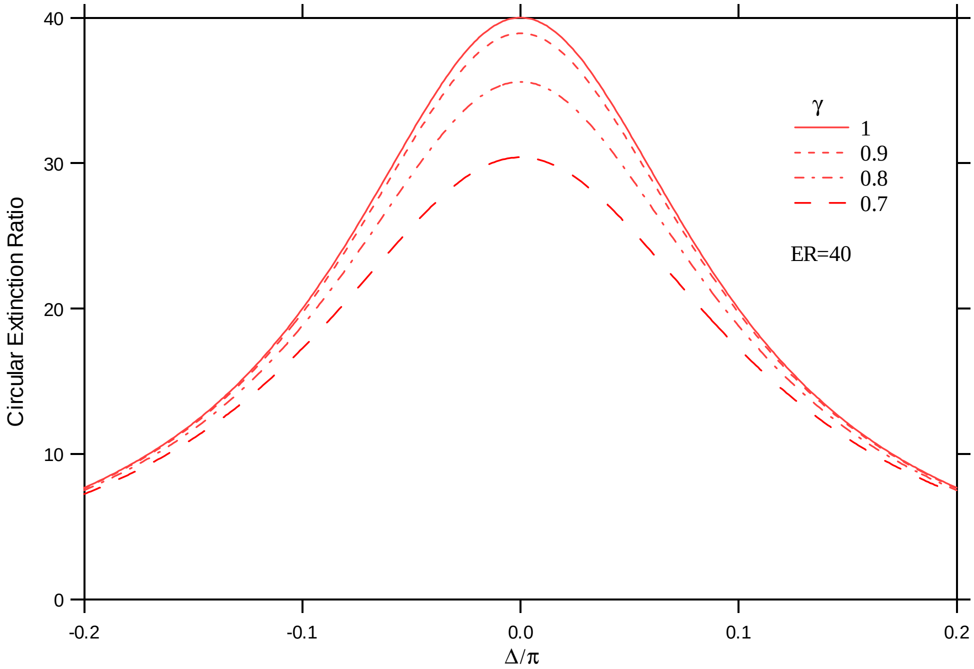

Figure 7.1 Circular extinction ratio of the stacked SWG's as a function of Δ for the cases of γ=0.7, 0.8, 0.9 and 1 and polarizer ER=40.

7.2 Circular Polarizer: Stack I

The first circular polarizer investigated is the Stack I design which consists of the 0.5 micron period wire grid polarizer (Polarizer I) stacked above a planarized, form birefringent QWP. The linear extinction ratio achieved by a representative Polarizer I was approximately 40 (discussed in Chapter 6). A representative form birefringent QWP (described in Chapter 5) performed with phase retardance within 0.4 to 0.6π. Both SWG components are within the fabrication tolerances specified in the previous section.

7.2.1 Fabrication of Stack I

We discuss the fabrication of Stack I consisting of the form birefringent QWP and Polarizer I. Since the fabrication of the individual components has been extensively described in Sections 5.2.2 and 6.1.2, a detailed discussion is given only to complications arising from the integration process and to modifications from the previous procedures.

7.2.1.1 QWP Fabrication

The underlying SWG structure in the stack is the form birefringent QWP which is fabricated directly on the silicon substrate surface. To accommodate the stacking of another SWG layer above this surface relief structure, this silicon grating required a planarization layer. The QWP design is a silicon grating having the parameters of a 1 μm period, 2.1 μm thickness and 66% fill factor and planarized with an SU-8 layer. There is no modification in the patterning and etching process of the QWP as described in Section 5.2.2.

7.2.1.2 Planarization

The planarization layer was critical to the success of integrating the QWP and the wire grid polarizer. The layer had to sufficiently planarize the QWP grating structure and also be compatible with the subsequent process to fabricate the polarizer above the QWP. The QWP silicon gratings have been succesfully planarized using two different materials, a polyimide-type, deep UV positive resist (PMGI) and an epoxy-based, near UV negative resist (SU-8). Both are applied by spin-coating and require a subsequent baking step to achieve the planarization. The resulting layer further acts as a protective dielectric cover. The PMGI material however was incompatible with the current polarizer fabrication process because it reacts with the photoresist stripper used in the lift-off process. However, SU-8 has good resistance to acetone and other photoresist strippers such as Microposit 1165 Remover and was chosen as the current planarizing material for the stack. The details of the procedure for processing the SU-8 (consisting of spin-coat, flood exposure, and bake) are given in Section 5.2.3.

7.2.1.3 Polarizer I Fabrication over the QWP

The success of the polarizer fabrication above an SU-8 planarized grating relies on achieving a very uniform SU-8 surface after planarization. Air bubbles, particulates and other surface defects can sometimes appear and the metal layer that is deposited on this planarization layer will assume this uneven topography. During the exposure, unwanted scattering of light results in non-uniform patterning of the photoresist. The surface defects arising from the use of a planarization layer lowered the yield of the process in comparison to the polarizer-only fabrication of Chapter 6.

The fabrication of Polarizer I is described fully in Section 6.1.2 and an outline of the steps is presented below. A thin layer of SiO_2 (100 nm) is deposited over the SU-8 prior to the thin film deposition of the metal. This SiO_2 coat will serve as the etch stop during the plasma etch of the metal (the wire grid polarizer). It also serves as a good adhesion layer (a compact surface due to high-energy sputter deposition) for the metal and provides another layer above the SU-8 to withstand chemicals used in the process. A 160 nm layer of Mo is DC sputtered onto the SiO_2 above the planarized QWP. An ARC layer is spin-coated on the Mo and then the 1805 resist is spin-coated above that. The photoresist is patterned with the interference lithography system. A lift-off procedure is used to create a Cr etch mask and involves the evaporation of a 25 nm layer Cr on the grating pattern. The resulting Cr mask is then used for the etching of the Mo layer with the RIE system.

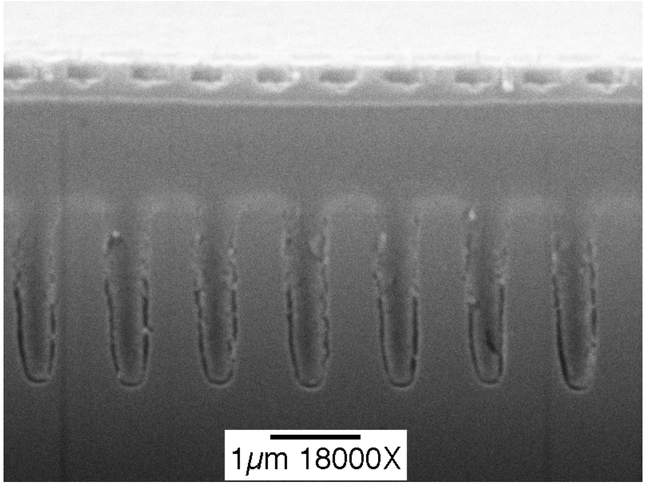

Figure 7.2 An SEM cross-sectional image of a Stack I circular polarizer.

An SEM cross section of the stack is shown in Figure 7.2. This image was taken along the direction of the QWP grating ridges, and the wire grid polarizer gratings are shown oriented at an angle of 45°. The QWP is approximately 1.93 μm and sufficiently planarized by a 1.3 μm SU-8 layer. The 100 nm SiO_2 layer prevented the etch from penetrating into the SU-8 layer. The wire grid polarizer consists of 160 nm of etched Mo and 25 nm of evaporated Cr gratings.

7.2.2 Performance of Stack I

The right circular polarizer fabricated above will convert unpolarized light into right circularly polarized light if the illumination is incident from the linear polarizer side of the device. However, for the imaging polarimetry application, we will use it as a circular polarization filter that passes RCP light and blocks LCP light when the illumination is incident first on the QWP side of the device. (The two functionalities are interchanged by flipping the wafer 180° such that the order of the QWP and polarizer are reversed.) We characterize the performance of Stack I as a circular polarization filter by measuring the transmission of incident LCP and RCP radiation through the sample. An FTIR spectrometer (FTS-60A from BioRad) and an FTIR spectropolarimeter were used to obtain measurements across the desired wavelength range of 3.5 to 5 μm. The incident circular polarization modes to test the sample were generated by bulk QWP and polarizer components with known characteristics. The Specac wire grid polarizer has an extinction ratio of 107 and 273 at λ=3 μm and λ=7 μm, respectively, and linear interpolation was used for the ER within that range. The QWP is a form birefringent QWP fabricated in our lab and measured with the FTIR spectropolarimeter. The phase retardance and transmittances (TM and TE) of this QWP are shown in Figure 7.3.

Nominal RCP and LCP incident polarization states were generated by rotating the QWP fast axis +45° and -45° from the polarizer azimuthal axis, as shown in Figure 7.4. The actual elliptical states were calculated using the Jones Matrix calculus presented in Section 4.3.4. The input polarization states used in the approximate and rigorous analysis of the SWG stack are given in Table 7.1.

In our investigation, we discovered the surprising effect of using antireflection (AR) coating on the backside of the wafers to improve polarization performance of the samples. We typically use an AR-coating to increase the transmission of a device. In the case of stacked SWG structures, the transmission of the RCP light increased, but surprisingly the transmission of LCP light decreased. The result is an increase in extinction ratio and therefore improvement in both transmission and polarization performance of the circular polarizer.

In the following sections, we compare the performance of samples with and without AR-coating. A single layer SU-8 coating was initially used as an AR-coating (good only for a small wavelength range) to observe the performance improvement. A broadband AR-coating was also applied to samples to improve the transmission performance across the entire 3.5 to 5 μm wavelength range.

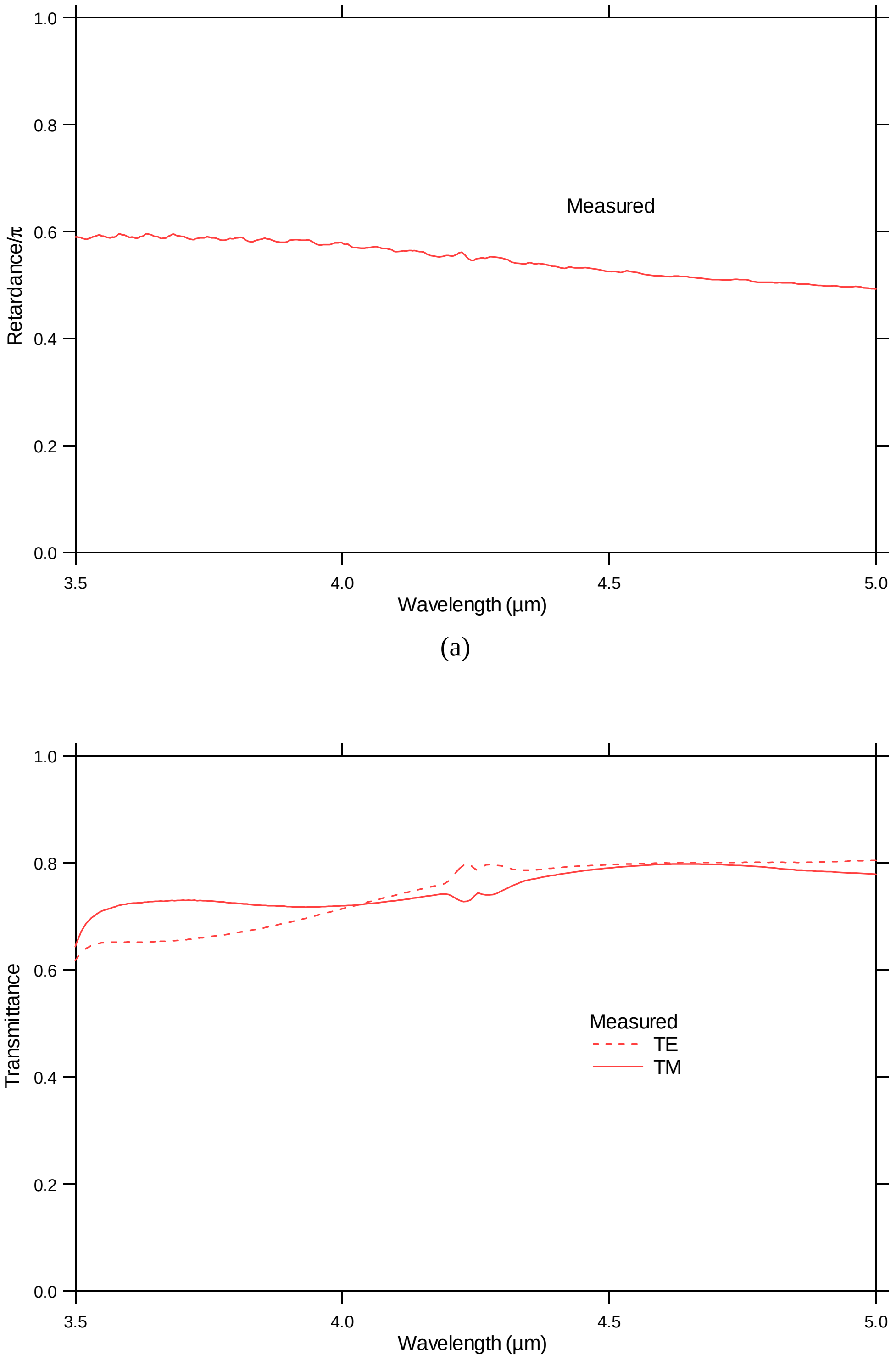

(a)

(b)

Figure 7.3 (a) Phase retardance and (b) transmittance measurements of the QWP which is used along with a polarizer to generate the incident circular polarization states.

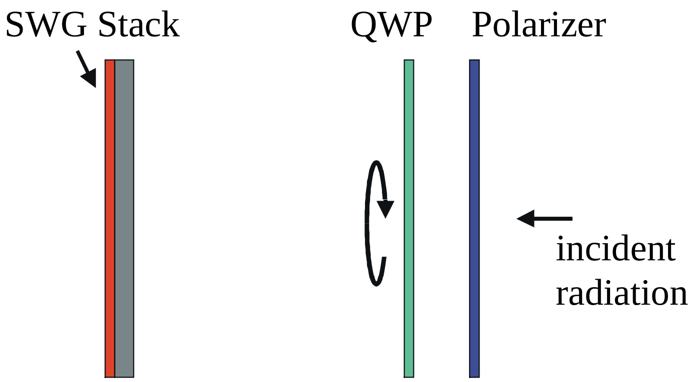

Figure 7.4 Configuration of the FTIR spectrometer testing of the SWG stack.

Table 7.1 Elliptical polarization input to simulations.

λ (μm)	**b/a**	**ψ_{RCP} (°)**	**b/a**	**ψ_{LCP} (°)**
3.5	0.72849	-31.2839	0.69496	-25.1113
3.75	0.7297	-31.6288	0.6992	-25.7572
4	0.74819	-26.9172	0.74531	-26.3945
4.25	0.78433	-20.5809	0.80217	-23.301
4.5	0.82711	-13.1068	0.84073	-14.4664
4.75	0.84666	-4.06823	0.86131	-4.54351
5	0.83516	2.42536	0.88234	3.50426

7.2.2.1 Stack I: No AR-Coating

We discuss initially the case of a Stack I circular polarizer (shown in Figure 7.2) with no AR-coating on the backside of the wafer. The layer parameters used in the Stack I simulations are given in Table 7.2.

Table 7.2 Layer parameters for Stack I circular polarizer.

Layer	**Thickness (μm)**	**Fill Factor**
Cr	0.025	70%
Mo	0.16	33%
SiO_2	0.1	100%
SU8	1.26	100%
QWP	1.21	53.4%
QWP	0.72	62.2%
Si	330	100%

Transmission measurements of RCP and LCP incident illumination, T_{RCP} and T_{LCP}, and the circular extinction ratio ($\equiv T_{RCP}/T_{LCP}$) as a function of wavelength are shown in Figure 7.5. The circular ER values of 3.5 to 5.5 across the desired wavelength range are unexpectedly low in comparison to the results obtained from the Jones Matrix simulations in Section 7.1.1 of a circular polarizer with comparable polarizer and QWP properties. Since these simulations do not take into account multi-layer interactions occuring within the SWG stack and within the silicon substrate, an analysis was performed using the rigorous method of SRG-RCWA to include the effect of multiple reflections occurring throughout the entire thickness of the wafer.

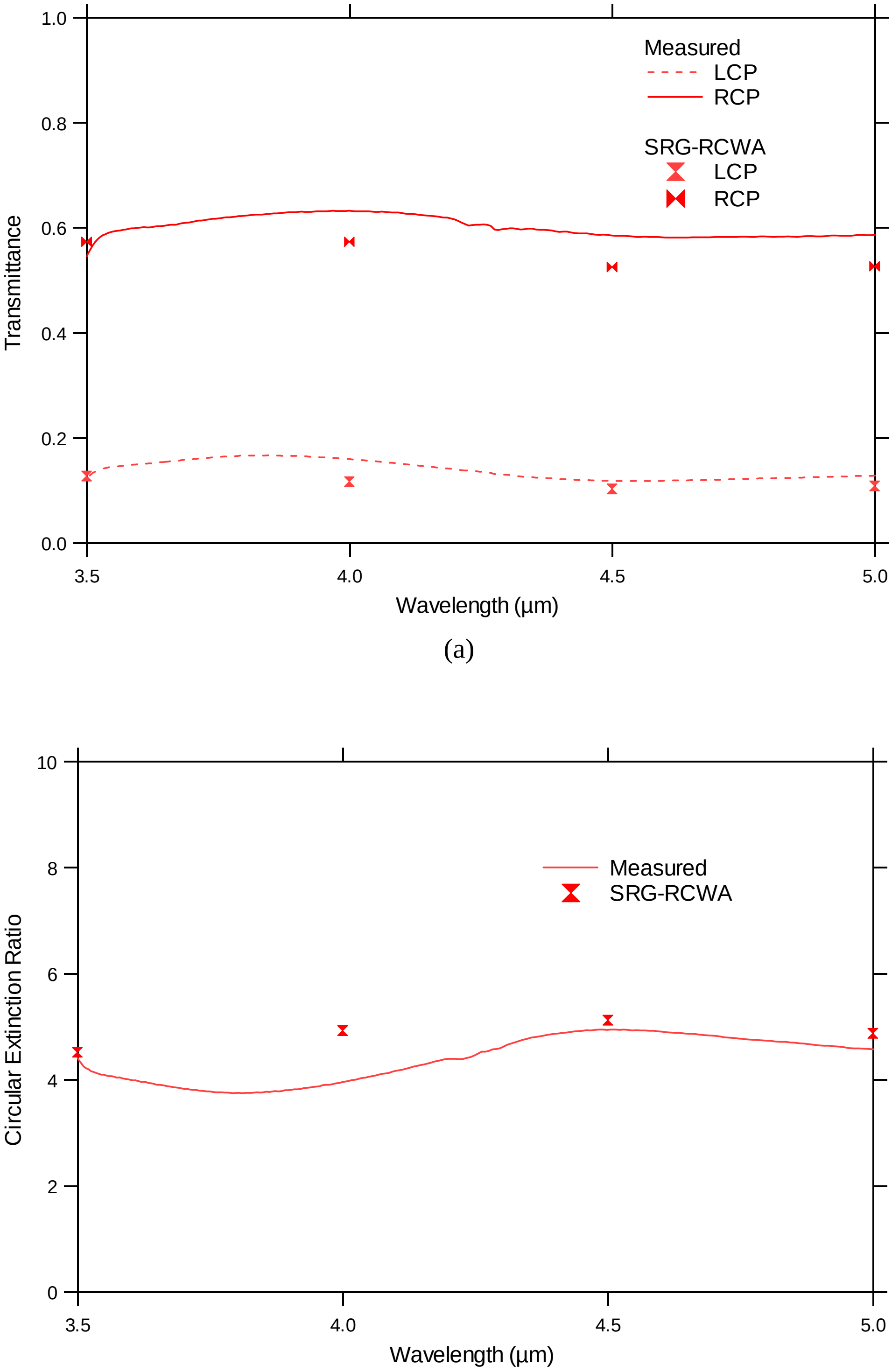

(a)

(b)

Figure 7.5 (a) Transmittances and (b) extinction ratio of Stack I sample without AR-coating comparing the results from measurement and SRG-RCWA simulations.

In the same figure, SRG-RCWA simulation results are plotted as a function of wavelength. Each SRG-RCWA simulation point is an average value within an interval of ±0.05 μm from the wavelength of interest due to the oscillatory behavior associated with the thick silicon substrate. There is agreement between measurement and simulation results for the RCP and LCP transmittances and consequently their ratio, the circular extinction ratio. The low circular ER values measured are therefore supported by results from simulations using rigorous analysis. We next examine the improvement due to the AR-coating of the samples.

7.2.2.2 Stack I: Single Layer AR-Coating

To determine the performance dependence on the AR-coating, a Stack I sample was AR-coated with a single layer of SU-8 on its backside. In order to spin-coat the SU-8 on the backside, the fragile SWG stack had to be protected with a dielectric cover, as shown in Figure 7.6.

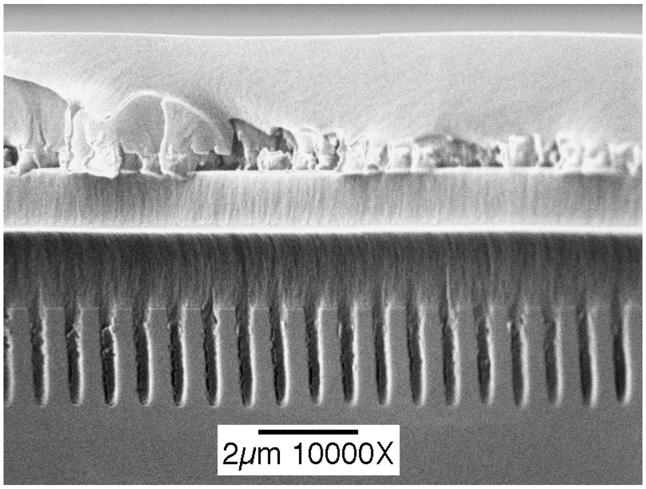

Figure 7.6 An SEM cross-sectional image of Stack I sample that has an SU-8 AR-coating in the backside (not shown).

The single layer of SU-8 applied on the backside acts as a good AR-coating for only a small wavelength range. For an SU-8 thickness of 2.46 μm, the theoretical transmission curve is maximized at the longer end of the 3.5 to 5μm wavelength range, as shown in Figure 7.7. The measured circular ER of the Stack I sample with a single layer SU-8 AR-coating is shown in Figure 7.8(a). There is a definite increase in the ER values, as much as 75%, at the longer wavelength region where the reflection is suppressed by the AR-coating. In the shorter wavelength region where the single layer AR-coating is ineffective, the circular ER is mainly unaffected.

The single layer AR coating of SU-8 is deficient in effective range and transmission (maximum of approximately 94%). We look at the improvement offered by a commercially available multi-layer, broadband AR coating in the next section.

7.2.2.3 Stack I: Broadband AR-Coating

A commercial broadband anti-reflection (BBAR) coating for the 3 to 5μm wavelength range was applied to the backsides of samples to suppress Fresnel reflections occurring at that interface. At this silicon-air interface, transmission values of 95% to 98.5% were achieved across the whole wavelength range. The same Stack I sample (no AR-coating) shown in Figure 7.2 received a BBAR-coating for direct comparison. The transmission of the RCP and LCP states before and after the BBAR-coat is shown in Figure 7.9(a). The RCP transmission increased as we expected because of the AR-coat (from 60% to 80%). There is however a surprising decrease in LCP transmission.

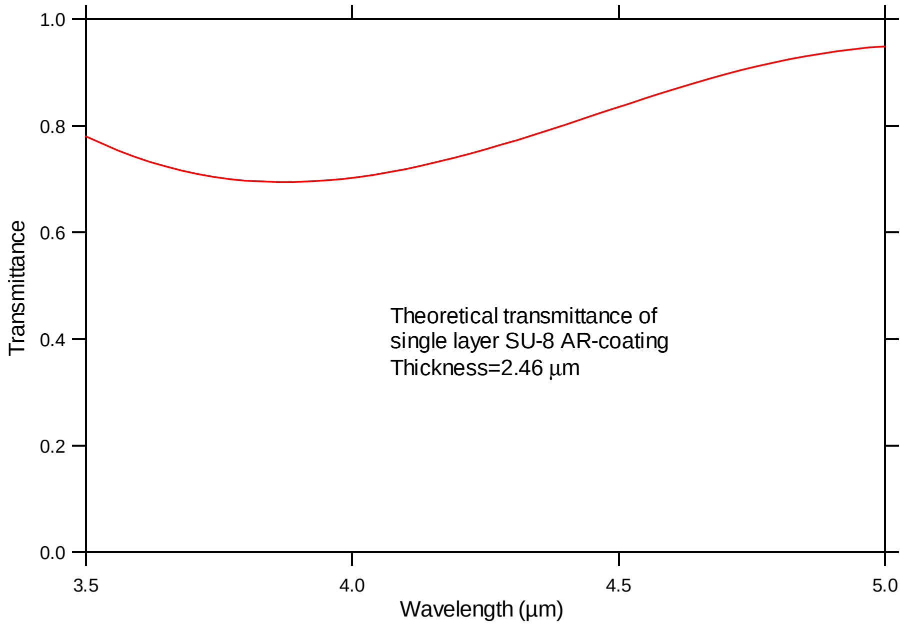

Figure 7.7 Theoretical transmittance of SU-8 AR-coat optimized for the longer wavelength region.

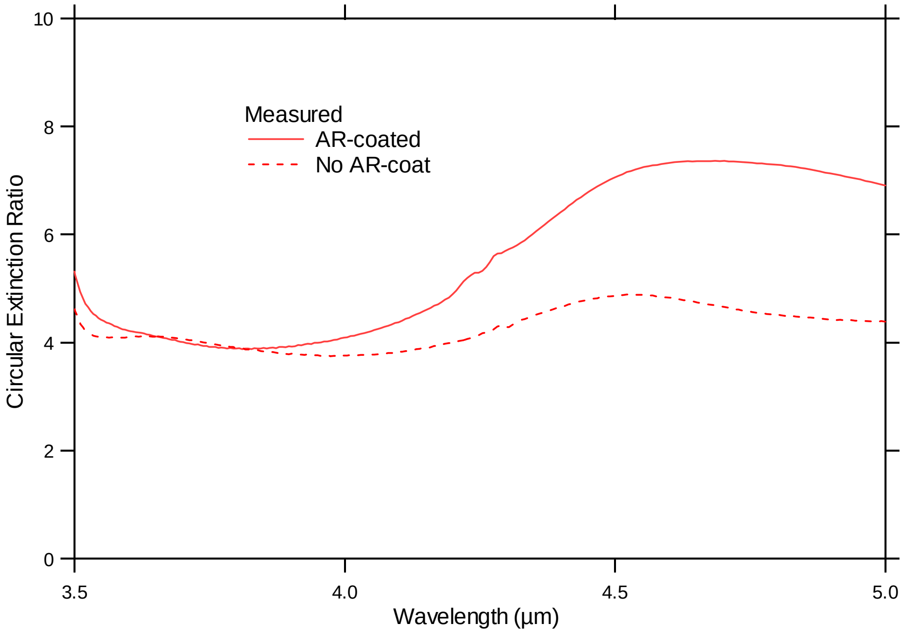

Figure 7.8 Extinction ratio of Stack I sample with an SU-8 AR-coat.

The explanation is due to the birefringent property of the stack and the multiple reflections occuring within the substrate. Initially, the incident circularly polarized light can be decomposed into two orthogonal components having equal amplitude and a phase difference of 90°. However, after reflection from the stack (consisting of a birefringent QWP, SU-8 and polarizer layers), the birefringent nature of the grating structures will cause a deviation from the 90° phase difference and equal amplitude conditions. Without an AR-coating in the backside, the multiple reflections involving the stack continually deteriorate the circular polarization into elliptical polarization. Since elliptical polarization contains both RCP and LCP light, then what was once, for example, pure LCP input will have a growing presence of the RCP component after successive multiple reflections. Since RCP light is highly transmitted by the circular polarization filter, even a small trace of this undesired RCP radiation can be significant. The LCP mode is affected most by this degradation because the circular polarizer was designed to block this component and therefore more light intensity undergoes multiple reflection (between the back surface and the SWG stack) for this mode than with the RCP.

The circular ER is plotted as a function of wavelength in Figure 7.9(b). The measurement of ER yielded values from 11 to 14 across the wavelength range, which is 2 to 3 times larger than the case without AR-coating. The AR-coating therefore minimized the depolarizing effect of reflections from the birefringent stack.

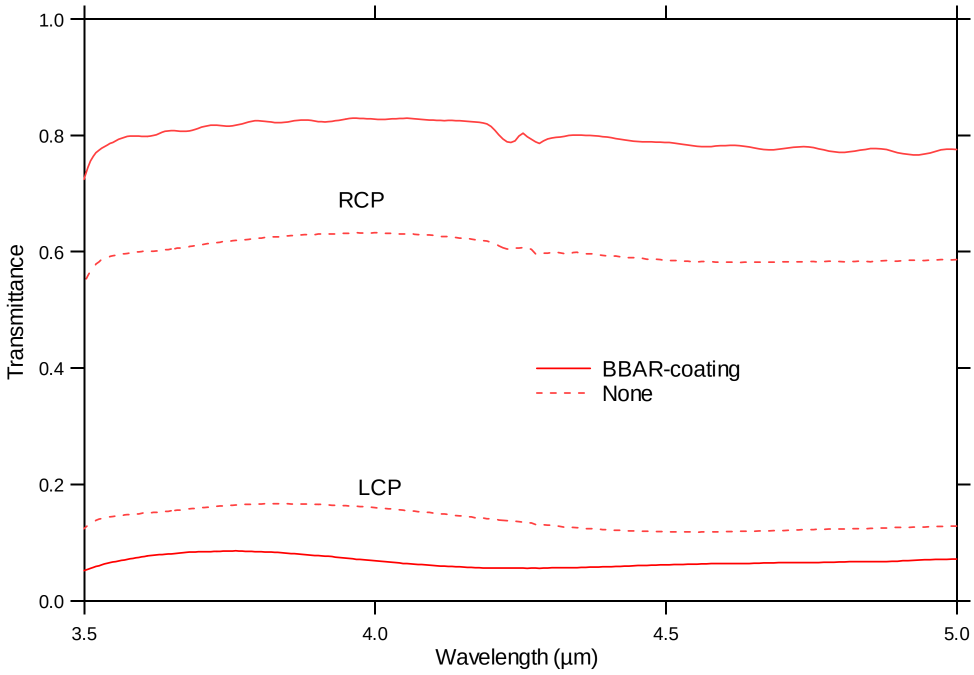

(a)

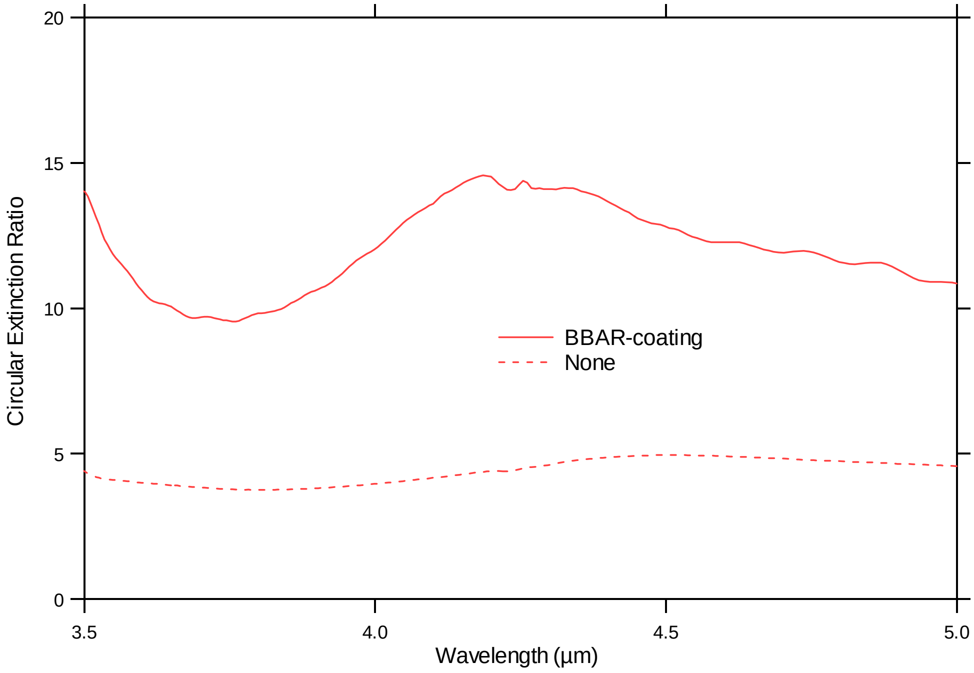

(b)

Figure 7.9 (a) Transmittance and (b) extinction ratio measurements of a Stack I sample before and after receiving a BBAR-coating.

The SRG-RCWA simulations were performed for the BBAR-coated sample. The RCP and LCP transmission results from measurement and simulations are plotted as a function of wavelength in Figure 7.10(a). The layer parameters used in these Stack I simulations are the same as those listed earlier in Table 7.2 with the exception of the silicon substrate which is no longer considered due to the presence of the broadband AR-coating. There is excellent agreement for the RCP mode. The LCP measured values are higher than simulation results and can be attributed to imperfections in the polarizer fabrication mainly due to planarization layer problems. Some regions are missing wire grid gratings and are therefore transparent to any incident polarization. The circular ER ($\equiv T_{RCP}/T_{LCP}$) is very sensitive to LCP transmission because it is in the denominator. This is reflected by the apparent difference in circular ER values between SRG-RCWA simulations and measurements shown in Figure 7.10(b). Jones Matrix simulations of the stack (which neglect the thin film nature of the stack components and consequent multiple reflections) also predicted higher circular ER values.

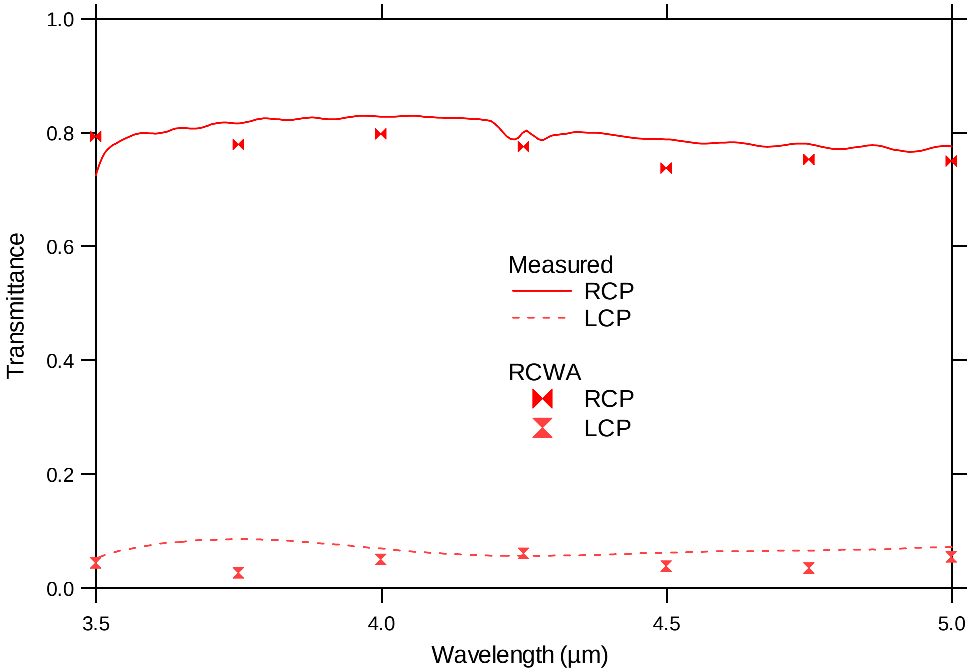

(a)

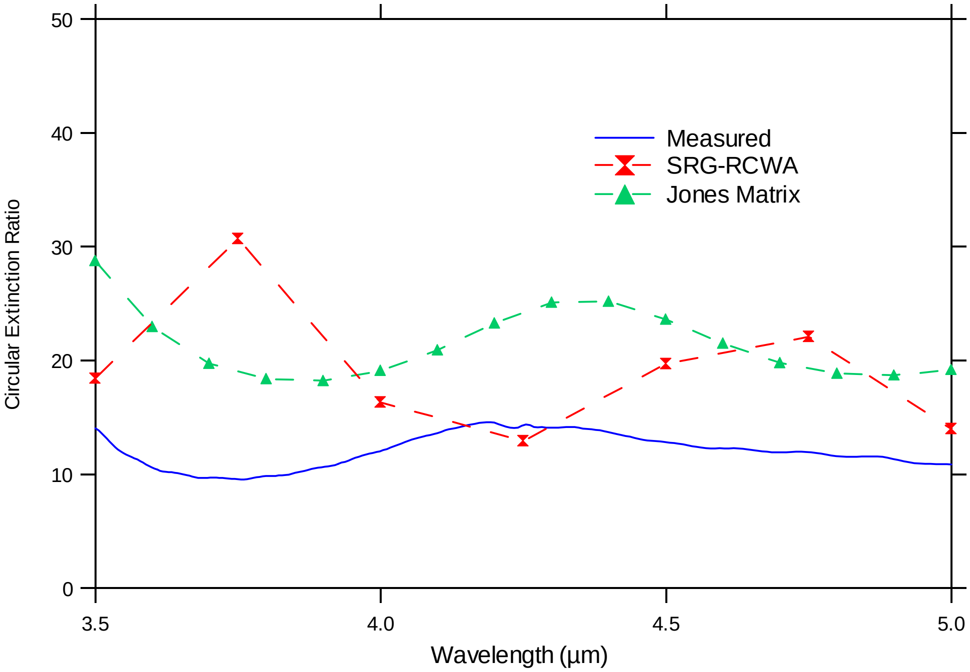

(b)

Figure 7.10 (a) Transmitance and (b) extinction ratio of a BBAR-coated Stack I sample comparing the results from measurement and simulations.

7.3 Improved Stack I Circular Polarizer

To improve the circular ER of the stack, we decided to improve the linear extinction ratio of the the wire grid polarizer by increasing its thickness. The original wire grid consists of wires with 160 nm thick Mo and 25 nm thick Cr. We increased this to 240 nm Mo and 55 nm Cr. The fabrication is the same procedure as the previous Stack I polarizer, except that the thicker Mo layer is deposited and therefore required a longer RIE etch.

An SEM cross-sectional image of the stack is shown in Figure 7.11. The cleaved sample was tilted to allow direct viewing of the polarizer grating lines, such that the QWP gratings are oriented 45°. The thicker wire grid polarizer layer is above a 2-layer SU-8 planarization layer.

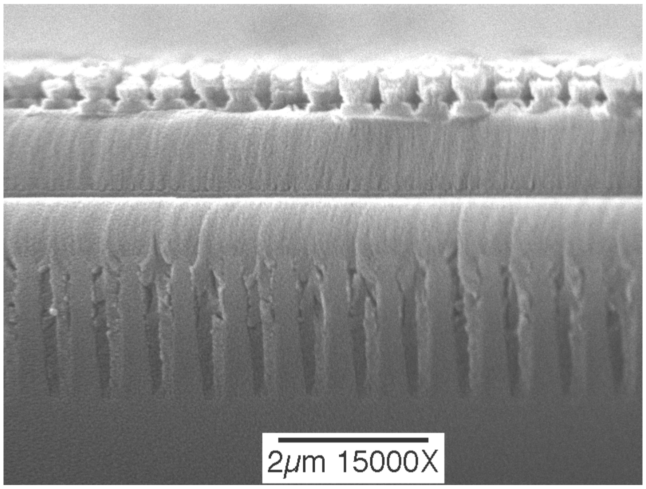

Figure 7.11 An SEM cross-sectional image of a Stack I circular polarizer with a thicker polarizer grating layer.

7.3.1 Performance

The layer parameters used in the stack simulations are given in Table 7.3. In Figure 7.12(a), the measured transmission of RCP and LCP incident illumination is plotted as a function of wavelength for the BBAR-coated sample shown above. The corresponding SRG-RCWA results are plotted with the measurements. The transmission is reasonably high, ranging from 70% to 80%. Measurement and simulation results for RCP illumination are in good agreement. The measured LCP transmission is larger than what is predicted because of damaged areas on the wire grid polarizer where radiation of any polarization state will pass through. There is however qualitative agreement between the curves. Figure 7.12(b) shows the circular ER as a function wavelength. Measured values range from 10 to 65. Better circular ER performance was measured as a consequence of the higher extinction ratio of the linear polarizer component.

Table 7.3 Layer parameters for improved Stack I circular polarizer.

Layer	Thickness (μm)	Fill Factor
Cr	0.055	70%
Mo	0.25	47%
SiO_2	0.1	100%
SU-8	2.1	100%
QWP	1.0	44%
QWP	0.85	50%

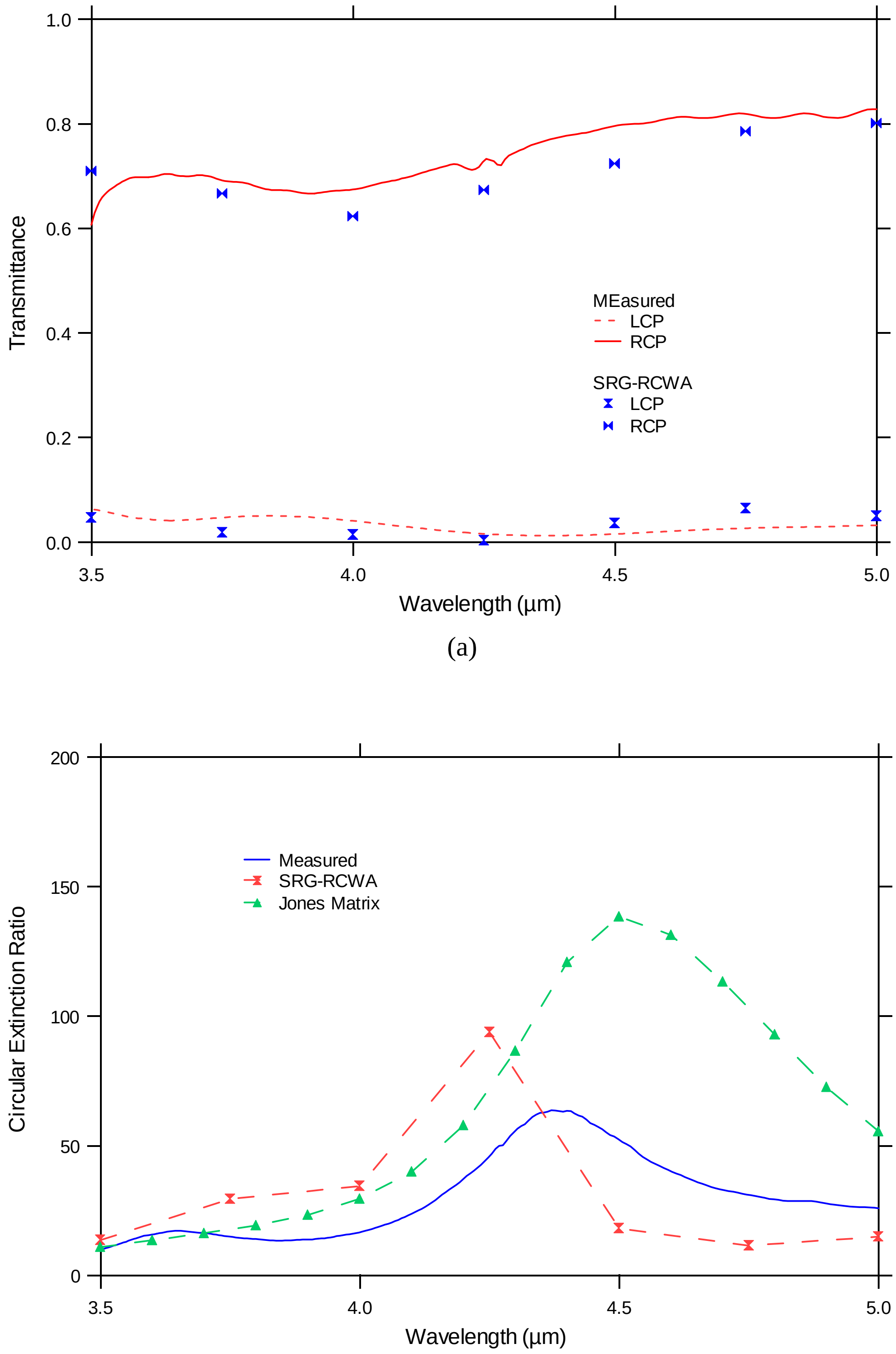

(a)

(b)

Figure 7.12 (a) Transmittance and (b) extinction ratio of Stack I sample with thicker polarizer layer.

7.4 Circular Polarizer: Stack II

The second design for the circular polarizer is labeled Stack II and differs from Stack I by the use of Polarizer II, the 1.0 μm period polarizer discussed in Section 6.2. The use of a contact aligner offered several advantages as well as disadvantages compared with interference lithography. The contact mask aligner requires very short setup time, exposure time and better repeatability. The disadvantage of using contact printing is the necessity of providing a very flat surface for the photomask to make uniform contact across the grating region. The planarization layer should therefore be free of defects such as particulates and air bubbles.

7.4.1 Fabrication of Circular Polarizer: Stack II

Fabrication of Polarizer II, the 1.0 μm period wire grid polarizer has been discussed in Section 6.2.2. The success of stacking this polarizer over the planarized QWP using contact printing relied on providing a defect-free planarization layer such that uniform contact can be made between the photoresist and the photomask. A particulate stuck between the mask and the wafer would force a separation and cause resolution problems in that area. The use of an ARC layer that is coated over the Mo layer assists in smoothing out the non-uniformity on the surface.

A 160 nm layer of Mo is initially deposited over the planarization layer, followed by an ARC layer and then a photoresist layer. The resist is then patterned by contact printing and is followed by a lift-off procedure to replicate the photoresist grating pattern with the Cr metal that is deposited. To produce a high ER polarizer, a thick Cr layer is desired and 240 nm was deposited. The Cr grating pattern is next used as an etch mask to pattern the Mo layer. The resultant polarizer is then a combination of a Cr wire grid and a Mo wire grid layers.

An SEM cross section of a Stack II sample is shown in Figure 7.13 (the sample shown has a protective SU-8 layer covering the stack). The single layer of SU-8 AR-coating is at the backside (not shown). The cleaved sample was tilted 45° to allow direct viewing of the polarizer grating lines. From this point of view, the QWP gratings are oriented 45° and its horizontal dimension is compressed by a factor of $\sqrt{2}$. Because of the protective SU-8 layer over the stack, very few Cr gratings are visible.

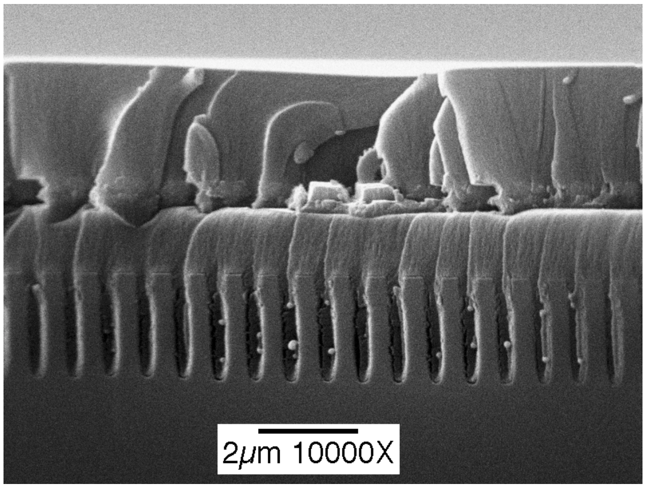

Figure 7.13 An SEM cross-sectional image of a Stack II sample that has an SU-8 AR-coating on the backside (not shown).

7.4.2 Performance of Stack II

Stack II circular polarizers were measured using the FTIR spectrometer. We discuss the three cases of having no AR-coating, a single layer SU-8 AR-coating and a broadband AR-coating.

7.4.2.1 Stack II: No AR-Coating

The performance of the Stack II sample shown in Figure 7.13 was measured before applying a single layer SU-8 AR-coating. The layer parameters used in the stack simulations are given in Table 7.4. The measurement and simulation results for the circular ER and transmission of RCP and LCP illumination as a function of wavelength are shown in Figure 7.14. Measurement of the circular ER yielded low values from 5 to 7.5 across the desired wavelength range. The SRG-RCWA simulations also predict low ER values of approximately 5 and are in agreement with the measured low circular ER values. We look at the improvement gained by the use of an AR-coating which reduces the multiple reflections involving the birefringent SWG stack.

Table 7.4 Layer parameters for Stack II circular polarizer.

Layer	Thickness (μm)	Fill Factor
Cr	0.27	58%
Mo	0.16	41%
SiO_2	0.1	100%
SU8	1.47	100%
QWP	1.53	54.2%
QWP	0.5	61.3%
Si	330	100%

7.4.2.2 Stack II: Single Layer AR-Coating

A Stack II circular polarizer was AR-coated with a single layer of SU-8. The layer parameters used in the Stack II simulations with the single layer AR-coating are given in Table 7.5. The measured circular ER is shown in Figure 7.14. There is a significant increase in the ER values at longer wavelengths where multiple reflection is suppressed with the SU-8 AR-coating, while the shorter wavelength region is mainly unaffected. Circular ER values as high as 33 are achieved, which is a four-fold increase over the non-AR coated case. There is again agreement between measurement and SRG-RCWA results. A broadband AR-coating was next applied to a second sample to improve the transmission and polarization performance of the sample across the entire 3.5 to 5 μm wavelength range.

Table 7.5 Layer parameters for Stack II sample with an SU-8 AR coating.

Layer	Thickness (μm)	Fill Factor
SU8	2.34	100%
Cr	0.27	58%
Mo	0.16	41%
SU8	1.47	100%
QWP	1.53	54.2%
QWP	0.5	61.3%
Si	330	100%
SU8	2.5	100%

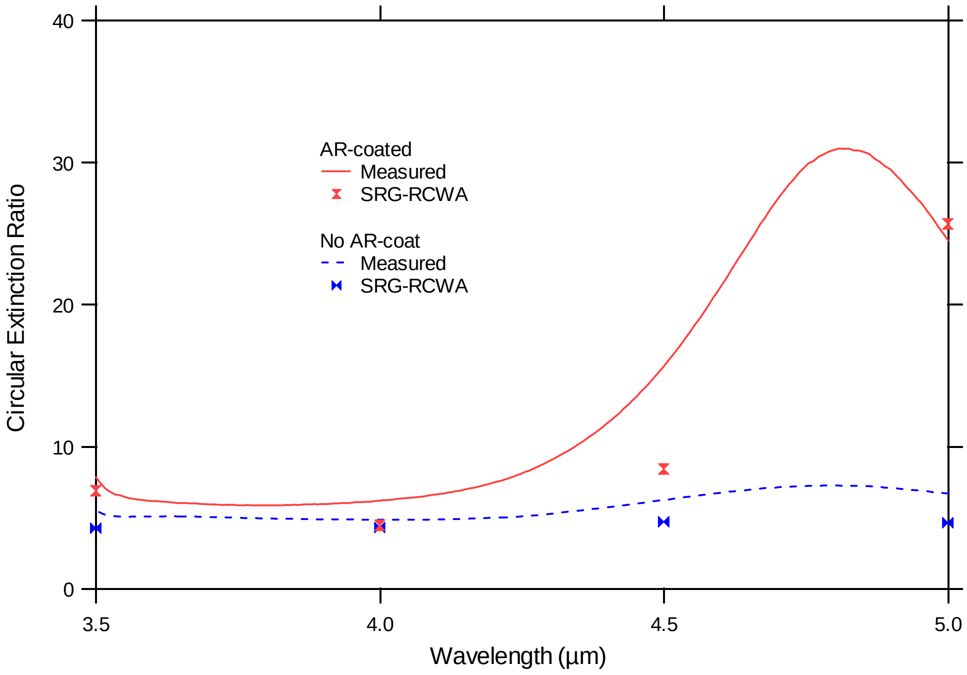

Figure 7.14 Extinction ratio as a function of wavelength for the Stack II sample before and after receiving an SU-8 single layer AR-coating.

7.4.2.3 Stack II: Broadband AR Coating

A second Stack II circular polarizer sample, shown in Figure 7.15, received the BBAR-coating at the wafer backside. The cleaved sample was tilted 45° to allow direct viewing of the polarizer grating lines. From this point of view, the QWP gratings are oriented 45° and its horizontal dimensions are compressed by a factor of $\sqrt{2}$. The Cr grating is 0.3 µm, which is 60 nm thicker than the previous sample. The 160 nm Mo grating was etched with very little undercutting while the SiO2 layer acted as the etch stop layer. The SU-8 layer adequately planarized the 2.1 µm deep QWP surface relief structure.

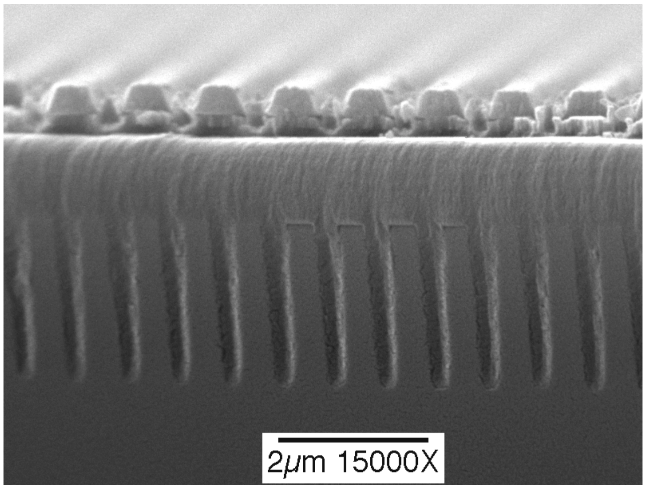

Figure 7.15 An SEM cross-sectional image of a Stack II circular polarizer.

The layer parameters used in the simulations of the Stack II sample having the BBAR-coating are given in Table 7.6. Measurement and simulation results of the RCP and LCP transmittances are given in Figure 7.16(a). There is good agreement between the measurement and simulation results across the 3.5 to 5μm wavelength range. The Stack II sample transmits approximately 50% to 60%, which is significantly lower than the Stack I transmission (~80%). The circular ER is plotted as a function of wavelength in Figure 7.16(b). The measured circular ER yielded values of 10 to 45. Because of the sensitivity of the circular ER calculation to small differences between measurement and simulation results of the LCP transmittance, there is a noticeable disparity between the circular ER values obtained from measurement and simulations as shown in Figure 7.16(b). The Jones Matrix approach also predicts higher values. The difference may be partly due to the optical constants of Cr used in the simulations. The exact values for the evaporated Cr are unknown and instead the optical constants from RF sputtered Cr was used.

Table 7.6 Layer parameters for Stack II sample with BBAR-coating.

Layer	Thickness (μm)	Fill Factor
Cr	0.2	50%
Cr	0.1	70%
Mo	0.16	58%
SiO_2	0.1	100%
SU8	1.3	100%
QWP	2.1	52%

7.5 Conclusion

Circular polarizers were implemented from the stacking of the form birefringent QWP and the wire grid polarizer. Two circular polarizers designs were investigated, labeled as Stack I and Stack II, which correspond to the integration of the QWP with Polarizer I and Polarizer II, respectively. We initially analyzed stacked gratings using the Jones Matrix method to predict the circular ER performance as a function of the non-ideal properties of the QWP and polarizer. We estimated fabrication tolerances on the QWP and the polarizer in order to achieve a circular ER goal of 10 to 20.

The critical step in the integration of the QWP and the polarizer was the planarization of the QWP surface relief. Surface defects on this layer lead to non-uniform patterning of the photoresist. In interference lithography, such non-uniform patterning resulted in certain areas where wire grid polarizers were absent. In contact lithography, particulates and bubbles

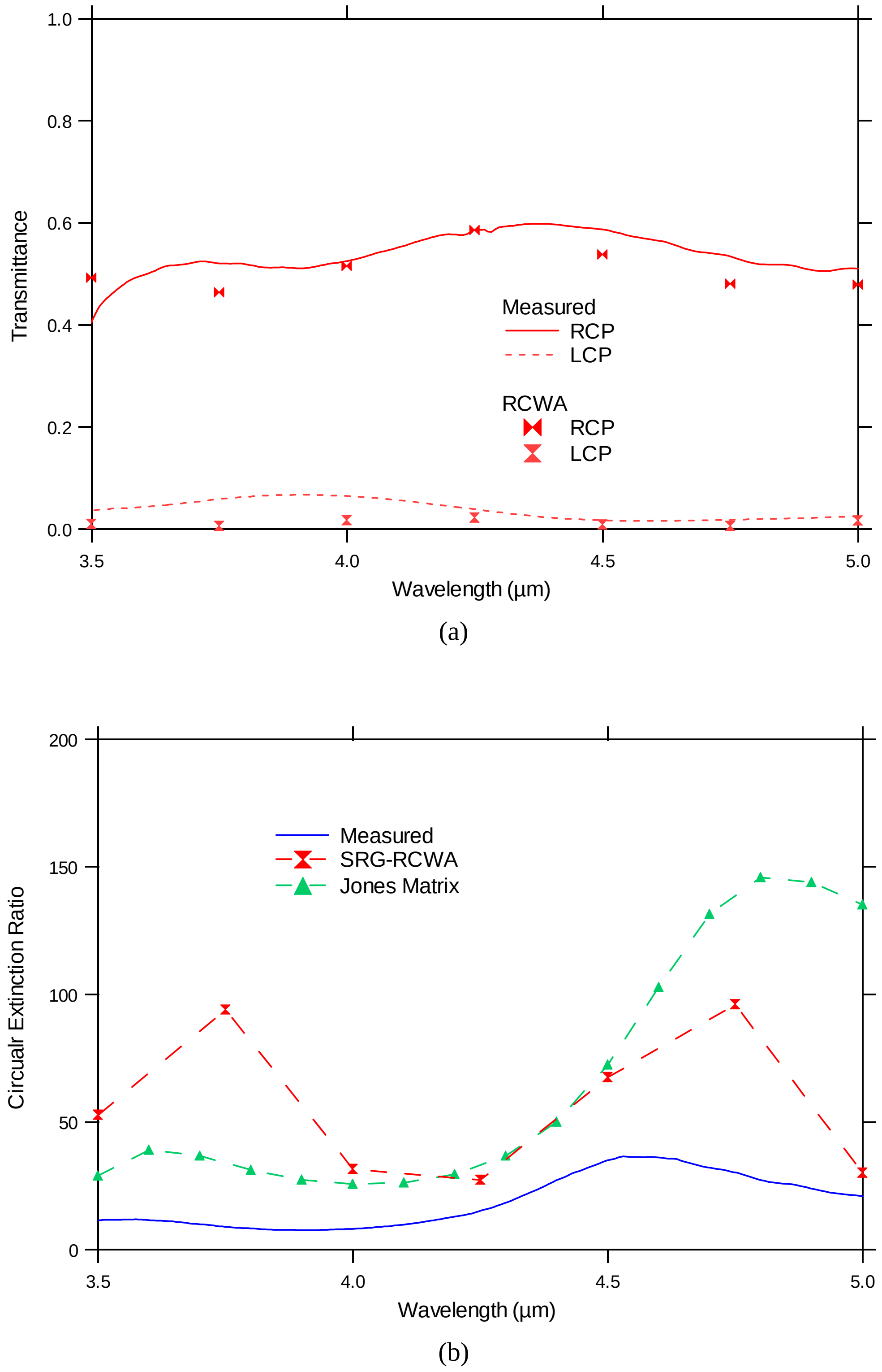

Figure 7.16 (a) Transmittance and (b) extinction ratio of a BBAR-coated Stack II sample comparing the results from measurement and simulations.

prevented good contact between mask and resist such that successful transfer of mask pattern to the resist was difficult. The SU-8 planarization procedure is continually being improved to reduce the surface defects.

The AR-coating was found have a critical effect on the performance of the samples by reducing multiple reflections involving the birefringent SWG stack that lead to depolarization. The performance of samples were therefore characterized before and after receiving the AR-coating. To test the performance improvement, a single layer of SU-8 was used as the AR-coating that was only effective within a small wavelength range. The thickness of the SU-8 was chosen such that the AR-coating was effective in the longer wavelength region. The Stack I sample showed a 65% increase in circular ER at the longer wavelengths. The Stack II sample showed over a 300% increase in circular ER at the longer wavelengths.

A broadband AR-coating was applied to several samples to extend the performance improvement across the whole 3.5 to 5 μm wavelength region. Two Stack I polarizers were fabricated with different Polarizer I thicknesses. The first achieved circular ER values ranging from 9 to 13, while the other performed with higher ER values ranging from 15 to 45. The transmission of these Stack I samples are satisfactorily high at 70% to 80%. Stack II circular polarizers performed with high circular ER values, from 10 to 40 across the wavelength range. The transmission of the Stack II samples however was limited to only 50 to 60%. The circular ER performances of both Stack I and II met our goal of achieving a circular ER of 10 to 20.

Chapter 8

CIRCULAR POLARIZATION FILTER ARRAY FOR IMAGING POLARIMETRY

In this chapter, we make the transition from the large aperture circular polarization filters to the 256 x 256 array of small circular aperture polarization filters that will be used for a real-time imaging polarimeter. The design of the SWG structures was performed using RCWA analysis which assumes periodic gratings having infinite area. In the case of the 256 x 256 array, the polarization filters are limited to a finite aperture of 15 μm x 15 μm. In the first two sections, we investigate the response of the form birefringent QWP and the wire grid polarizer to the finite aperture. The following section presents the fabrication of the circular polarization filter array. New photomasks were designed to accommodate the patterning and alignment of the bottom-layer QWP array and top-layer polarizer array. The circular polarization filters are only a subset of the whole micro-optic device which integrates also the multiply-oriented linear polarization filters. (The challenging fabrication of the polarizer array that is patterned above the QWP array is the Master's thesis topic of UAH graduate student Jeff Meier [72].) Complete polarization filter arrays have been fabricated using two approaches and are presented here. We discuss the performance of the filters from measurements taken with an IR microscope.

8.1 Finite Aperture Form Birefringent QWP

The effect of a finite aperture on the form birefringent QWP has not been reported in literature. In this section, we performed an experiment to investigate the phase retardance response of QWP subwavelength grating structures confined within 25 μm x 25 μm apertures. A large area QWP, shown in Figure 8.1(a), was fabricated using the process described in Section 5.2.2 and tested with the FTIR spectropolarimeter. Afterwards, an array of 25 μm x 25 μm window apertures was patterned over the QWP (by contact printing and lift-off) using an opaque layer of Cr (~100 nm) to mask off the outside areas. The phase retardance of this pixel array was again measured. Figure 8.1(b) shows the retardance measurements taken before and after the presence of the finite aperture array. There is minimal difference in phase retardance at the longer wavelengths and only a slight decrease of 3% at the shorter wavelengths. We therefore conclude that the 256 x 256 array of QWP pixels confined within the area of 25 μm x 25 μm behaves much like the large area structure.

8.2 Finite Aperture Wire Grid Polarizer

In this section, we discuss the effect of the finite aperture on the wire grid polarizer from research reported in the literature. Kuta *et al.* investigated the response of lamellar metal transmission gratings in the near IR (1060-1523 nm) experimentally to demonstrate the limitations of applying an infinite grating approximation to model finite period structures [27]. For a 25 period device, they found a high degree of consistency between the RCWA results and measured transmission efficiencies. For a 12 period device, they found a substantial difference between RCWA and experimental data for both the TM and TE polarizations. These results were comparable with another research on finite aperture metal transmission gratings performed by Deleuil [73]. In his work with microwaves, his results indicated that 12 or more periods are required before the grating response approaches that of an infinite structure.

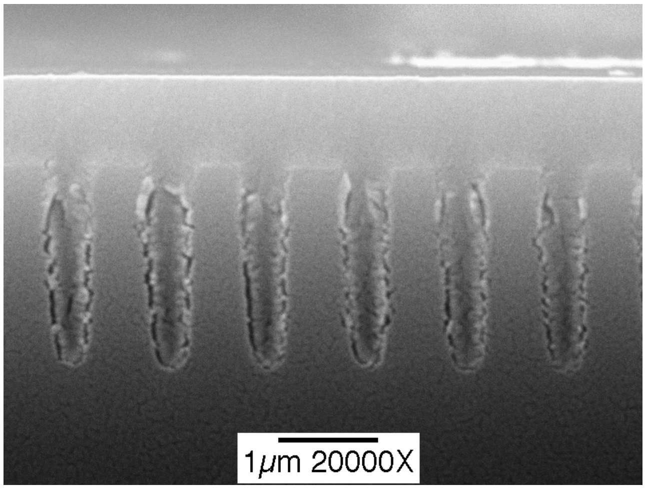

(a)

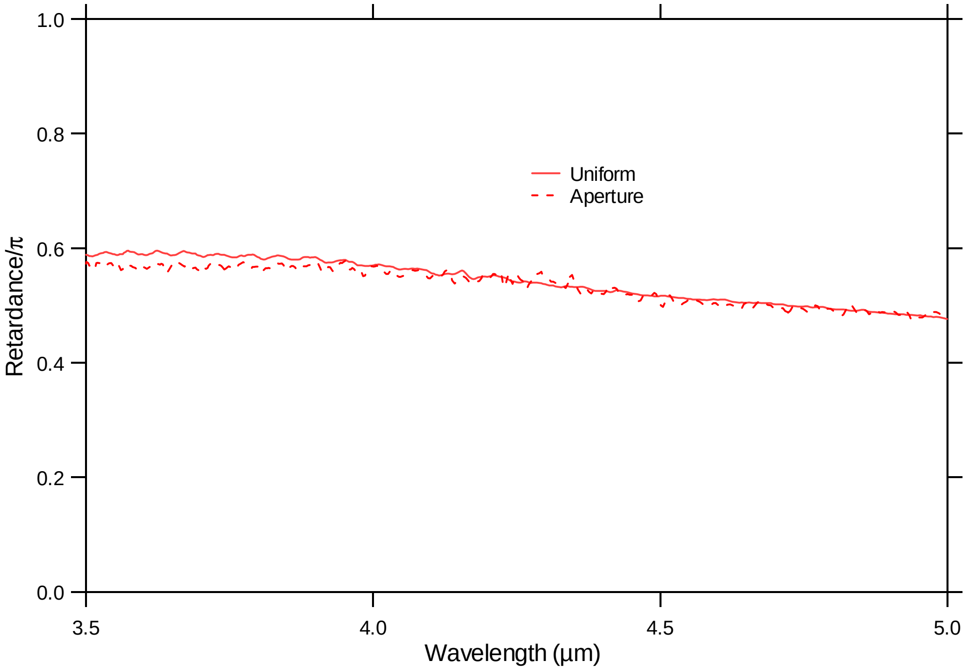

(b)

Figure 8.1 (a) An SEM cross-sectional image of a uniform form birefringent QWP and (b) its measured phase retardance as a function of wavelength when a finite-aperture is absent and present.

Recently, Jensen and Nordin performed Finite-Difference Time-Domain (FDTD) simulations on finite aperture wire grid polarizers [74] and they found that the electrical size of the aperture is the important parameter that determines the aperture effect. If the aperture is larger than the wavelength of the incident radiation, then the behavior of the wire grid polarizer can approach that of the large area structure. The apertures of the wire grid polarizers used in our mid-wave IR (3.5 to 5 μm) application are 15 μm x 15 μm. Applying either criteria of the number of periods or electrical size, the research findings discussed above indicate that the aperture effect will not be significant.

8.3 Fabrication of Circular Polarization Filter Array

The 256x256 array of circular polarization filters is only one quarter of the 512x512 polarization filter array present in the micro-optic device. Appropriate photomasking steps were used to delineate these SWG stacks (QWP and polarizer arrays) from the linear-only polarization filters. Alignment marks consisting of grids and squares were used to position the multiple arrays in their proper location to within a micron or two of accuracy.

8.3.1 QWP Array Fabrication

The fabrication of the QWP array is identical to the procedure used in the large aperture QWP fabrication described in Section 5.2.2. A different photomask is used which contains a 256 x 256 array of 25 μm x 25 μm pixels of 1 μm period Cr lines and spaces. The patterning, lift-off, and etching resulted in QWP array etched into the silicon substrate, as shown in Figure 8.2. Alignment grid marks are etched along the wafer sides so that the subsequent fabrication of the polarizer array is appropriately aligned above the QWP array.

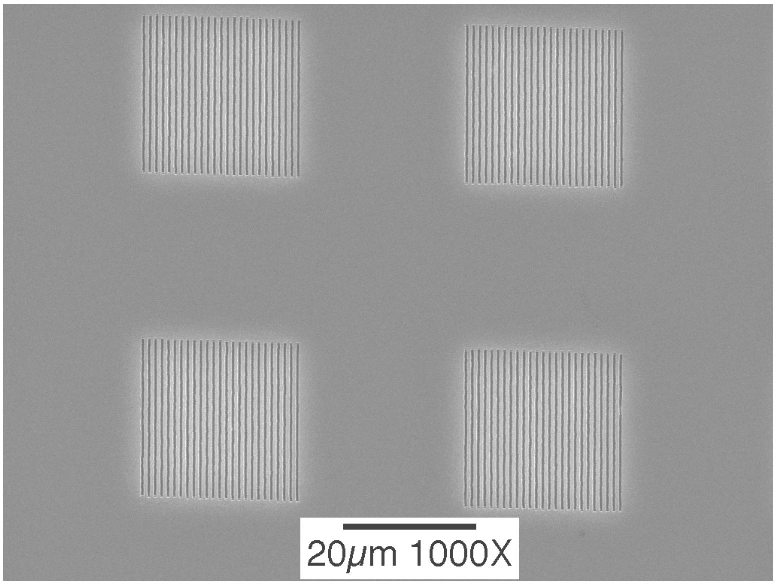

Figure 8.2 An SEM image of QWP pixels from the 256 x 256 array.

8.3.2 Polarizer Array Fabrication

The fabrication of the polarizer array is the Master's thesis topic of J. Meier, as mentioned earlier. Only an overview of the procedure is presented here. Fabrication of the polarizer array above the QWP array by interference lithography required several photomasking steps to define the wire grid patterns in the appropriate apertures. There are 3 polarizer orientations in the array: 0°, 45° and 90°. Three successive interference lithography steps were therefore needed. A photomask is used to define the location of the filters for each orientation.

The procedure is identical to the large area wire grid polarizer case. In that process, the photoresist is exposed in the interference lithography setup to create the 0.5 μm grid period grating. A lift-off method follows to create a Cr etch mask that has the desired wire grid pattern. Then, the pattern is transferred to the Mo layer by RIE.

In the fabrication of the polarizer array, a photomasking step is added to define which pixel windows will be patterned. First, the 0° grating orientation is patterned on the resist in the appropriate location and a lift-off method is used to create a Cr etch mask with that 0° orientation. This process is repeated for the 45° and the 90° orientations resulting in an array of Cr etch masks having three different grating orientations. After achieving the complete set of Cr etch masks that define the 0°, 45° and 90° orientations in specific windows, the Mo layer is then etched and a polarizer array is fabricated.

8.3.3 QWP-Polarizer Array

A complete micro-optic device has been fabricated in the manner outlined above. A cross section of a single circular polarization filter in the array is shown in Figure 8.3. The orientation of the polarizer is rotated 45° degrees with respect to the QWP axis. The QWP is planarized by a 1.6 μm SU-8 layer. An SiO_2 layer served as the etch stop for the Mo layer.

Fabrication of complete micro-optic devices by interference lithography resulted in low yield because three successive exposures were needed. The long exposure times of up to 100 seconds made the photoresist patterning susceptible to instability in the setup (e.g., laser power, vibration). Since the patterning of the micro-polarizer array was the cause of the low yield, another approach of patterning was considered.

Electron beam lithography provided the most direct way to pattern the wire grid polarizers having different angular orientations. We used an electron-beam writer at the Cornell Nanofabrication Facility to create the micro-polarizer array pattern above the QWP array using PMMA resist. Since grating fingers are written individually, exposure times lasted for approximately 4 hours per wafer. The most direct method of patterning is also the most expensive. We discuss the performance of the stacked QWP-polarizer array in the next section.

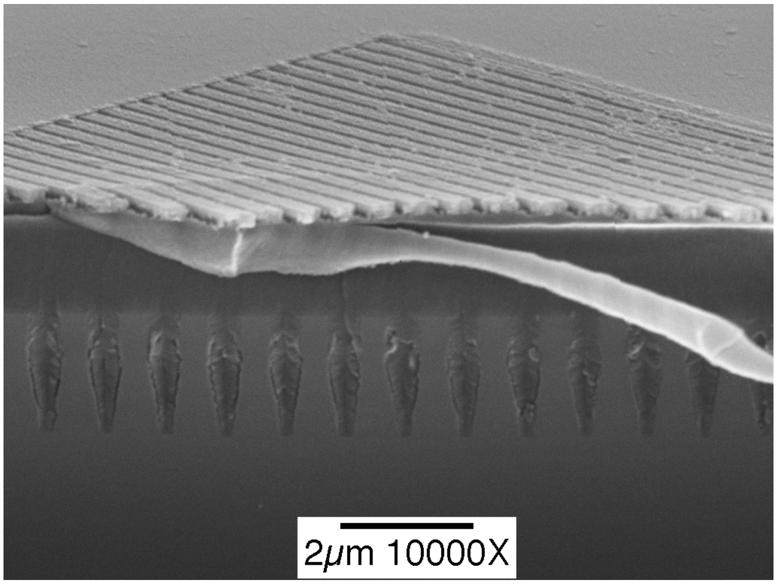

Figure 8.3 An SEM cross-sectional image of a SWG stack pixel in the 256 x 256 array of circular polarization filters.

8.4 Performance of Circular Polarization Filter Array

The performance of the array of circular polarization filters was tested with an IR microscope. The diagram of the testing apparatus is shown in Figure 8.4. A black body source is heated to 800°C to produce an adequate supply of radiation in the mid-wave IR. A filter is inserted to pass radiation in the 3 to 5 μm wavelength range. A wire grid polarizer and an achromatic QWP made from two birefringent plates, cadmium sulfide and cadmium selenide [68], were used to generate the incident circularly polarized wave that is focused by a lens onto the micro-optic device. An adequate number of pixels are illuminated and their image is projected by a microscope objective lens to the focal plane array detector.

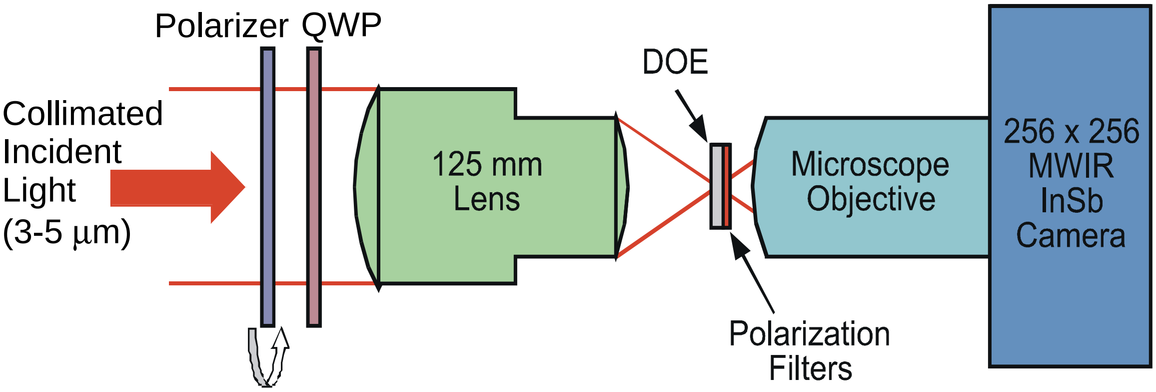

Figure 8.4 Diagram of the IR microscope testing setup.

Infrared microscope images of the polarization filter array were taken with the 256 x 256 MWIR InSb camera. Different incident polarization states were generated by rotation of the polarizer from -90° to +90° while the QWP fast axis was fixed at 0°. Nominal circular polarization states, RCP and LCP, resulted when the polarizer axis was rotated to the -45° and +45° orientations, respectively. Linear (horizontal and vertical) polarization states occurred at 0° to 90°, along the direction of the QWP axes.

Figure 8.5 shows the IR microscope images of the micro-optical polarization filters under illumination from linear and circular polarization states. (Only a subset, a 4 x 4 pixel array, of the whole image is shown for comparison. A unit cell of the polarizer array is inserted to remind the observer where each filter is situated.) The extinction ratio values of the filters were measured by sampling representative pixels using Igor Pro software to provide 8-bit (0 to 255) intensity values within a pixel region. The linear polarization filters show very good extinction ratio performance of approximately 40. The circular extinction ratio (=T_{RCP}/T_{LCP}) of the circular polarization filters can be measured from the image intensities at a representative pixel. A circular extinction ratio of 5.2 was measured for the circular polarization filter.

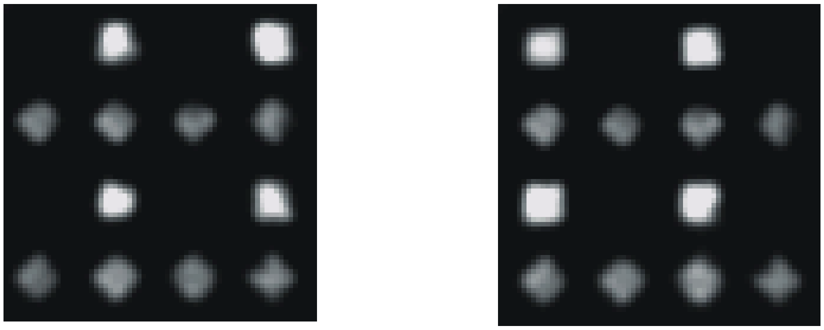

Vertical Horizontal

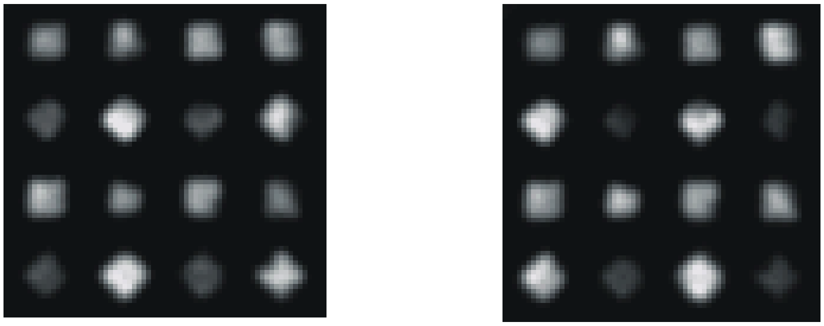

RCP LCP

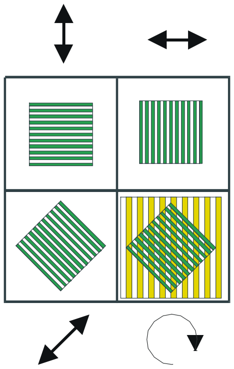

Figure 8.5 IR microscope images of the micro-optic polarization filters under different input polarization states.

A factor contributing to the low circular ER is due to the non-ideal phase retardance of the QWP. The measurement of the retardance gave a range from 77° to 84° (or 0.43π to 47π) over the wavelength region of 3.5 to 5 µm, as shown in Figure 8.6. The effect of the resultant elliptical polarization can be seen in the IR images of the 45° linear polarization filters. For circularly polarized illumination, the linear filter should equally transmit RCP and LCP radiation. But it is evident that this filter is much brighter when RCP illumination is incident than when LCP illumination is incident.

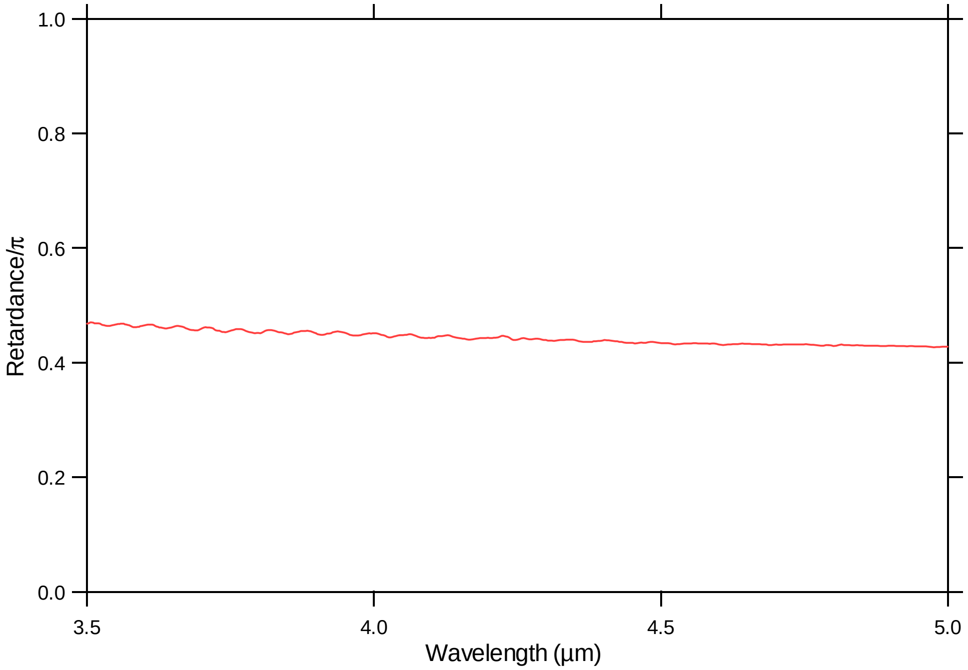

Figure 8.6 Retardance as a function of wavelength for the achromatic QWP that is used to generate nominal circular polarization states.

In comparison with large area circular polarization filters, this circular ER of small aperture filters value is approximately half that of the large area filters. The possible cause in the reduction in performance may be due to depolarizing effects of scattering from the aperture edges and also scattering of light between adjacent polarization filters leading to cross-talk. The Cr masking that defines the apertures for the polarizers will also increase the amount of reflections within the SWG stack and reflections from the birefringent structures will further lead to more depolarizing effects.

8.5 Conclusion

In this chapter, we discussed the transition from the large aperture circular polarization filter to the 256 x 256 array of small aperture filters. The RCWA analysis used in determining the performance of the SWG components and their stacked structure assume periodic gratings having infinite area. We therefore investigated the effect of using small apertures in the array. Experimental verification was performed on the form birefringent QWP and results show that the phase retardance was only slightly affected by the 25 μm x 25 μm aperture. Literature results were presented showing that wire grid polarizers with 15 μm x 15 μm finite aperture should approach the performance of an infinite one. From the results of the finite aperture QWP and wire grid polarizer, we may conclude that the finite aperture effect on the phase retardance of the QWP and the extinction ratio of the polarizer would not be significant in our design.

Fabrication of the micro-optic polarization filter array was accomplished in a couple of ways: interference lithography and electron beam lithography. The yield of the interference lithography system was low due to the multiple exposure and masking steps. Patterning by electron beam lithography improved the yield but raised the expense of fabrication.

The performance of a complete filter array was measured using an IR microscope. The array of linear and circular polarization filters was illuminated with linear and circular polarization states (nominal RCP, LCP, vertical and horizontal polarized light) and microscope images were taken to determine the extinction ratio performance of the filters. The measured circular extinction ratio was 5.2 and was lower than the large aperture case. The possible cause in the reduction in ER performance may be due to depolarizing effects from scattering at the aperture edges that led to cross-talk between adjacent polarization filters and from reflections involving the birefringent structures.

Chapter 9

SUMMARY AND FUTURE RESEARCH

In this dissertation, multi-functional SWG structures were integrated to create a single device that implements a more complex functionality. For an application in imaging polarimetry, SWG components were implemented as the linear and circular polarization filters of an imaging polarimeter for acquiring polarization information from a scene being observed. The stacking of SWG's provided an approach to realize real-time operation. The final micro-optic device is a 512 x 512 pixelated array of SWG structures that is mounted directly on top of the focal plane array of the camera. In this chapter, we summarize the dissertation in Section 9.1 and discuss future research directions in Section 9.2.

9.1 Summary

Chapter 2 provided background information on current applications of SWG's. The fabrication of the form birefringent QWP using a silicon substrate required anisotropic etching of high aspect ratio stuctures and literature search provided some approaches in accomplishing this challenge. The best processes, however, required more advanced systems than were available for this project. Background information on the significance of the Stokes parameters for specification of polarization state and how they are measured is presented.

Chapter 3 introduced the real-time imaging polarimeter design. The SWG's were implemented as linear and circular polarization filters. The focal plane array detector of the imaging polarimeter is a 512 x 512 array. The SWG polarization filter array is directly mounted above this FPA array such that both are spatially registered. The unit cell is a 2 x 2 array consisting of 3 linear polarization filters oriented at 0°, 45°, and 90° and a circular polarizer. This complete set of 4 filters allows the determination of the Stokes parameters at each image pixel. Wire grid polarizers are used as linear polarization filters. The stacked structure of a wire grid polarizer and form birefringent QWP performed as the circular polarization filter.

Chapter 4 described the theoretical analysis methods used in this dissertation to design the SWG components. The subwavelength grating analysis are commonly performed using the EMT and RCWA methods to obtain approximate and rigorous results, respectively. The analysis of stacked diffraction gratings necessitated a new RCWA method to rigorously treat multiple gratings having arbitrary structural parameters and angular orientations. A simplification by treating the stack as cascaded bulk components allowed an analysis using the Jones Matrix calculus. Both the rigorous and approximate treatment of the stack was described in this chapter.

The approach to develop the SWG polarization filters was to develop the individual components first and then integrate them afterwards. Chapter 5 presents the development of the broadband form birefringent QWP. The easier case to verify the proper operation of the SWG design implementing a QWP functionality was a silicon-air component. The design required modest features to fabricate. The phase retardance performed within 88° to 100° and simulation results compared well with measurement results. The structure desired for the imaging polarimeter was the silicon-SU-8 QWP. The design required stringent features that posed quite a fabrication challenge with resources that were available. The planarized QWP performed with good achromatic behavior in the 3.5 to 5 μm wavelength range achieving retardance values from 83° to 97°.

Chapter 6 presents the development of the wire grid polarizer. Two designs were investigated to determine the feasibility of using them for the imaging polarimeter. Polarizer I was patterned with a grating period of 0.5 μm using interference lithography. An extinction ratio of 40 was achieved and can be improved by using a thicker metal layer without changing the process. Polarizer II had a grid period of 1 μm and was patterned with contact printing. A very thick Cr layer was used to compensate for the ER loss due the larger grating period. An extinction ratio of 250 was measured.

Chapter 7 presents the integration of the QWP and the polarizer in the large area case. Since there were two polarizer designs, two stack designs were investigated. The stack performance was degraded by multiple reflections involving SWG form birefringence; therefore, measurements were taken of samples with and without AR-coating. Single layer AR-coats were initially shown to improve the ER for only a short wavelength range. A broadband multi-layer coat was then applied to other samples to improve the ER across the whole 3.5 to 5 μm wavelength range. Stack I, consisting of the 0.5 μm period polarizer and the QWP, performed with a circular ER values within 4 to 5 without AR-coating and increased to 10 to 14 after AR-coating. Transmission across the stack was approximately 80% over the entire wavelength range. An improved circular ER performance was accomplished by increasing the thickness of the polarizer. The circular ER was measured between 10 to 55 in the wavelength range. Stack II, consisting of the 1 μm grid period polarizer and the QWP, had a measured circular ER of 5 to 7 without AR-coating and increased to 10 to 40 after the AR-coating. Transmission through this component was approximately 50% across the wavelength range. The advantage of using the 0.5 μm polarizer is the higher throughput. The advantage of using the 1 μm polarizer may be in fabrication repeatability. Despite using a 120 mW HeCd laser, interference lithography exposures were 30 to 40 times longer in comparison to contact printing and thus susceptible to stability problems.

Chapter 8 presents the pixel array of polarization filters and in particular, the circular polarization filters were implemented by stacked SWG's. Finite aperture effects were investigated by masking the large area QWP with an opaque Cr layer except for an array of square windows 25 μmx25 μm in area. The phase retardance measurement showed the minimal effect of the finite aperture. Research on finite aperture effects on polarizers indicated that 30 periods contained in the 15 μmx15 μm apertures of the Stack I polarizers is sufficient to approximate the behavior of an infinite structure. A complete micro-optic device was fabricated and performance of the pixelated structure was measured with an IR microscope. Images of the pixels for linear and circular incident polarization states show that the filters are functioning properly. A Stack I filter was measured to have a circular ER of approximately 5.2. The exact structural parameters of this sample is not known to perform simulation comparisons because it was mounted subsequently to a focal plane array. Possible cause of the low circular ER value may be scattering of light between adjacent pixels leading to cross-talk and the depolarizing effect of reflections from the birefringent structures.

9.2 Future Research

The goal of this project is to develop a real-time imaging polarimeter by mounting a micro-optical polarization filter array directly on top of the focal plane array of the camera. In this dissertation, three methods of fabricating the circular polarization filters using stacked SWG's were developed which involve contact printing, interference lithography and electron beam lithography. From initial investigations, stacked SWG's have performed with satisfactory results achieving circular ER values from 10 to 65 across the 3.5 to 5 μm wavelength range for large area filters. In the transition to the small aperture filter array, one of the designs (Stack I) achieved a circular ER value of 5.2. Further development is needed to improve the performance and some suggestions follow.

The circular ER of the stack can be improved by improving the individual SWG components. As was shown for Stack I samples in Section 7.3, a thicker polarizer grating layer can be used to raise the overall circular ER. The polarizer fabrication process remains basically unchanged. The broadband form birefringent QWP fabrication also requires further improvement. The etching of silicon using a basic RIE system is not sufficiently anisotropic to fabricate the design at the optimum grating parameters. Successful high-aspect-ratio etching of silicon reported in literature has been accomplished using more advanced systems, such as an ICP RIE discussed in Section 2.2. The improvement of the QWP broadband retardance and TE and TM transmittance would significantly increase the circular ER of the stack. Future use of an ICP RIE should be considered to improve the anisotropic etching of silicon.

Another method to raise the circular ER of the polarization filter array is to use the Stack II design. New masks will be needed; however, the costs are relatively inexpensive compared to the use of electron-beam lithography. Fabrication can be accomplished quickly and with repeatability if the planarization problems described in Section 7.4.1 can be improved.

The stack fabrication using electron-beam lithography is very attractive because it is the most direct method of patterning the wire grid array pattern above the QWP array. The electron beam resist receives the same amount of energy dose across the whole filter array and will be uniform, in contrast to the multiple exposures required in interference lithography which can have repeatability problems due to the long exposure times. Future research using this e-beam method should look at increasing the wire grid polarizer thickness and decreasing the grid period to increase the circular ER.

Further research is needed to determine why the circular ER lowered when the stack was fabricated as the polarization filter array. Scattering of light between adjacent polarization filter pixels is most likely leading to cross-talk. From the small aperture results gathered from the finite aperture QWP and wire grid polarizer, the finite aperture does not appear to be a significant factor in the performance loss. To directly measure the effect of the finite aperture on the SWG stack, it is straightforward to apply a Cr mask over the large area Stack I or Stack II samples such that small aperture arrays are created. The circular ER of these filters can be measured with the FTIR. The results from this array of small aperture circular polarization filters can be compared with the results of the array of small apertures of both linear and circular polarization filters to investigate the cross-talk. In addition, the mounting of the micro-optic device is critical to avoid any mis-registration with the focal plane array which would be another source of cross-talk.

APPENDIX

4 x 4 Method of Berreman

This appendix provides the Matlab code for the 4 x 4 method given by Berreman to treat the propagation of incident polarized light by stratified anisotropic film layers. The anisotropic optical properties of the subwavelength gratings are calculated using the EMT analysis and then used as the input of this 4x4 analysis.

```
clear all
kI=0;    %Assume nonabsorbing incident medium
NI=nI+j*kI;
NII=nII+j*kII;
k=2*pi./W;
for v=1:data_points                    % v=varying parameter of output
  for L=1:num_layers                            % L=layer index
    zTE=emtTE(nR(L,v),kR(L,v),nG(L,v),kG(L,v),P(L,v)*ff(L,v),P(L,v)*(1-ff(L,v)),W(v));
    N_TEbest=zTE(1)+j*zTE(2);
    zTM=emtTM(nR(L,v),kR(L,v),nG(L,v),kG(L,v),P(L,v)*ff(L,v),P(L,v)*(1-ff(L,v)),W(v));
    N_TMbest=zTM(1)+j*zTM(2);
    if (v==1)
      NL=[N_TMbest N_TEbest N_TEbest];      %display first
      inc_wave=W(v);
      substrate_index=NI(v);
             N_ff=nR(L,v)+j*kR(L,v);
    elseif (v==data_points)
      NL=[N_TMbest N_TEbest N_TEbest];      %display last
    else
      NL=[N_TMbest N_TEbest N_TEbest];      %do not display middle
    end
        thetaII(v)=asin((NI(v)/NII(v))*sin(theta(v)));
        eta=NI(v)*sin(theta(v))/c;                     %careful of c!!!!
        e=[NL(1)^2 0 0;0 NL(2)^2 0;0 0 NL(3)^2];  %TE=s and TM=p
        I=[1 0 0;0 1 0;0 0 1];
        u=I;
    if(rot(L,v) ~= 0)
      CCWfile=1;
        ta=rot(L,v);
        Rw=[cos(ta) sin(ta) 0; -sin(ta) cos(ta) 0; 0 0 1];
        R_L=[cos(ta) -sin(ta) 0; sin(ta) cos(ta) 0; 0 0 1];
        e=Rw*e*R_L;
    end
    p=[0 0 0;0 0 0;0 0 0];
    pp=p;
    M=[e p;pp u];
    Q=M(3,3)*M(6,6)-M(3,6)*M(6,3);
```

```
    A1=(M(6,1)*M(3,6)-M(3,1)*M(6,6))/Q;
    A2=((M(6,2)-eta)*M(3,6)-M(3,2)*M(6,6))/Q;
    A3=(M(6,4)*M(3,6)-M(3,4)*M(6,6))/Q;
    A4=(M(6,5)*M(3,6)-(M(3,5)+eta)*M(6,6))/Q;
    A5=(M(6,3)*M(3,1)-M(3,3)*M(6,1))/Q;
    A6=(M(6,3)*M(3,2)-(M(6,2)-eta)*M(3,3))/Q;
    A7=(M(6,3)*M(3,4)-M(3,3)*M(6,4))/Q;
    A8=((M(3,5)+eta)*M(6,3)-M(3,3)*M(6,5))/Q;

    D(1,1)=M(5,1)+(M(5,3)+eta)*A1+M(5,6)*A5;
    D(1,2)=M(5,5)+(M(5,3)+eta)*A4+M(5,6)*A8;
    D(1,3)=M(5,2)+(M(5,3)+eta)*A2+M(5,6)*A6;
    D(1,4)=-(M(5,4)+(M(5,3)+eta)*A3+M(5,6)*A7);
    D(2,1)=M(1,1)+M(1,3)*A1+M(1,6)*A5;
    D(2,2)=M(1,5)+M(1,3)*A4+M(1,6)*A8;
    D(2,3)=M(1,2)+M(1,3)*A2+M(1,6)*A6;
    D(2,4)=-(M(1,4)+M(1,3)*A3+M(1,6)*A7);
    D(3,1)=-(M(4,1)+M(4,3)*A1+M(4,6)*A5);
    D(3,2)=-(M(4,5)+M(4,3)*A4+M(4,6)*A8);
    D(3,3)=-(M(4,2)+M(4,3)*A2+M(4,6)*A6);
    D(3,4)=M(4,4)+M(4,3)*A3+M(4,6)*A7;
    D(4,1)=M(2,1)+M(2,3)*A1+(M(2,6)-eta)*A5;
    D(4,2)=M(2,5)+M(2,3)*A4+(M(2,6)-eta)*A8;
    D(4,3)=M(2,2)+M(2,3)*A2+(M(2,6)-eta)*A6;
    D(4,4)=-(M(2,4)+M(2,3)*A3+(M(2,6)-eta)*A7);
    B=c*k(v)*D;
    [psiV,qval]=eig(B);
    K=qval;
    K(1,1)=exp(-i*qval(1,1)*h(L,v));K(2,2)=exp(-i*qval(2,2)*h(L,v));
    K(3,3)=exp(-i*qval(3,3)*h(L,v));K(4,4)=exp(-i*qval(4,4)*h(L,v));
    LL=(psiV*K*inv(psiV))*LL;
end
aip=cos(theta(v))*(LL(1,1)*NII(v)-LL(2,1)*cos(thetaII(v)))+...
    NI(v)*(LL(1,2)*NII(v)-LL(2,2)*cos(thetaII(v)));
arp=-cos(theta(v))*(LL(1,1)*NII(v)-LL(2,1)*cos(thetaII(v)))+...
    NI(v)*(LL(1,2)*NII(v)-LL(2,2)*cos(thetaII(v)));
ais=NI(v)*cos(theta(v))*(LL(1,4)*NII(v)-LL(2,4)*cos(thetaII(v)))+...
    (LL(1,3)*NII(v)-LL(2,3)*cos(thetaII(v)));
ars=-NI(v)*cos(theta(v))*(LL(1,4)*NII(v)-LL(2,4)*cos(thetaII(v)))+...
    (LL(1,3)*NII(v)-LL(2,3)*cos(thetaII(v)));
bip=cos(theta(v))*(LL(3,1)*NII(v)*cos(thetaII(v))-LL(4,1))+...
    NI(v)*(LL(3,2)*NII(v)*cos(thetaII(v))-LL(4,2));
brp=-cos(theta(v))*(LL(3,1)*NII(v)*cos(thetaII(v))-LL(4,1))+...
    NI(v)*(LL(3,2)*NII(v)*cos(thetaII(v))-LL(4,2));
bis=NI(v)*cos(theta(v))*(LL(3,4)*NII(v)*cos(thetaII(v))-LL(4,4))+...
    (LL(3,3)*NII(v)*cos(thetaII(v))-LL(4,3));
brs=-NI(v)*cos(theta(v))*(LL(3,4)*NII(v)*cos(thetaII(v))-LL(4,4))+...
    (LL(3,3)*NII(v)*cos(thetaII(v))-LL(4,3));

Rpp(v)=((ars*brp-arp*brs)^(-1))*(aip*brs-ars*bip);
```

```
      Rps(v)=((ars*brp-arp*brs)^(-1))*(ais*brs-ars*bis);
      Rsp(v)=((ars*brp-arp*brs)^(-1))*(arp*bip-aip*brp);
      Rss(v)=((ars*brp-arp*brs)^(-1))*(arp*bis-brp*ais);

      Tpp(v)=((LL(2,1)*cos(theta(v))+LL(2,2)*NI(v))+Rpp(v)*(-LL(2,1)*cos(theta(v))+...
          LL(2,2)*NI(v))+Rsp(v)*(LL(2,3)-LL(2,4)*NI(v)*cos(theta(v))))/NII(v);
      Tps(v)=((LL(2,3)+LL(2,4)*NI(v)*cos(theta(v)))+Rps(v)*(-LL(2,1)*cos(theta(v))+...
          LL(2,2)*NI(v))+Rss(v)*(LL(2,3)-LL(2,4)*NI(v)*cos(theta(v))))/NII(v);
      Tsp(v)=(LL(3,1)*cos(theta(v))+LL(3,2)*NI(v))+Rpp(v)*(-LL(3,1)*cos(theta(v))+...
          LL(3,2)*NI(v))+Rsp(v)*(LL(3,3)-LL(3,4)*NI(v)*cos(theta(v)));
      Tss(v)=(LL(3,3)+LL(3,4)*NI(v)*cos(theta(v)))+Rps(v)*(-LL(3,1)*cos(theta(v))+...
      LL(3,2)*NI(v))+Rss(v)*(LL(3,3)-LL(3,4)*NI(v)*cos(theta(v)));
   LL=1;
end
J_CCW=[1;-j]/sqrt(2);
J_CW=[1;j]/sqrt(2);
J_45=[1;1]/sqrt(2);
J_0=[1;0];   %p or TM
J_90=[0;1]; %s or TE

for v=1:data_points
   A=[Tpp(v) Tps(v);Tsp(v) Tss(v)];
      tCCW=A*J_CCW;
      T_CCW(v)=tCCW'*tCCW*real(NII(v))*cos(thetaII(v))/(NI(v)*cos(theta(v)));
      tCW=A*J_CW;
      T_CW(v)=tCW'*tCW*real(NII(v))*cos(thetaII(v))/(NI(v)*cos(theta(v)));
      t45=A*J_45;
      T_45(v)=t45'*t45*NII(v)*cos(thetaII(v))/(NI(v)*cos(theta(v)));
      t0=A*J_0;
      T_0(v)=t0'*t0*real(NII(v))*cos(thetaII(v))/(NI(v)*cos(theta(v)));
      t90=A*J_90;
      T_90(v)=t90'*t90*real(NII(v))*cos(thetaII(v))/(NI(v)*cos(theta(v)));

   B=[Rpp(v) Rps(v);Rsp(v) Rss(v)];
      rCCW=B*J_CCW;
      R_CCW(v)=rCCW'*rCCW;
      rCW=B*J_CW;
      R_CW(v)=rCW'*rCW;
      r45=B*J_45;
      R_45(v)=r45'*r45;
      r0=B*J_0;
      R_0(v)=r0'*r0;
      r90=B*J_90;
   R_90(v)=r90'*r90;
   t0_a(:,v)=angle(t0)/pi;
      t90_a(:,v)=angle(t90)/pi;
      tCW_a(:,v)=angle(tCW)/pi;
      tCCW_a(:,v)=angle(tCCW)/pi;
end
ERcirc=T_CW./T_CCW;
ER=T_0./T_90;
```

```
Tlin_ret=(t0_a(1,:)-t90_a(2,:));
Tcirc_ret=-(tCW_a-tCCW_a);
Conserv_Energy_CCW=T_CCW+R_CCW;
Conserv_Energy_CW=T_CW+R_CW;
Conserv_Energy_0=T_0+R_0;
Conserv_Energy_90=T_90+R_90;
RppA=-angle(Rpp);
RssA=-angle(Rss);
TppA=-angle(Tpp);
TssA=-angle(Tss);
RppA=angle(Rpp)/pi;
RssA=angle(Rss)/pi;
TppA=angle(Tpp)/pi;
TssA=angle(Tss)/pi;
RppP=(abs(Rpp)).^2;
RssP=(abs(Rss)).^2;
TppP=(abs(Tpp)).^2.*NII(v)*cos(thetaII(v))./(NI*cos(theta(v)));
TssP=(abs(Tss)).^2.*NII(v)*cos(thetaII(v))./(NI*cos(theta(v)));
Rphasediff=(RppA-RssA);
Tphasediff=(TppA-TssA);
for(aa=1:data_points)
    if(Rphasediff(aa)<-1),Rphasediff(aa)=2+Rphasediff(aa); end;
    if(Rphasediff(aa)>1),Rphasediff(aa)=Rphasediff(aa)-2; end;
    if(Tphasediff(aa)<-1),Tphasediff(aa)=2+Tphasediff(aa); end;
    if(Tphasediff(aa)>1),Tphasediff(aa)=Tphasediff(aa)-2; end;
    if(Tlin_ret(aa)<-1),Tlin_ret(aa)=2+Tlin_ret(aa); end;
    if(Tcirc_ret(1,aa)<-1),Tcirc_ret(1,aa)=2+Tcirc_ret(1,aa); end;
    if(Tcirc_ret(2,aa)<-1),Tcirc_ret(2,aa)=2+Tcirc_ret(2,aa); end;
    if(Tlin_ret(aa)>1),Tlin_ret(aa)=-2+Tlin_ret(aa); end;
    if(Tcirc_ret(1,aa)>1),Tcirc_ret(1,aa)=-2+Tcirc_ret(1,aa); end;
    if(Tcirc_ret(2,aa)>1),Tcirc_ret(2,aa)=-2+Tcirc_ret(2,aa); end;
end

lngth=length(file_name);
lngth=lngth-2;  %remove .m
filename=file_name(1:lngth);
if(CCWfile)
    filenmRCW=[filename 'RCW '];
    filenmRCCW=[filename 'RCCW '];
    filenmTCW=[filename 'TCW '];
    filenmTCCW=[filename 'TCCW '];
    wavesnm=['WAVES/D ' x_label ' ' filenmTCW filenmTCCW filenmRCW filenmRCCW '\r'];
    y=[x_axis; T_CW; T_CCW; R_CW; R_CCW];
else
  filenmR0=[filename 'R0 '];
    filenmR90=[filename 'R90 '];
    filenmT0=[filename 'T0 '];
    filenmT90=[filename 'T90 '];
  filenmR0p=[filename 'R0p '];
    filenmR90p=[filename 'R90p '];
    filenmT0p=[filename 'T0p '];
```

```
    filenmT90p=[filename 'T90p '];
    filenmTp=[filename 'Tp '];
    filenmRp=[filename 'Rp '];
    wavesnm=['WAVES/D ' x_label ' ' filenmT0 filenmT90 filenmR0 filenmR90 filenmTp
filenmRp '\r'];
    y=[x_axis; T_0; T_90; R_0; R_90; Tphasediff; Rphasediff];
end
filenm=[pathname filename '.txt']
fid = fopen(filenm,'w');
fprintf(fid,'IGOR\n');
fprintf(fid,wavesnm);
fprintf(fid,'\nBEGIN\n');
if(CCWfile)
    fprintf(fid,'%12.8f  %12.8f  %12.8f  %12.8f  %12.8f\n',y);
else
  fprintf(fid,'%12.8f  %12.8f  %12.8f %12.8f  %12.8f  %12.8f  %12.8f\n',y);
end
fprintf(fid,'END');
status=fclose(fid);
```

REFERENCES

[1] Flanders, D. C., “Submicrometer periodicity gratings as artificial anisotropic dielectrics,” Appl. Phys. Lett **42**, 492-494,1983.

[2] Enger, R. C. and Case, S. K., “Optical elements with ultrahigh spatial-frequency surface corrugations,” Appl. Opt. **22**, 3220-3228, 1983.

[3] Bird,G. R. and Parrish, M., Jr., “The wire grid as a near-infrared polarizer,” J. Opt. Soc. Am. **50**, 886-891, 1960.

[4] Young, J. B., Graham, H. A. and Peterson, E. W., “Wire grid infrared polarizer,” Appl. Opt. **4**, 1023-1026, 1965.

[5] Tyan, R. C., Sun, P. C. and Fainman, Y., “Polarizing beam splitters constructed of form-birefringent multilayer gratings,” Proc. SPIE **2689**, 82-89, 1996.

[6] Lopez, A. G. and Craighead, H. G., “ Wave-plate polarizing beam splitter based on a form-birefringent multilayer grating,” Opt. Lett. **23**, 1627-1629, 1998.

[7] Raguin, D. H., “Subwavelength structured surfaces: theory and applications,” Ph.D. Dissertation, University of Rochester, 1993.

[8] Wendt, J. R., Vawter, G. A., Smith, R. E. and Warren, M. E., “Fabrication of subwavelength, binary, antireflection surface-relief structures in the near infrared,” J. Vac. Sci. Technol. B **14**, 4096-4099,1996.

[9] Grann, E. B., Moharam, M. G. and Pommet, D. A., “Optimal design for antireflective tapered two-dimensional subwavelength grating structures,” J. Vac. Sci. Technol. B **12**, 333-339,1995.

[10] Magnusson, R. and Wang, S. S., “New principle for optical filters,” Appl. Phys. Lett **61**, 1022-1024,1992.

[11] Norton, S. M., Erdogan, T. and Morris, G. M., “Coupled-mode theory of resonant-grating filters,” J. Opt. Soc. Am. A **14**, 629-639, 1997.

[12] Stork,W., Streibl, N., Haidner, H. and Kipfer, P., “Artificial distributed-index media fabricated by zero-order gratings,” Opt. Lett. **16**, 1921-1923, 1991.

[13] Wendt, J. R., Vawter, G. A., Smith, R. E. and Warren, M. E., “Subwavelength, binary lenses at infrared wavelengths,” J. Vac. Sci. Technol. B **15**, 2946-2949,1997.

[14] Babin, S. and Danilov, V., “Variable shaped electron-beam lithography application to subwavelength and computer generated diffractive optics fabrication,” J. Vac. Sci. Technol. B **13**, 2767-2771,1995.

[15] Zhou, Z. and Drabik, T. J., “Optimized binary, phase-only, diffractive optical element with subwavelength features for 1.55μm,” J. Opt. Soc. Am. A **12**, 1104-1112, 1995.

[16] Astilean, S., Lalanne, P. and Chavel, P., “High-efficiency subwavelength diffractive element patterned in a high-refractive-index material for 633nm,” Opt. Lett. **23**, 552-554, 1998.

[17] Wendt, J. R., Vawter, G. A., Smith, R. E. and Warren, M. E., “Nanofabrication of subwavelength, binary, high-efficiency diffractive optical elements in GaAs,” J. Vac. Sci. Technol. B **13**, 2705-2708,1995.

[18] Jiang, J. J., “Rigorous analysis and design of diffractive optical elements,” Ph.D. thesis proposal, University of Alabama, Huntsville, Fall 1998.

[19] Nordin, G. P., Deguzman, P. C., Meier, J. T., Jiang, J. J. and Jones, M. W., “Array of stacked subwavelength gratings for polarization analysis,” EOS Topical Meeting on Diffractive Optics (European Optical Society Topical Meetings Digest Series: Volume 22, 1999), p. 221.

[20] Born, M., and Wolf, E., *Principles of Optics*, 7th Ed., Cambridge University Press, 837-840, 1999.

[21] Cescato, L. H., Gluch, E. and Streibl, N., “Holographic quarterwave plates,” Appl. Opt. **29**, 3286-3290, 1990.

[22] Xu, F., Tyan, R. C., Sun, P. C., and Fainman, Y., “Fabrication, modeling, and characterization of form-birefringent nanostructures,” Opt. Lett. **24**, 2457-2459, 1995.

[23] Kim,T. J., Campbell, G. and Kostuk, R. K., “Volume holographic phase-retardation elements,” Opt. Lett. **20**, 2030-2032, 1995.

[24] Kikuta, H., Ohira, Y. and Iwata, K., “Achromatic quarter-wave plates using the dispersion of form birefringence,” Appl. Opt. **36**, 1566-1572, 1997.

[25] Chou, S. Y., Schablitsky, S. J. and Zhuang, L., “Application of amorphous silicon gratings in polarization switching vertical-cavity surface-emitting lasers,” J. Vac. Sci. Technol. B **15**, 2864-2867, 1997.

[26] Yeh,P., “A new optical model for wire grid polarizers,” Opt. Comm. **26**, 289, 1978.

[27] Kuta, J. J., Van Driel, H. M., Landheer, D. and Feng, Y., “Coupled-wave analysis of lamellar metal transmission gratings for the visible and the infrared,” J. Opt. Soc. Am. A **12**, 1118-1127, 1995.

[28] Stenkamp, B., Abraham, M., Ehrfeld, W., Knapek, E., Hintermaier, M., Gale, M. T. and Morf, R., “Grid polarizer for the visible spectral region,” SPIE **2213**, 288-296, 1994.

[29] Bernhard, C. G., “Structural and functional adaptation in a visual system, “ Endeavor **26**, 79-84.

[30] Hecht, E., *Optics*, 2nd Ed., Addison-Wesley Publishing Company, 375, 1987.

[31] Wood, R. W., “On a remarkable case of uneven distribution of light in a diffraction grating spectrum,” Philosophical Magazine **4**, 396-402 (1902).

[32] Rytov, S. M., “Electromagnetic properties of a finely stratified medium,” Sov. Phys. JETP **2**, 466-475, 1956.

[33] Musson, B. D., Sze, F. C., Reinhard, D. K. and Asmussen, J., “Anisotropic etching of submicron silicon features in a 23 cm diameter microwave multicusp electron-cyclotron-resonance plasma reactor,” J. Vac. Sci. Technol. B **9**, 3521-3525, 1991.

[34] Bhardwaj, J. K., Ashraf, H. and STS Ltd., “Advanced silicon etching using high density plasmas,” SPIE **2639**, 224-233, 1995.

[35] Hirobe, K., Kawamura, K. and Nojiri,K., “Formation of deep holes in silicon by reactive ion etching,,” J. Vac. Sci. Technol. B **5**, 594-600, 1987.

[36] Mansano, R. D., Verdonck, P. and Maciel, H. S., “Deep trench etching in silicon with fluorine containing plasmas,” Applied Surface Science **100**, 583-586, 1996.

[37] Jansen, H., De Boer, M., Legtenberg, R. and Elwenspoek, M., “The black silicon method: a universal method for determining the parameter setting of a fluorine-based reactive ion etcher in deep silicon trench etching with profile control,” J. Micromech. Microeng. **5**, 115-120, 1995.

[38] Grigoropoulos, S., Gogolides, E., Tserepi, A. D. and Nassiopoulos, A. G., “Highly anisotropic silicon reactive ion etching for nanofabrication using mixtures of SF6/CHF3 gases,” J. Vac. Sci. Technol. B **15**, 640-645, 1997.

[39] Vogel, S., Schaber, U., Kuhl, K., Schafflik, R., Pradel, H., Kozlowski, F. and Hillerich, B., “Novel microstructuring technologies in silicon,” Mikrosystemtechnik-Symposium zur Productronica 97, 1997.

[40] Watanabe, S., “ECR plasma etchers,” in *Plasma Etching, Fundamentals and Applications*, Ch. 7, Sugawara, M. (ed.), Oxford University Press, 310, 1998.

[41] Collett, E., “The Stokes polarization parameters”, in *Polarized Light: Fundamentals and Applications*, Ch. 4, Marcel Dekker, Inc., 33-66, 1993.

[42] Denes, L. J., Gottlieb, M., Kaminsky, B. and Huber, D. F., “Spectro-polarimetric imaging for object recognition,” SPIE **3240**, 8-18, 1998.

[43] Peters, K. W., Turner, T. S. and Tyo, J S., “Portable visible imaging spectropolarimetr for remote sensing applications,” SPIE **3498**, EUROPTO Conference on Sensors, systems, and next-generation satellites II, Barcelona Spain, 1998, 223-230.

[44] Shaw, J. A. and Descour, M. R., “Instrument effects in polarized images,” Opt. Eng., **34** (5), 1396-1399, 1995.

[45] Bishop, K. P., McIntire, H. D., Fetrow, M. P. and McMackin, L., “Multi-spectral polarimeter imaging in the visible to near IR,” SPIE **3699**, SPIE Conference on Targets and Backgrounds: Characterization and Representation V, 49-57, 1999.

[46] Smith, M. H., Howe, J. D., Woodruff, J. B., Miller, M. A., Ax, G. R., Petty, T. E. and Sornsin, E. A., “Multispectral infrared Stokes imaging polarimeter,” SPIE **3754**, Conference on Polarization: Measurement, Analysis and Remote Sensing II, 137-143, 1999.

[47] Gandorfer, A. M., “Ferroelectric retarders as an alternative to piezoelastic modulators for use in solr Stokes vector polarimetry,” Opt. Eng. **38**(8), 1402-1408, 1999.

[48] November, L. J. and Wilkins, L. M., “Liquid crystal polarimeter: a solid state imager for solar vector magnetic fields,” Opt. Eng. **34**(6), 1659-1668, 1995.

[49] El-Saba, A. M. and Abushagur, M. A. G., “Diffractive-optical element based photopolarimeter,” SPIE Vol. 3754, Conference on Polarization: Measurement, Analysis and Remote Sensing II, 260-265, 1999.

[50] Nordin, G. P., Meier, J. T., Deguzman, P. C. and Jones, M. W., "Diffracative optical element for Stokes vector measurement with a focal plane array," SPIE **3754**, Conference on Polarization: Measurement, Analysis and Remote Sensing II, 169-177, 1999.

[51] Gehrels, T. (ed.), *Planets, Stars, and Nebulae Studied with Polarimetry*, University Arizona Press, Tucson, 1974.

[52] Jacques, S. L. and Lee, K., "Imaging tissues with a polarized light video camera," SPIE **3863**, 68-74, 1999.

[53] Chipman, R. A., "Polarimetry", in *Handbook of Optics Vol. II: Devices, Measurements and Properties*, 2nd Ed., Ch. 22, 22.0-22.37, 1994.

[54] Barbour, B. A., Barnes, H. B., Lewis, C. P., Lindquist, P. E.A., Jones, M. W. and Mohon, N., "Imaging polarimetry: applications for generating images where contrast is small," Optics and Photonics News, August 1998.

[55] Nordin, G. P., Meier, J. T., Deguzman, P. C. and Jones, M. W., "Micropolarizer array for infrared imaging polarimetry," J. Opt. Soc. Am. A **16**, 1168-1174, 1999.

[56] Moharam, M. G. and Gaylord, T. K., "Rigorous coupled-wave analysis of planar-grating diffraction," J. Opt. Soc. Am. **71**, 811-818, 1981.

[57] McPhedran, R.-C., Botten, L. C., Craig, M. S., Neviere, M. and Maystre, D., "Lossy lamellar gratings in the quasistatic limit," Opt. Acta **3**(29), 289-312, 1982.

[58] Collett, E., "The Jones matrix calculus", in *Polarized Light: Fundamentals and Applications*, Ch. 10, Marcel Dekker, Inc., 187-218, 1993.

[59] Born, M. and Wolf, E., *Principles of Optics*, 7th Ed., Cambridge University Press, 54-74, 1999.

[60] Yeh, P., *Optical Waves in Layered Media*, John Wiley & Sons, 239-248, 1988.

[61] Berreman, D. W., "Optics in stratified and anisotropic media: 4x4-matrix formulation," Journal of the Optical Society of America **62**(4), 502-510, 1972.

[62] Moharam, M. G. and Gaylord, T. K., "Rigorous coupled-wave analysis of metallic surface-relief gratings," J. Opt. Soc. Am. A **3**, 1780-1787, 1986.

[63] Chambers, D. M., "Stratified volume diffractive optical elements as high-efficiency gratings," J. Opt. Soc. Am. A **16**, 1184-1193, 1999.

[64] Born, M. and Wolf, E., *Principles of Optics*, 7th Ed., Cambridge University Press, 27-28, 1999.

[65] Nordin, G. P. and Deguzman, P. C., "Broadband form birefringent quarter waveplate for the mid-infrared wavelength region", Optics Express **5**(8), 163-168, 1999.

[66] Wolfe, W. L. and Zissis, G. J., *The Infrared Handbook*, IRIA Center, Environmental Research Institute of Michigan, 7-76, 1985.

[67] Goldstein, D. H., Chipman, R. A. and Chenault, D. B., "Infrared spectropolarimetry," Opt. Eng. **28**(2), 120-125, 1989.

[68] Chipman, R. A. and Cheneault, D. B., U.S. Patent #4,961,634, “Infrared achromatic retarder,” October, 1990.

[69] Molectron Detector Inc., Catalog 1999.

[70] Stenkamp, B., Abraham, M., Ehrfeld, W., Knapek, E., Hintermaier, M., Gale, M. T. and Morf, R., “Grid polarizer fo the visible spectral region,” in *Nanofabrication Technologies and Device Integration*, Karthe, W., ed., Proc SPIE **2213**, 288-296 (Society of Photo-Optical Instrumentation Engineers, Bellingham, Wash., 1994).

[71] Van Zant, P., *Microchip Fabrication: A Practical Guide to Semiconductor Processing*, 3rd Edition, McGraw Hill, 306, 1997.

[72] Meier, J. T., Master’s Thesis topic, University of Alabama in Huntsville, 2000.

[73] Deleuil, R., “Construction and use of an apparatus intended for the study of irregular dioptres and gratings by millimeter waves,” Opt. Acta **16**, 23-25, 1969.

[74] Jensen, M. A. and Nordin, G. P., “Finite-aperture wire grid polarizers,” accepted for publication in JOSA A.